POLITECNICO DI MILANO

School of Industrial and Information Engineering

Master of Science in Engineering Physics

POLITECNICO
MILANO 1863

Master's Degree Thesis

Two-Layer Reconstruction of Raman Spectra in Diffusive Media by Time-Domain Approaches

Author:
STEFAN ŠUŠNJAR
Student ID: 918771

Supervisor:
Prof. ANTONIO PIFFERI

Co-Supervisors:
Prof. DAVIDE JANNER
Dr ANDREA FARINA

Academic Year 2019-2020

Summary

Diffuse Optics techniques enable depth sensitivity of up to few centimetres, non-invasively through the diffusive media. Raman Spectroscopy provides excellent chemical specificity. The joint of these two fields can be applied for retrieving chemically specific information about the molecules at different depths inside the diffusive medium.

The goal of this thesis work was to test the novel concept of Diffuse Raman spectra reconstruction from a two-layer diffusive medium by rigorous time-domain approaches. The main objectives were:

1) to develop a method able to:

   a) calculate the Raman reflectance in a defined geometrical and optical configuration of the two-layers;

   b) solve the inverse problem, retrieving the unknown spectra, when the Raman reflectance measurements are known;

2) to simulate measurements, by including the noise and the instrument response function of the acquisition system, and then reconstruct the spectra and estimate the quality of the reconstruction;

3) to validate the reconstruction method on experimental data.

Accordingly, the core of the thesis work consists of the following parts:

- presentation of the mathematical model of diffuse Raman processes in time-domain and its implementation in the developed software (Chapter 2);

- systematic study on the impact of various geometrical and optical parameters on the reconstruction of the two-layer spectra (Chapter 3);

- reconstruction of Raman spectra from experimental data stem from a novel time-domain setup (Chapter 4).

The program developed in Python computes the forward model, then solves the inverse problem, with a total processing time of around one minute on an average PC. The method exploits a heuristic approach to derive Diffuse Raman propagation from the solution of the Diffusion Equation for a two-layer geometry. As found by the simulations, the main factors that limit the two-layer reconstruction are the thickness of the top layer and the number of collected photons. The reconstruction on experimental data proved the applicability of the new concept, rigorously separating the two-layer spectra for the first time.

Sommario

Le tecniche di Ottica Diffusa consentono di investigare mezzi fortemente diffondenti (es. tessuti biologici) in modo non invasivo fino ad alcuni centimetri di profondità. La Spettroscopia Raman consente di ottenere un'eccellente specificità chimica del campione analizzato. L'unione di questi due campi può essere sfruttata per recuperare specifiche informazioni chimiche sulle molecole a diverse profondità all'interno del mezzo diffusivo.

L'obiettivo di questo lavoro di tesi è di testare un nuovo metodo di ricostruzione degli spettri Raman dal mezzo diffusivo in un sistema a due strati mediante approcci rigorosi nel dominio del tempo. Gli obiettivi principali del lavoro sono:

1) sviluppare una metodica in grado di:

   a) calcolare la riflettanza Raman diffusa in una geometrica a due strati;

   b) risolvere il problema inverso, recuperando lo spettro Raman dei due strati, a partire da misure di riflettanza Raman diffusa;

2) simulare misure sperimentali, includendo il rumore e la funzione di risposta strumentale del sistema di acquisizione, per poi ricostruire gli spettri e stimare la qualità della ricostruzione;

3) validare il metodo di ricostruzione tramite dati sperimentali.

Pertanto, il nucleo della tesi è costituito dalle seguenti parti:

- presentazione del modello matematico del Raman in mezzi diffondenti nel dominio del tempo e delle sue applicazioni nello sviluppo del software (Capitolo 2);

- studio sistematico dell'impatto di vari parametri ottici e geometrici sulla ricostruzione degli spettri a due strati (Capitolo 3);

- ricostruzione di dati sperimentali ottenuti con un sistema innovativo tempo-risolto (Capitolo 4).

Il programma sviluppato in Python calcola il modello forward e risolve il problema inverso, con un tempo di processamento totale di circa un minuto su un PC medio. Il metodo sfrutta un approccio euristico per descrivere la propagazione Raman in mezzi diffusivi a partire dalla soluzione dell'Equazione della Diffusione per una geometria a due strati. Come riscontrato dalle simulazioni, i principali fattori che limitano la ricostruzione a due strati sono lo spessore dello strato superiore e il numero di fotoni raccolti. La ricostruzione sui dati sperimentali ha dimostrato l'applicabilità del nuovo metodo, ottenendo per la prima volta la separazione rigorosa degli spettri dei due strati.

Acknowledgements

Firstly, I would like to express my sincere gratitude to my professor and supervisor of this thesis work, Antonio Pifferi. He showed a great professionalism in these challenging times, guiding me through the thesis work and making it possible for me to complete it in time and manner I wanted. I am very happy I had this opportunity to work with Prof. Pifferi, who has a great knowledge and experience in the field I have just entered, but more importantly, his pedagogical approach made a particularly strong impression on me. Many things I have learned from him could be beneficial and significant for my future work and life.

I am also thankful to my co-supervisors, Dr Andrea Farina and Prof. Davide Janner. Dr Farina was engaged from the very beginning of this thesis work, following my advancement, and providing me with useful information and suggestions. Prof. Janner was enthusiastic to read my thesis and provide support from the side of Politecnico di Torino.

Moreover, I owe great thanks to Dr Fabrizio Martelli from Università degli Studi di Firenze. Without his contribution in the field of theoretical modelling, the novel concept demonstrated in this thesis could not be born. His earlier numerical implementation of the solution to a more fundamental problem presented an excellent starting point for me to develop the methods which finally produced the desired outcome.

While appreciating the impact of teachers, professors and scholars on my development as a mathematician, physicist and engineer, I should remember all the people from whom I was learning in the following schools: Politecnico di Milano, Faculty of Electrical Engineering and Mathematical Grammar School in Belgrade and Regional Centre for Talents "Mihajlo Pupin" in Pančevo. These are the four Institutions with the capital "I", whose part I have been combined for more than 15 years.

Finally, studying abroad is a challenging period in a lifetime. They all, of course, know, but I can also state here that the support from my family has never been absent from my life and I feel it has even strengthened since the moment I started this academic journey in Milano. Many positive words I can find also for my friends,

from Serbia or other countries, which I knew before or met here in Italy, but then, my already long sentences would become even longer. I will just conclude with an observation that the time spent with good people always positively reflects on our lives. I am grateful to all the people who can recognize themselves among these lines.

In Milano, November 2020.

Stefan Šušnjar

Table of Contents

"Knowledge is the light which illuminates our path through this life and leads to a future life of everlasting glory"

- Mihajlo Pupin

Chapter 1

Introduction on Diffuse Raman Spectroscopy

The available knowledge and realized or potential applications of light have been growing from day to day in this century. The research in the field of photonics, combined with other sciences, opened very attractive new fields, among which the biophotonics is. The idea of using just light to examine the biological tissues in vivo, completely noninvasively and make precise clinical diagnosis, may sound astonishing, but actually is not that far from reality. This is the field where Diffuse Optics has had results recently, relying on the nature of photon propagation through certain media, which we will later define and call diffusive, such as biological tissues. These media allow photons to collect information from depth, even though the photons are starting and finishing their paths on the surface of the medium, outside of the tissue. While propagating through the diffusive medium, if the photons are not elastically, but rather inelastically, in a specific way scattered on the molecules of the medium, then we are introducing the phenomenon of Raman scattering. Every time a photon is Raman scattered, not only its movement direction is changed, but also its energy, and by the specific amount, inherent to the molecule the photon scattered on. This means that the information obtained by just considering the Raman shifted wavelengths of detected photons can increase the potentials of Diffuse Optics and make it extremely chemically specific.

In this chapter, we will introduce the basics of the physics of Diffuse Optics and Raman scattering. We will also see what can be achieved when the two fields, Diffuse Optics and Raman Spectroscopy, are combined, and what are the technical realizations and applications. To arouse the curiosity of the reader, here we will just say that the Diffuse Raman is applied in many fields, from clinical diagnostics, then analysis of substances such as pharmaceuticals and food, or potential explosives in security controls, even in conservation sciences for the analysis of cultural heritage.

The key advantages are noninvasiveness, depth sensitivity and chemical specificity. If we are able to develop the theory and methods to better utilize the measured Raman signal obtained from the diffusive media, then the horizon of the potential applications will expand. To make a connection with the full title of the thesis, the topic of this thesis work, as it will be seen in the end of this chapter, is exactly the theoretical modelling in time domain and development of the reconstruction methods, which goal is to retrieve the Raman spectra from the probed two-layer media. Two-layer media are simply chosen to prove the concept and show the potential of retrieving the separated Raman spectra of the two layers, when the information of interest is hidden beneath the surface layer.

1.1 Diffuse Optics

1.1.1 Absorption and Scattering

Light propagation through scattering media is, as expected by its name, not straightforward. In corpuscular representation of light, direction of propagation of each photon is affected by many scattering events. If the photons can also be absorbed by the medium, and by that removed from further propagation, giving the energy to the medium at the same time, then that medium has also absorption properties. The media with scattering and absorption properties are called turbid media. Propagation of light through such media is well described by Radiative Transfer Equation (RTE), which emerges from more general Transport Theory. If some further assumptions on the medium can be made, light propagation could be described with Diffusion Equation (DE), and the medium is then called diffusive. Through diffusive media, photon paths look like a random walk (array of short piecewise straight-line segments). This is the consequence of a large number of scattering events, at which photons randomly change direction of movement. Abovementioned equations and corresponding mathematical models describing light propagation in turbid media will be explained in Chapter 2. Examples of diffusive media are biological tissues, agricultural products, wood, paper, plastic materials, sugar, salt, milk [1]. To give just a brief insight into the geometry of the setup, exploiting the scattering phenomenon, source and detector can be positioned on the surface of the medium, on the same side - which is known as the reflectance configuration, or even on opposite sides - in which case it is the transmittance configuration. What can be obtained from light probing the diffusive medium is, in principle, information about the absorption and scattering coefficients of the medium.

The coefficient of absorption, denoted as $\mu_a\,[\mathrm{mm}^{-1}]$, in very simple case of light beam passing through a homogeneous medium, shows how the intensity I of light decreases with the distance z travelled through the medium, according to the

Beer-Lambert law: $I(z) = I(0)e^{-\mu_a z}$. Another definition, more statistical, would be: the probability that a medium absorbs a photon after travelling the distance $\mathrm{d}l$ through it, is equal to $\mu_a \mathrm{d}l$.

The coefficient of scattering, however, often expressed as reduced scattering coefficient $\mu_s' \, [\mathrm{mm}^{-1}]$ represents the inverse of the mean free path travelled by photon between the two scattering events. In other words, probability of photon scattering after passing the distance $\mathrm{d}l$ through medium is equal to $\mu_s \mathrm{d}l$.

In a particular example of biological tissue as a diffusive medium, absorption is determined by the tissue components, while scattering is related to its structure. These properties depend on the wavelength of light as well. When recording the spectrum of absorption or scattering in visible or near-infrared region, it is possible to estimate the density of scatterers, their equivalent size, or on the other hand, changes in absorption. These changes are associated with some changes in the tissue – either as a consequence of the activity (for example increased blood flow due to the increase in need for oxygenation of brain parts when performing certain activity) or as a consequence of some pathological changes (cysts, lesions and tumours).

Note that it was never imposed that coefficients of absorption and scattering are constant parameters for the medium. They are properties of the medium and may vary, if the medium is inhomogeneous, depending on the position, i.e, in general, they are functions of the position vector $\vec{r}$: $\mu_a(\vec{r})$ and $\mu_s'(\vec{r})$. This is of practical importance when applying Diffuse Optics to retrieve the information on biological tissue, for example, and some local changes within it.

1.1.2 Physics of Diffuse Optics

In order to better understand how the information is extracted, we have to understand the physics of the problem. Let us assume we have a biological tissue, that is a semi-infinite medium (which is not particularly important now, but we represent it like this for simplicity), and the source and detector on top of it, at some distance ρ. Thanks to scattering phenomena, there are many paths for photons to reach the detector, starting from the source (see Figure 1.1). The signal at the detector will depend on many factors.

Obviously, the higher the absorption, the lower the number of photons will arrive to the detector. For higher scattering coefficients, photons will have more "complicated" paths, or, in our "random-walk" representation, longer and more frequently randomized. Therefore, it is expected to detect majority of them later in time. If the distance between the source and the detector increases, we expect to have more information from depth, however, the deeper the photons go into the medium, the more of them will be absorbed, and therefore, the useful signal will be weakened. If we measure a temporal profile of the number of photons detected, then

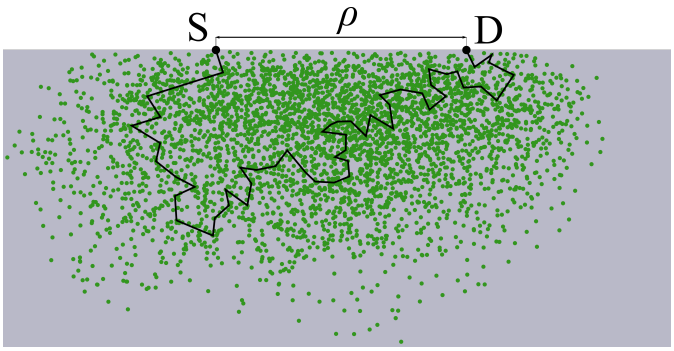

Figure 1.1: Photon scattering in the diffusive medium. Black circles represent positions of the source (S) and the detector (D) in the reflectance measurement configuration. Green dots represent the molecules on which the photons scattered while propagating from the source to the detector. A sequence of straight line segments in black represents one exemplary "random walk" photon path.

we know that the information from close to the surface arrives first, and photons from depth arrive later, since they have longer paths. This is very attractive idea, because even for small source-detector distances, one can retrieve the information from depth [2, 3]. When having appropriate technical equipment, fast time gating can increase amount of information, allowing to choose which time intervals (time gates) are of interest, or in other words, which ones carry the desired information.

The depth sensitivity and noninvasiveness of the Diffuse Optics make it very promising for application in many fields. Even that can be improved, in terms of quality of information. Diffusion of photons during their propagation through diffusive medium can be combined with other physical effects, such as Raman scattering, leading to a wide range of interesting applications, as it will be described in Section 1.5.

1.2 Raman Spectroscopy

1.2.1 Physics of Raman Emission

For light scattering described so far, we considered only change in directions of propagation of photons. That was important for the photon paths and their arrival times. One can ask a question what happens with the wavelengths of scattered photons. Detected photons are usually resolved by wavelengths, and in Diffuse Optics applications, they are expected at the wavelengths of the excitation light. And that is what is obtained experimentally, therefore, for the scattering considered so far, we can say it is elastic, since the energy of single photons (which successfully

come to the detector) is conserved after scattering events. Depending on the relative size of the scattering molecules in comparison to the wavelength of incident photons, theories of Reyleigh scattering (scatterer dimensions smaller than wavelength of light) or Mie scattering (general) are to be applied.

However, in 1928, Raman discovered a new type of secondary radiation, much weaker signal shifted to different wavelengths [4]. This was explained as a new type of scattering, now called Raman scattering, which is, by its nature, inelastic. Energy of arriving photon is altered upon scattering of a molecule, so-called Raman emitter, since it re-emits the radiation, but with different wavelength, either higher or lower. The rest of the energy (either excess or lack) corresponds to the difference in energies between rotational or vibrational states of the scattering molecule. The incoming photon excites the molecule, theoretically promoting it to a higher energy virtual state. Depending on the chemical bonds forming the molecule, it is possible that the molecule almost immediately re-emits a photon, and reaches different vibrational level. Difference in energies between the initial and final vibrational level is a characteristic of the bond and therefore inherent for the molecule. If the final state is of higher energy in comparison with the initial state, then the scattered (re-emitted) photon will have lower energy (longer wavelength) and the shift is called Stokes shift. On the other hand, if the final state is of lower energy, then the scattered photon will have higher energy (shorter wavelength) and the shift is called anti-Stokes shift.

If the wavelength of an incident photon is λ_0 and the wavelength of a scattered photon is λ_1, Raman shift is defined in the following way: $\Delta\overline{\nu} = \frac{1}{\lambda_0} - \frac{1}{\lambda_1}$, which simply follows from the energy conservation law. Usual unit for Raman shift in Raman Spectroscopy is [1/cm], and it will be used throughout this work, as well as [nm] for wavelengths of incident and Raman-emitted light. A graphical representation with energy levels is given in Figure 1.2.

1.2.2 Information Content

As it was seen from the previous section, Raman emission is determined by the scattering molecule and its vibrational states. In other words, it is chemically specific, determined by the substance (molecule) that scatters photons. If we are able to measure the spectrum of detected photons, i.e. number of photons at different wavelengths, at the positions where peaks are found, we should expect to read information. If considering only Raman effect, each peak should be ascribed to a certain vibrational mode that is inherent for the molecules from which the medium is composed. Why? Because the energy of scattered photon may be either unaltered (elastic, Mie scattering) or changed by well determined amount - the difference between vibrational levels (inelastic, Raman scattering).

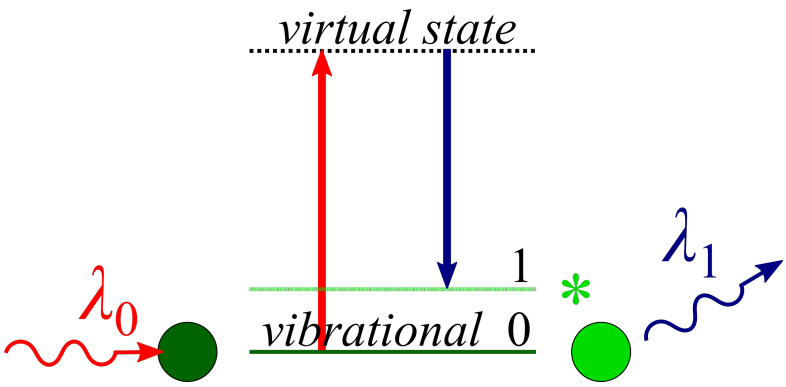

Figure 1.2: Raman scattering event. From left to right: a photon with wavelength λ_0 excites a molecule in vibrational state 0, thus promoting it to a virtual energy state; then the molecule takes the vibrational state 1, by releasing a photon in random direction, with altered wavelength λ_1.

In practice, signal at the detector, obtained at wavelengths different from the source emission wavelength is very weak, since Raman emission is a secondary radiation, whose intensity depends on the chemical bonds themselves and their properties, and density and effective dimensions of Raman scatterers. It is necessary to filter out the signal at the source emission wavelength and look only for the signals at shifted wavelengths, usually expressed as Raman shifts, rather than absolute values of wavelengths of Raman re-emitted light. This is not essential, but we want to draw attention at this place, since all the results of the Raman spectra in Chapters 3 and 4 will be presented in terms of Raman shifts. When the peaks with their positions and intensities are recognized, one can determine the exact molecules that are found in the medium, opening very wide field of applications.

We should also note that there are other inelastic scattering processes that take place, and therefore affect the spectrum of detected photons. One of them is the fluorescence, which, unlike the Raman emission, does not occur immediately when photon excites the molecule, but with a given delay distribution, with a certain probability, and on a range of wavelengths. This is the property that can make the reconstruction of Raman spectra difficult, as it will be pointed out in Chapter 4.

1.3 Diffuse Raman

1.3.1 Joint of the Two Fields

As it was anticipated in the introduction on Diffuse Optics and Raman Spectroscopy, combination of these two fields predicts even more interesting possibilities. Firstly, Diffuse Optics techniques allow noninvasive probing of biological tissues with a

sensitivity up to a few centimetres in depth. Quantitative information can be obtained by retrieving the absorption and scattering coefficients of certain regions inside the medium. Secondly, Raman signal carries the information about the fingerprint of molecules contained in the medium. In other words, molecules can be distinguished by their Raman spectra, which provides an excellent tool for performing the chemical specification of the medium. Taking advantage of the properties of photon propagation through diffusive media, treated by the Diffuse Optics, using the techniques developed there, with a modification that takes into account the chemically specific information of Raman signal, a very powerful tool can be obtained. This is theory. In practice, there is always a question of implementation. How to exploit the aforementioned properties in the best way, to be able to reconstruct the complete spectrum at certain depth or even different spectra of many different layers that could exist in the medium? Measurements with variable parameters are needed. The principle is that each set of parameters provides different sensitivities for different layers, thus making it possible to focus on Raman signal from a specific depth. The depth sensitivity is determined by: different distance between the source and the detector in Spatially Offset Raman Spectroscopy (SORS), different optical properties for different wavelengths in Frequency Offset Raman Spectroscopy (FORS), different time gates in Time Resolved Raman Spectroscopy, all of them in reflectance configuration. There is also a transmittance configuration technique, called Transmittance Raman Spectroscopy (TRS), which does not provide depth sensitivity, rather chemical investigation of the entire probed volume. We will briefly discuss SORS, FORS and TRS techniques and then move to the Time Domain and focus on the core of this thesis work.

1.3.2 Spatially Offset Raman Spectroscopy (SORS)

The SORS technique relies on spatially separating the light collection zone (detector) from the illumination zone (light source). This way, the overwhelming much stronger surface Raman and fluorescence signals can be suppressed, because of the fact that the photons migrating near the surface on their way from the source to the detector have higher probability of being lost at the sample-to-air interface, in comparison to the photons that go deeper into the sample. The mean photon penetration depth increases with increasing distance between the source and the detector on the surface of the sample [5].

The technique was first introduced by Matoušek et al. in 2005 [6]. We can imagine probing the heterogeneous, multi-layer medium. With varying the separation between the laser illumination zone and the collection zone, different weights are given to surface and subsurface layers contributing to the total Raman signal. For greater separations, information from deeper subsurface layers will contribute more (see Figure 1.3, left). With a few different separations, the same number of so-called

"spatial gates" are created, each of them accounting the contribution of every layer with different weight. With at least the same number of "gates" (measurements) as unknowns (spectra of different layers), it is possible in principle to retrieve the spectra of individual layers. Such obtained Raman spectra can be corrected by subtracting the undesired layers spectra scaled with coefficients chosen to remove the particular components. There are also other implementations of SORS in the specific environments, such as: Micro-SORS [7] and SERS (Surface-Enhanced Raman Spectroscopy) [8, 9].

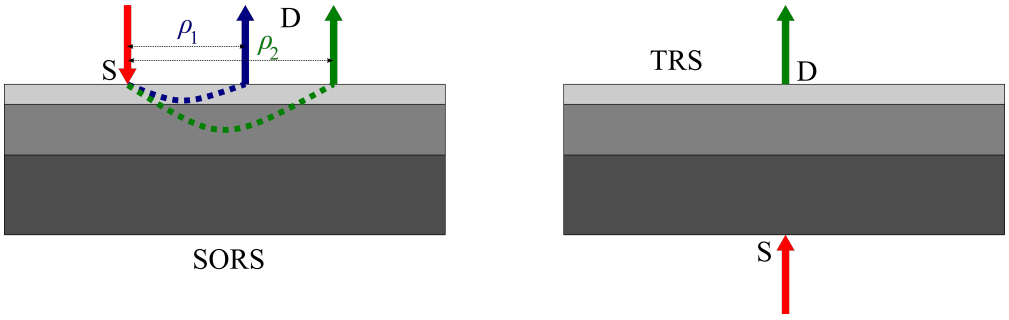

Figure 1.3: SORS configuration (left) and TRS configuration (right). In SORS, different source-detector (SD) separations (ρ_1 and ρ_2) are used to obtain different sensitivity: blue and green photon paths from the source (red arrow) to the detector (blue or green). In TRS (right), the source and the detector are on the opposite sides of the probed medium.

1.3.3 Transmittance Raman Spectroscopy (TRS)

The first demonstration of this technique dates back in 1967 [10]. However we will present it from the point of view of modern techniques. The easiest way to approach the Transmittance Raman Spectroscopy is to compare it with SORS. TRS can be considered as SORS with distance between the source and the detector in such extreme that they are on opposite sides of the medium. [5]. The signal is no longer measured in reflectance, but in transmittance configuration (see Figure 1.3, right). This is beneficial for the acquisition of the chemically specific information of the entire probed volume. By searching through the entire volume, it is possible to discriminate if there is a certain object on unknown location inside the medium. However, depth resolving features of SORS cannot be exploited in this configuration. Combination of this technique with SORS could be very interesting for the identification of the buried object in the diffusive medium, by its chemical composition and spatial position [11].

1.3.4 Frequency Offset Raman Spectroscopy (FORS)

As it was shown by Martelli et al. in 2016 [12], the mean penetration depth of photons is dependent on the optical properties of the medium. For a continuous-wave (CW) illumination and detection, when the absorption coefficient increases, the mean penetration depth of photons decreases. Hence, in case of low absorption, one should expect information from deep layers to be present, while in case of high absorption it would be suppressed. For what concerns the scattering coefficient, higher values prevent photons from going deep into the medium, thus reducing the amount of information from the bottom. Therefore, having lower values for scattering would increase the contribution of deep layers.

This seems analogous to SORS, but the main question is how to affect the optical properties of the medium and select the combination of low absorption - low scattering for deep insight, or higher absorption - higher scattering for insight much closer to the surface of the sample. The answer is given by Konugolu et al. in their paper from 2017, where a new technique, named Frequency Offset Raman Spectroscopy (FORS) was proposed [13]. The FORS technique relies on the optical properties dependence on wavelengths. By properly choosing the excitation laser wavelength, it is possible to make such a contrast in optical properties that will significantly affect the contribution of layers at different depths. Again, by making some "frequency gates", i.e. measurements at different frequencies (wavelengths) of excitation light, one can see different contributions from individual layers, depending on how deep in the medium the layer is.

In comparison to SORS, FORS has higher signal-to-noise ratio, since the distance between the source and the detector can be kept very small. FORS has also better spatial resolution, again because of the fact that this source-detector separation is constant and small. However, the possibility of enhancing the signal from depth is highly dependent on the optical contrast achievable by frequency variation. Moreover, the multiple-frequency (multiple-wavelength) excitation system is another practical challenge for the complexity of the whole system.

According to Konugolu et al. [13], combination of SORS and FORS, a sort of hybrid FORS-SORS technique, gives even better results, in terms of bottom layer signal enhancement.

1.4 Time Domain Techniques

Time Resolved Raman Spectroscopy relies on the so-called "time encodes depth" principle, which should have been taken as the important message from the introductory sections on physics of the Diffuse Optics. Additionally, despite the great chemical specificity of the Raman signal, intensities are usually very low and therefore very specific requirements are to be met by the acquisition systems

in terms of detection efficiency, noise suppression and background removal. It is necessary to use very short laser pulses as an excitation and look for temporal response at the detector. The system should have a short response time in order to effectively apply the time gating. Time gates (intervals at which the photons are counted) increase the signal-to-noise ratio, moreover, their proper positioning in time allows the extraction of information of interest. To obtain information from deeper layers of the sample, one should not collect (or count) photons at initial times (or a first few gates), since that signal is overwhelming the later arriving, much weaker signal from depth. Moreover, some gates are to be chosen or avoided in such way to reduce the impact of fluorescence and other background radiation.

In the following subsections, possible realizations of the time gating techniques will be presented.

1.4.1 Kerr Gating

Prior the paper on SORS technique, in the same year (2005) Matoušek et al. demonstrated another technique to effectively separate Raman signals originating from different depths in heterogeneous diffusive media [14]. The method relies on a picosecond laser pulse excitation and fast temporal gating of detected Raman scattered photons. By the same group, very similar experimental setup was earlier used to reject the fluorescence from the Raman spectra [15].

The physical effect adopted to produce the temporal gating of photons with this technique was the Kerr effect. Namely, the Raman scattered light is passed through the so-called Kerr gate, which consists of the two crossed polarizers, and a Kerr medium between them. A Kerr medium is a plate of nonlinear optical material, exploiting birefringence (existence of different refractive indices for different directions of polarization of light propagating through material) when an external electric field is applied. If the electric field (so-called gating electric field) of appropriate intensity and polarization is applied, difference in ordinary and extraordinary indices of refraction can be set to such value for which the Kerr medium acts as a half-wave plate, changing the polarization direction of the incident light at the exit by 45°. Such polarized light can now pass through the second polarizer, and finally reach the detector. When there is no need to collect photons (Kerr gate is closed), nothing is happening with the Kerr medium, since the gating electric field is turned off, and two polarizers, which have mutually perpendicular axes of polarization do not allow any light to exit the Kerr gate. However, when there is need to open the gate and collect the photons, a very short pulse of the gating electric field is applied, inducing the abovementioned anisotropy in the Kerr medium and allowing the light to pass through the second polarizer and be collected at the detector. The temporal resolution is of the order of $\sim 4\,\mathrm{ps}$ [14, 15]. A key drawback of this approach is the short achievable duration of the temporal

gate, causing a very poor light harvesting in the case of Diffuse Raman, where the photon temporal spread is of the order of ns.

1.4.2 Gated Camera

In realizations of Izake et al. [16, 17] and of Ariese et al. [18], for time gating, an intensified charge-coupled device (ICCD) was used. In comparison to Kerr gating, this requires less complex systems and there is no need for high intensity pulsed lasers. However, the gate temporal width is of the order of $\sim 100\,\text{ps}$. Intensified CCD is a CCD camera with an image intensifier placed in front of it. Image intensifier consists of a photocathode, micro-channel plate (MCP) and a phosphor screen. When light falls on the photocathode, photoelectrons are emitted and accelerated towards the micro-channel plate by the application of appropriate voltage between the photocathode and MCP. Depending on the gate control signal, that voltage can be set to accelerate electrons towards the MCP, or to stop them and return to the photocathode. In the latter case, the gate is off, and thus no electrons arrive to the MCP, so in the end, no photons will reach the CCD detector. In the opposite case, CCD normally collects the photons emitted from the phosphor screen, and we say that the gate is on.

1.4.3 Time-Correlated Single-Photon Counting (TCSPC)

Since Raman signals are relatively weak, a Time-Correlated Single-Photon Counting approach (TCSPC) is quite interesting for Diffuse Raman applications, because of the sensitivity down to a single-photon level. The first implementation was proposed by Pogue et al. [19], yet with a simple and poorly performing system. Later on, a system based on TCSPC camera that simultaneously acquires both spectral and temporal information of Raman photons, was proposed by Konugolu et al. [20]. It has many advantages over previously discussed realizations of Diffuse Raman time domain techniques, in terms of signal-to-noise ratio, detection efficiency and compactness of the system. Great advantage of this system is that both Raman spectrum and temporal profile are acquired in a single measurement, thanks to the TCSPC camera. Gating can be performed in the post processing, where it is possible to choose the width of temporal gates, their start and end times. This is exactly what will be further elaborated in Chapter 4, where we are going to deal with the experimental data obtained on this system. More details about the technical specifications of the time resolved single photon counting camera and accompanying hardware will be presented in Section 4.1. Here we will just briefly introduce the idea of TCSPC.

Upon a short laser pulse excitation, the time interval between the pulse and the single photon detection is recorded, due to fast electronics. This process is repeated

with new laser pulses, until a certain number of photons is detected. The time intervals between the pulses and the corresponding detected photons are stored. This way, a histogram of photon arrival times is formed. For a measurement of the order of minutes, it is possible to acquire enough number of photon counts to statistically reliably represent the time resolved curve of photon time of flights from the source to the detector. This curve is also spectrally resolved.

TCSPC hardware enabled unpredictable application of Time Domain Diffuse Raman Spectroscopy theory. At the time of the Konugolu et al. paper (2018) [20], information on temporal gates was used in a way discussed in theoretical introduction in the previous sections, however, from an empirical point of view, as it is the case also with other realizations described so far. Spectra are reconstructed and ascribed to the bottom or to the top layer of the heterogeneous medium, depending on the time gates from which they are retrieved. What will be shown in this thesis work, is that there is a more rigorous way to treat the obtained associated temporal and spectral information.

1.4.4 Compressive Sensing

The three main technical needs: video-rate speeds spectroscopy, low phototoxicity, and coverage of a full vibrational spectrum, could be efficiently fulfilled by the application of a compressive sensing technique. [21]. A Digital Micromirror Device (DMD) is added to a conventional spectrometer in order to select which photons, according to their wavelengths, are allowed to fall on the single-pixel detector. This can be understood as a binary mask, or a matrix with ones and zeros, representing which wavelengths (columns) at which time instants (rows) are passed to the detector. This matrix, called Hadamard matrix, acts as a transition matrix on a real input spectrum, producing the output spectrum in other domain, called Hadamard's domain. The input signal is multiplexed, since the signals from many wavelengths are summed at the detector. An integration of signal over different wavelengths increases the signal-to-noise ratio, which is beneficial for Raman Spectroscopy. The time required to obtain a satisfactory level of useful signal is thus shortened. Moreover, the size of the information stored per unit time is decreased, since the dimension of data is reduced by exploiting the sparsity of the input. That is why we say it is a compressing technique. In such a way, the acquisition rate is increased. Only important informational content is stored, but with the simple reconstruction method it can be reliably retrieved. For the retrieval of the original spectrum, an inverse of the transition matrix is applied. If we think about mathematics more generally, which is also useful for easier understanding, this whole process is analogous to the Fourier transform. A realization of the compressive sensing system for depth-sectioning of two-layer tissue mimicking phantom is reported in [22].

1.5 Applications

With definition of diffusive media from the very beginning of this introduction and with already thoroughly discussed nature of Diffuse Optics, then with an insight into Raman Spectroscopy information content, it becomes clear that the range of potential applications is very wide. Of course, current applications will always be dependent on the technical advancements, not only the theory. Here we will provide a review of some of the most interesting applications and, in general, fields where the Diffuse Raman Spectroscopy is used (or could be used).

1.5.1 Clinical Diagnostics

Many laboratories are currently investigating potential medical applications of the Diffuse Raman Spectroscopy. It is still in perspective, since the already discussed techniques are relatively new and, although promising, at an early stage of development. Examples include: noninvasive diagnosis of breast cancer, in order to make rapid and more reliable detection and classification, thanks to chemical specificity [5], then determination of cancer margins during the cancer removal surgery [23], bone disease diagnosis through soft tissue in vivo (including information on both organic and inorganic components) or even tomographic approach for bone imaging [24]. The paper from Cordero et al. [25] gives recent and very detailed review on clinical in vivo applications of Raman Spectroscopy, covering noninvasive diagnostics on: cardiovascular diseases, inflammatory diseases, and, of course, lung, breast, digestive and urinary tract, brain and skin cancer. The group of Matoušek and Stone has very recently provided an up-to-date review on SORS applications in this field [26]. Another interesting technique, called Universal Multiple Angle Raman Spectroscopy (UMARS), firstly demonstrated by Umapathy et al, could in future bring Raman tomography as a tool for disease diagnostics [27].

1.5.2 Cultural Heritage

Identification of materials used in cultural heritage objects and monuments, as well as the investigation of their decay is very important goal of the conservation science. Typical structure of these materials is multi-layered, with micrometer thickness of layers, positioned over a few-millimeter-thick substrate. Nondestructiveness of Diffuse Raman Spectroscopy and its capability to separate layers (for very small thicknesses and superficial layers, micro-SORS is convenient [28]) opens new possibilities in the field of conservation science, as it was confirmed by Conti et al. [29]. As a requirement for many cultural sites, portable device should be developed, and there are already some results in this field [30, 31].

1.5.3 Security

Nowadays, development of robust security screening with great chemical specificity is highly desirable. In the work of Eliasson et al. [32], SORS showed ability to penetrate through non-metallic containers and retrieve highly chemically specific information. According to [33], SORS instruments are already applied at the airports worldwide, to scan the essentials taken on board for the flights. Another interesting application comes from the combination of space and time resolved Diffuse Raman approach [17]. This enabled screening of the potential explosives through containers under ambient light, which impact on the useful signal is suppressed by temporal gating. This method was also applied for the stand-off detection of explosives, through containers, at distances greater than 10 m, under ambient light. [16].

1.5.4 Pharmaceuticals

The analysis of unopened pharmaceutical products was made available by SORS techniques. It is possible to detect the counterfeit drugs in sealed bottles as demonstrated by Eliasson and Matoušek [34]. Not only the chemical fingerprint, but also the quantity of active pharmaceutical ingredients in pharmaceutical formulations could be assessed by applying the SORS through packaging, as shown by Olds et al. [35]. Since the "chemical identity check" is a regulatory requirement, this process has to be done, but unfortunately usually invasively, by opening the sampled packages, which makes the production process slower and more expensive, and also could possibly affect the pharmaceuticals being in contact with the environment. Another interesting field for the application of TRS is this. Recent advances in the analysis of pharmaceuticals using TRS are reviewed in the paper of Griffen et al [36].

1.5.5 Food

Also in the field of food analysis, noninvasive, subsurface and chemically precise analysis of the samples is needed. Qin et al. demonstrated the potential of SORS to quantify the lycopene content of intact tomatoes and to monitor their ripening [37]. Another interesting application is the usage of hand held SORS device to examine spirit drinks through bottle by means of counterfeiting and also with possibility of discriminating between different brands [38]. Ability to monitor methanol presence at concentrations well below the maximum human tolerable level was also demonstrated.

1.6 Overview of the Thesis Work

This first chapter has provided a basic introduction on the physics of the photon propagation in diffusive media and information content of the Raman Spectroscopy. Moreover, standard techniques in different domains and applications of the joint of the two fields, which we shortly call Diffuse Raman, are summarized.

In the following chapters, we start with the rigorous theoretical modelling of the Diffuse Raman in time domain. It will include well known results from the Diffuse Optics combined with the Raman correction derived by the heuristic approach for homogeneous media. Then, to obtain an appropriate model to solve our problem of the reconstruction of the spectra of two layers, this heuristic approach will be adapted for the two-layer media. The rigorous linear model is the key novelty. It will enable simple and quick retrieval of the spectra of both layers, when measurements are known, by finding the least square solution of the overdetermined system of linear equations.

The methods will be tested in Chapter 3 and Chapter 4. Firstly on the simulations, where the reader will find the analysis of results of the systematic study on effect of the specific parameters. The conclusions drawn will help us to better understand the limitations and capabilities of the method. However, final conclusions can only be made after the reconstruction performed on the real measurements data. The measurement data was provided by S. Konugolu and Prof. Pifferi on the experiments performed in 2017, with the specific hardware [20]. It will be shown that the new model and approach work also on real experimental data, despite the non-negligible background fluorescence signal. A few methods for the background removal from the reconstructed spectra will be presented, although there are many others that can be applied. Other limitations and perspectives will be discussed finally in Chapter 5.

Chapter 2

Modelling of Time-Domain Diffuse Raman

In accordance with the general idea of this thesis work, which is the reconstruction of Raman spectra of the two-layer diffusive media, relying on the information recorded in the time domain, it is required to obtain the models which will accurately describe the temporal evolution of the Raman signal depending on the optical and geometrical parameters of the medium considered. Our approach will be rigorous, not empirical, and here we will present and motivate its theoretical foundations. This rigorous approach to the reconstruction of the two-layer spectra is the key novelty and we are going to perform the reconstruction on simulated measurements (in Chapter 3) and real measurements (in Chapter 4) to see its effectiveness and limitations.

To reach the final goal, in this chapter we start with the detailed mathematical modelling of photon propagation processes in Time Resolved Diffuse Raman Spectroscopy. First sections will cover general Diffuse Optics models and equations. Then, additionally Raman scattering processes will be considered for homogeneous medium case. Everything exposed by that point is very well known in literature [1],[39]. However, what follows is the new application of the heuristic approach to treat photon propagation with Raman scattering processes in two-layer diffusive media. This relatively simple for the Diffuse Raman case, but rigorous theoretical model was suggested by Prof. Martelli [40]. The approach and corresponding models that follow from it are fundamental for the successful reconstruction of the two-layer Raman spectra. Namely, the rigorous solution of the Diffuse Raman forward problem in time domain provides us with a tool to access the reconstruction of unknown spectra, by solving the inverse problem, in which the time-resolved Raman signal measurements are known.

To run the simulations and perform the reconstruction either on simulated or

real experimental data, specific computer programs were developed. Insight in them will be given in the end of this chapter, through block-schemes representing the algorithms and their flow.

Before beginning with the theory, we will motivate the decision which one, among many approaches, to follow and which models to use.

2.1 Motivation

We have already seen that Time Resolved Diffuse Raman techniques have great potential and the information that could be retrieved would be extremely beneficial for the field of medical diagnostics. Here we will focus on diffusive media, which biological tissues are. What is fundamental to make the Time Resolved Diffuse Raman system work in practice? Besides the hardware which should be compact, reliable and, ultimately, cheap, as discussed in Chapter 1, another very important aspect is appropriate theoretical modelling. Development of rigorous theoretical models that will be used in solving the inverse problems is essential for expanding the boundaries of successful applications.

To be as formal as possible, in the following sections detailed insight into Diffuse Optics, from Transport Theory to Diffusion Approximation, will be given. One may ask why we decided to follow this line of thought, instead of strict application of Maxwell's equations. The answer is simple, practical results are obtained with the Diffusion Equation, while Maxwell's equations, although fundamental and universal, still have not, apart from few specific attempts, produced practical results in the field [1]. Moreover, Transport Theory and Diffusion Approximation will serve as the basis for what will come right after, when Raman effect will be introduced. To model the Raman scattering in compliance with the Diffusion Equation, we will follow the so-called heuristic approach. Briefly summarizing the concept, this approach takes advantage of the solution of the Diffusion Equation applied for a two-layer medium with addition of Raman correction. This correction takes into account Raman scattering in a very simple way, relying on the statistical nature of the phenomenon and expected photon's time of flight, or in other words, travelled pathlength. Such obtained equations for Raman scattering coefficients of the two layers are linear, which allows safe solution of the inverse problem in terms of computational effort.

When discussing about the computational cost, another approach, much more expensive would be to use the Monte Carlo simulations. They are used in research as "gold standard" [28], [39], but if we want to pave the way for practical applications in future, much faster methods are to be developed. Once again, since the main goal is to make reliable, compact, fast and cheap system, we will pursue this path of theoretical modelling, explained in the previous paragraph and thoroughly

elaborated in the following sections.

2.2 Transport Theory and Diffusion Approximation

In this section we are going to define the main quantities used to describe the photon migration through diffusive media. Moreover, precise mathematical formulation of two fundamental equations will be given. The first one, very general is the Radiative Transfer Equation (RTE), an integro-differential equation which does not have an analytical solution in closed form. Because of the computational complexity required to solve this equation, a more practical equation for treating multiple scattering phenomena in highly scattering media is the Diffusion Equation (DE), a partial differential equation, which follows from RTE when some assumptions, explained in Section 2.2.6, are met. The theoretical background and presentation approach relies on the content of the book from Zaccanti, Martelli et al. [1].

2.2.1 Optical properties

As already discussed in Chapter 1, two characteristic processes that photons undergo while propagating through turbid media are absorption and scattering. Different from the Section 1.1.1 where a more phenomenological and intuitive definitions of absorption and scattering coefficients were given, here we are going to be formal, since further sections will require precise theoretical setup. Moreover, scattering phase function, reduced scattering coefficient and extinction coefficient will be defined.

Absorption coefficient is defined as the ratio between the power absorbed per unit volume and the power incident per unit area (see Figure 2.1):

$$\mu_a = \frac{\mathrm{d}P_{abs}/\mathrm{d}V}{P/S} = \frac{\mathrm{d}P_{abs}}{P\mathrm{d}l}. \tag{2.1}$$

Here we can immediately write $\mathrm{d}P_{abs} = \mu_a \mathrm{d}lP$. Considering that $\mathrm{d}P_{abs} = -\mathrm{d}P$, differential equation for the power $\mathrm{d}P(l) = -\mu_a P(l)\mathrm{d}l$ is obtained. The solution is: $P(l) = P_0 e^{-\mu_a l}$ for some initial power P_0 entering the medium. The assumption here is that the medium is homogeneous and the light travels distance l through it. Moving to the intensities, exactly the Beer-Lambert law is derived: $I(l) = I_0 e^{-\mu_a l}$, where I_0 is the initial intensity of light, before propagating through the medium.

Scattering coefficient μ_s, analogously to the absorption coefficient, is defined as the ratio between the power scattered (photons changed the direction of propagation) per unit volume and the power incident per unit area. Another function required to describe scattering is the scattering phase function $p(\hat{s}, \hat{s}')$. The scattering phase

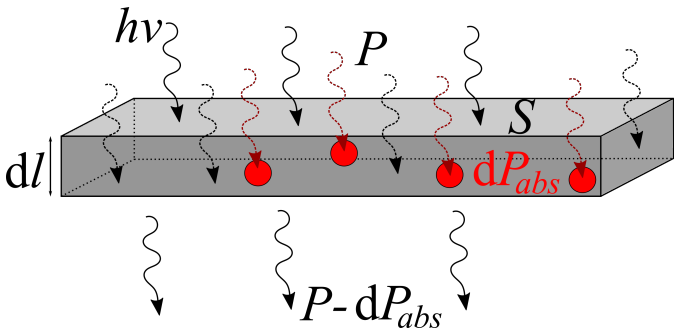

Figure 2.1: Photons with energy $h\nu$ and total power P falling on the area S. Some of them, with total power $\mathrm{d}P_{abs}$ are absorbed by molecules of the medium (red). The remaining power after distance $\mathrm{d}l$ is $P - \mathrm{d}P_{abs}$.

function represents the probability that a photon, travelling along direction $\hat{s}$, is scattered within a unit solid angle around the direction $\hat{s}'$. The scatterers are isotropic, if the scattering phase function does not depend on absolute directions $\hat{s}$ and $\hat{s}'$, but only on angle θ between them (scattering angle, see Figure 2.2): $p(\hat{s}, \hat{s}') = p(\theta)$. The following normalization condition holds

$$\int_{4\pi} p(\hat{s}, \hat{s}')\mathrm{d}\Omega' = 2\pi \int_0^{\pi} p(\theta) \sin\theta \mathrm{d}\theta = 1. \tag{2.2}$$

Asymmetry factor g is defined as the average of the cosine of scattering angle:

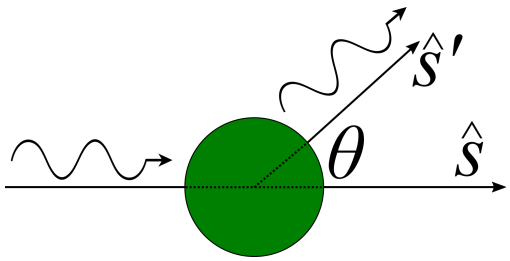

Figure 2.2: Photon scattering by angle θ.

$$g = \langle \cos\theta \rangle = 2\pi \int_0^{\pi} \cos\theta p(\theta) \sin\theta \mathrm{d}\theta. \tag{2.3}$$

Based on this, the reduced scattering coefficient is

$$\mu_s' = (1 - g)\mu_s. \tag{2.4}$$

The fraction of power extracted in a unit volume by scattering or absorption is described by the extinction coefficient $\mu_t = \mu_a + \mu_s$.

2.2.2 Radiometric Quantities

Firstly, we are going to define the spectral radiance (or the spectral specific intensity). The spectral radiance $I_s(\vec{r}, \hat{s}, t, \nu)$ is equal to the average power that, at position $\vec{r}$ and time instant t, flows through the unit area oriented in the direction of the unit vector $\hat{s}$, carried by the photons from unit interval of frequencies around ν and unit solid angle around $\hat{s}$. From the definition, it is clear that the unit for spectral radiance is $\mathrm{Wm^{-2}sr^{-1}Hz^{-1}}$.

According to this definition, the power $\mathrm{d}P$ [W] that flows through elementary area $\mathrm{d}S$, oriented in direction of unit vector $\hat{n}$, at the position $\vec{r}$ and time instant t, due to the photons from infinitesimal solid angle $\mathrm{d}\Omega$ around $\hat{s}$ and very narrow interval of frequencies $(\nu, \nu + \mathrm{d}\nu)$ is (see Figure 2.3)

$$\mathrm{d}P = I_s(\vec{r}, \hat{s}, t, \nu)\, |\hat{n} \cdot \hat{s}|\, \mathrm{d}S \mathrm{d}\Omega \mathrm{d}\nu. \tag{2.5}$$

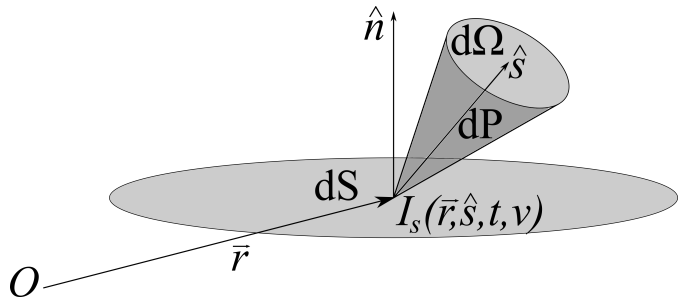

Figure 2.3: Geometrical representation of vectors $\vec{r}$, $\hat{s}$, $\hat{n}$ from equation (2.5) in space.

The relation between the energy density $\mathrm{d}w$ [$\mathrm{J/m^3}$], at position $\vec{r}$ and time instant t, of the photons travelling in direction $\hat{s}$, subtended by infinitesimal solid angle $\mathrm{d}\Omega$ around $\hat{s}$ and with frequencies from narrow interval $(\nu, \nu + \mathrm{d}\nu)$ now becomes obvious:

$$\mathrm{d}w = \frac{\mathrm{d}P\mathrm{d}t}{\mathrm{d}V} = \frac{\mathrm{d}P\mathrm{d}t}{\mathrm{d}S v \mathrm{d}t} = \frac{I_s(\vec{r}, \hat{s}, t, \nu)\mathrm{d}\Omega\mathrm{d}\nu}{v}, \tag{2.6}$$

where v is the speed of light in the medium.

We assume the frequency of radiation does not change during light propagation through medium. If we have a (quasi-)monochromatic source of radiation, then, instead of specifically referring to spectral radiance, we may use just radiance, an integral of spectral radiance over a narrow band of frequencies $(\nu - \Delta\nu/2, \nu + \Delta\nu/2)$

around source frequency ν:

$$L(\vec{r},\hat{s},t) = \int_{\nu-\Delta\nu/2}^{\nu+\Delta\nu/2} I_s(\vec{r},\hat{s},t,\nu)\mathrm{d}\nu. \tag{2.7}$$

It is evident from equation (2.6) that the radiance $L(\vec{r},\hat{s},t)$ [$\mathrm{Wm^{-2}sr^{-1}}$] is proportional to the number of photons of energy $h\nu$ (h is Plancks's constant) from an infinitesimal solid angle $\mathrm{d}\Omega$ around direction $\hat{s}$, passing, at time instant t and at position $\vec{r}$, through elementary area $\mathrm{d}S$ oriented along $\hat{s}$. Note that from now on, we will consider only one frequency ν for all quantities that are going to be defined, as it was the case with radiance. Basically, the assumption is that the light source is monochromatic and the medium (still) cannot change the wavelength of photons, i.e. the scattering processes are elastic. This will be true until we take into consideration also the Raman scattering in Section 2.3

We now define the fluence (or irradiance) as the total power of photons crossing (or falling onto) the unit surface at position $\vec{r}$ and time instant t. It can be obtained as an integral of radiance over the entire solid angle:

$$\Phi(\vec{r},t) = \int_{4\pi} L(\vec{r},\hat{s},t)\mathrm{d}\Omega. \tag{2.8}$$

Combining the definitions of radiance and spectral radiance, and equations for the fluence (2.8) and for the elementary energy density (in solid angle $\mathrm{d}\Omega$ and frequency interval $(\nu,\nu+\mathrm{d}\nu)$) (2.6) we can relate the fluence Φ [$\mathrm{Wm^{-2}}$] with the energy density w [$\mathrm{Jm^{-3}}$]:

$$w(\vec{r},t) = \frac{\Phi(\vec{r},t)}{v}. \tag{2.9}$$

If we divide the energy density by the energy of a single photon $h\nu$, we obtain the photon density, i.e. number of photons in unit volume, at position $\vec{r}$ and time t

$$u(\vec{r},t) = \frac{w(\vec{r},t)}{h\nu} = \frac{\Phi(\vec{r},t)}{h\nu v}. \tag{2.10}$$

Therefore, photon density is proportional to the fluence.

Similarly to the fluence, another quantity which will be used in formulations of our equations in the following sections, is the flux vector [$\mathrm{W/m^2}$], defined as directed net flux of power crossing unit area at position $\vec{r}$ and time t:

$$J(\vec{r},t) = \int_{4\pi} L(\vec{r},\hat{s},t)\hat{s}\mathrm{d}\Omega. \tag{2.11}$$

2.2.3 Radiative Transfer Equation (RTE)

To quantify the photon migration through the medium, we can look for density of photons, fluence or radiance, in any point of space and time. We will formulate the RTE for radiance, as the most fundamental among these quantities.

If we consider what happens with the energy of photons in an elementary volume $\mathrm{d}V$ in a given direction $\hat{s}$, within infinitesimal solid angle $\mathrm{d}\Omega$, during infinitesimal time interval $\mathrm{d}t$, we may identify the following factors:

- temporal change of energy: $\left[\frac{\partial}{v\partial t}L(\vec{r},\hat{s},t)\right]\mathrm{d}V\mathrm{d}\Omega\mathrm{d}t$;
- net flux of energy: $\hat{s}\left[\nabla L(\vec{r},\hat{s},t)\right]\mathrm{d}V\mathrm{d}\Omega\mathrm{d}t$;
- energy extracted by absorption and scattering: $\mu_t L(\vec{r},\hat{s},t)\mathrm{d}V\mathrm{d}\Omega\mathrm{d}t$;
- energy increase due to photons scattered from another direction $\hat{s}'$ to the direction of interest $\hat{s}$: $\left[\mu_s\int_{4\pi}p(\hat{s},\hat{s}')L(\vec{r},\hat{s}',t)\mathrm{d}\Omega'\right]\mathrm{d}V\mathrm{d}\Omega\mathrm{d}t$;
- energy generated by sources: $\varepsilon(\vec{r},\hat{s},t)\mathrm{d}V\mathrm{d}\Omega\mathrm{d}t$.

Writing the energy balance along a specific direction $\hat{s}$, in differential form, we obtain the Radiative Transfer Equation

$$\frac{\partial}{v\partial t}L(\vec{r},\hat{s},t)+\nabla\left[\hat{s}L(\vec{r},\hat{s},t)\right]+\mu_t L(\vec{r},\hat{s},t)=\mu_s\int_{4\pi}p(\hat{s},\hat{s}')L(\vec{r},\hat{s}',t)\mathrm{d}\Omega'+\varepsilon(\vec{r},\hat{s},t). \tag{2.12}$$

Here v is the speed of light in the medium, μ_t, μ_s and $p(\hat{s},\hat{s}')$ are defined in Section 2.2.1 and all other quantities are defined in Section 2.2.2.

2.2.4 Green's Function Solution

Since the Radiative Transfer Equation is a linear equation for radiance (or fluence, or photon density), the superposition principle can be applied. Namely, if we can represent the excitation (source term) as a sum of different excitations (sources), then the response (solution) is also sum of different responses (solutions), each as a result of corresponding single excitation (source) [41]. The use of a general term excitation here refers to a source term from equation (2.12), while a general term response, more specifically in the same equation could be replaced with the solution for radiance.

If the source term from equation (2.12) is a unitary Dirac delta function (in space, time and direction domains)

$$\varepsilon(\vec{r},\hat{s},t)=\delta^3\left(\vec{r}-\vec{r}'\right)\delta\left(\hat{s}-\hat{s}'\right)\delta\left(t-t'\right), \tag{2.13}$$

then the solution of the equation (2.12) is the Green's function of the problem. Green's function method consists of expressing the source as the sum of Dirac delta functions, and then, knowing the solution for one Dirac delta, it is possible to express the solution for the sum of delta functions, exploiting the properties of

linearity. For very precise divisions this sum becomes an integral. If we denote with $L(\vec{r}, \vec{r}', \hat{s}, \hat{s}', t, t')$ the solution when the source is $\delta^3(\vec{r} - \vec{r}')\,\delta(\hat{s} - \hat{s}')\,\delta(t - t')$, then the final solution of RTE to an arbitrary source defined in spatial, temporal and solid angular domain as $\varepsilon(\vec{r}', \hat{s}', t')$ for all $\vec{r}'$, $\hat{s}'$, and t', is given by the following integral over the whole spatial V, temporal $(-\infty, +\infty)$ and solid angular 4π domain:

$$L(\vec{r}, \hat{s}, t) = \int_V \int_{4\pi} \int_{-\infty}^{+\infty} L(\vec{r}, \vec{r}', \hat{s}, \hat{s}', t, t')\varepsilon(\vec{r}', \hat{s}', t')\mathrm{d}\vec{r}'^3\mathrm{d}\Omega' dt'. \tag{2.14}$$

2.2.5 Absorption and Mean Time of Flight

In this section, we are going to see how the absorption modifies the solution of the RTE and how we can relate the time that photons spend in different layers of multi-layered media or, in general, any media that can be divided in different regions, not necessarily layers.

For the beginning, let us assume a medium with homogeneous absorption $\mu_a(\vec{r}) = \mu_a$. If $L_0(\vec{r}, \hat{s}, t)$ is the solution of the equation (2.12) for the non-absorbing medium ($\mu_a = 0$), when the source term is Dirac delta in time $\varepsilon(\vec{r}, \hat{s}, t) = S(\vec{r}, \hat{s})\delta(t)$, then the solution for absorbing medium (with absorption coefficient μ_a) is

$$L_{\mu_a}(\vec{r}, \hat{s}, t) = L_0(\vec{r}, \hat{s}, t)e^{-\mu_a v t}. \tag{2.15}$$

This statement immediately follows from the equation (2.12), after substituting $L_{\mu_a}(\vec{r}, \hat{s}, t)$ with $L_0(\vec{r}, \hat{s}, t)e^{-\mu_a v t}$ and applying $\varepsilon(\vec{r}, \hat{s}, t) = 0$ when $t \neq 0$ and $L_{\mu_a}(\vec{r}, \hat{s}, t) = L_0(\vec{r}, \hat{s}, t)$ when $t = 0$. One conclusion we may draw at this point is that, in case of a homogeneous absorption, the RTE can be solved first for non-absorbing medium, and then the correcting exponentially decaying factor should be added to obtain the final solution.

Let us, instead, consider an inhomogeneous medium with different regions, represented by union of disjoint volumes V_i. Furthermore, in each region we assume constant absorption μ_{ai} over whole volume V_i. To determine the mean time of flight, or in other words, mean time that photons spend in volume V_i, we may perform the following reasoning. We consider a temporal Dirac delta function as a source and detected radiance $L_{\mu_{ai}}(\vec{r}, \hat{s}, t)$ at some point $\vec{r}$, at time instant t measured from the beginning of photons propagation. The index μ_{ai} refers to the scenario where the region V_i has non-zero absorption coefficient. On the contrary, if the absorption of the region V_i is $\mu_{ai} = 0$, then the radiance is $L_0(\vec{r}, \hat{s}, t)$. Let $f(t_i, t)$ be the probability density function for random variable t_i, time that photon spends in region V_i, knowing that the total propagation time (through all regions) is t. Exploiting the equation (2.15) and probability density function for t_i, we may

write

$$L_{\mu_{ai}}(\vec{r},\hat{s},t) = L_0(\vec{r},\hat{s},t)\int_0^t f(t_i,t)e^{-\mu_{ai}v_it_i}\mathrm{d}t_i, \tag{2.16}$$

where v_i is the speed of light in region V_i. Mean time of flight through region V_i can be expressed in the following way

$$\langle t_i\rangle = \frac{\int_0^t t_i f(t_i,t)e^{-\mu_{ai}v_it_i}\mathrm{d}t_i}{\int_0^t f(t_i,t)e^{-\mu_{ai}v_it_i}\mathrm{d}t_i} \tag{2.17}$$

Note that

$$\frac{\partial}{\partial\mu_{ai}}\int_0^t f(t_i,t)e^{-\mu_{ai}v_it_i}\mathrm{d}t_i = -v_i\int_0^t t_i f(t_i,t)e^{-\mu_{ai}v_it_i}\mathrm{d}t_i. \tag{2.18}$$

Combining the equations (2.16) and (2.18) and returning to (2.17), the following expression for the mean time of flight in region V_i is obtained

$$\langle t_i\rangle = \frac{-\frac{1}{v_i}\frac{\partial}{\partial\mu_{ai}}\left[\frac{L_{\mu_{ai}}(\vec{r},\hat{s},t)}{L_0(\vec{r},\hat{s},t)}\right]}{\frac{L_{\mu_{ai}}(\vec{r},\hat{s},t)}{L_0(\vec{r},\hat{s},t)}} = -\frac{1}{v_iL_{\mu_{ai}}(\vec{r},\hat{s},t)}\frac{\partial L_{\mu_{ai}}(\vec{r},\hat{s},t)}{\partial\mu_{ai}}. \tag{2.19}$$

This result would be of interest when considering two-layer medium and average times that photons spend in each of the two layers before being detected at time t. Instead of radiance, it is possible to use fluence or power detected or other quantities as it will be seen in Section 2.4.

2.2.6 Diffusion Approximation

As previously said, there is no general analytical solution for the RTE. Solving this integro-differential equation is based on numerical methods and for the retrieval of the solutions usually great computational effort is needed. That is the reason why simpler methods or equations that appropriately describe photon propagation process are to be found, whenever possible.

In diffusive media, where photons undergo many scattering events, diffusion approximation is applied. This approximation consists of two assumptions:

- Radiance inside a diffusive medium is almost isotropic:

$$L(\vec{r},\hat{s},t) = \alpha\Phi(\vec{r},t) + \beta\vec{J}(\vec{r},t)\cdot\hat{s}, \tag{2.20}$$

where constants α and β will be determined later. The first term is isotropic and the second is linearly anisotropic. This approximation is good if the second term is much smaller then the first.

- Time change of flux vector $\vec{J}(\vec{r},t)$ over a time interval $\Delta t = \dfrac{1}{v\mu_s'}$ is negligible in comparison to the flux vector itself:

$$\frac{1}{v\mu_s'}\left|\frac{\partial J(\vec{r},t)}{\partial t}\right| \ll \left|J(\vec{r},t)\right|. \tag{2.21}$$

Let us determine α and β from (2.20). From the definition equation for the fluence (2.8), in isotropic approximation immediately follows that $\alpha = \dfrac{1}{4\pi}$. To find β, we start with the following: $\left|\vec{J}(\vec{r},t)\right| = \vec{J}(\vec{r},t)\cdot\hat{s}_J$, where $\hat{s}_J$ is the unit vector in direction of $\vec{J}(\vec{r},t)$. Substituting radiance from equation (2.20) to (2.11) we obtain

$$\left|\vec{J}(\vec{r},t)\right| = \frac{1}{4\pi}\int_{4\pi}\Phi(\vec{r},t)\hat{s}\cdot\hat{s}_J\mathrm{d}\Omega + \beta\int_{4\pi}\left(\vec{J}(\vec{r},t)\cdot\hat{s}\right)\cdot(\hat{s}\cdot\hat{s}_J)\,\mathrm{d}\Omega, \tag{2.22}$$

which simplifies to

$$\left|\vec{J}(\vec{r},t)\right| = \frac{\Phi(\vec{r},t)}{4\pi}\hat{s}_J\cdot\int_{4\pi}\hat{s}\mathrm{d}\Omega + \beta\left|\vec{J}(\vec{r},t)\right|\int_{4\pi}(\hat{s}\cdot\hat{s}_J)^2\mathrm{d}\Omega. \tag{2.23}$$

The first term is equal to zero, while for the second we have

$$\left|\vec{J}(\vec{r},t)\right| = \beta\left|\vec{J}(\vec{r},t)\right| = \int_0^{2\pi}\mathrm{d}\varphi\int_0^{\pi}\cos^2\theta\sin\theta\mathrm{d}\theta, \tag{2.24}$$

which implies $1 = \beta\cdot 2\pi\cdot\dfrac{2}{3}$ and finally $\beta = \dfrac{3}{4\pi}$. Now, the equation (2.20) is complete:

$$L(\vec{r},\hat{s},t) = \frac{1}{4\pi}\Phi(\vec{r},t) + \frac{3}{4\pi}\vec{J}(\vec{r},t)\cdot\hat{s}, \tag{2.25}$$

With this, we have enough pieces to obtain the Diffusion Equation. In the following section, the derivation will be presented. However, some mathematical steps will be skipped, in order to make it easier to follow the main line of the derivation. These steps are not fundamental and include just solutions to some integrals.

2.2.7 Diffusion Equation (DE)

If we start from the RTE (2.12), multiply everything by $\hat{s}$ and integrate over the entire angular domain, the RTE becomes:

$$\begin{aligned}\int_{4\pi}\left\{\frac{\partial}{v\partial t}L(\vec{r},\hat{s},t)+\nabla\left[\hat{s}L(\vec{r},\hat{s},t)\right]+\mu_t L(\vec{r},\hat{s},t)\right\}\hat{s}\mathrm{d}\Omega \\ =\int_{4\pi}\left\{\mu_s\int_{4\pi}p(\hat{s},\hat{s}')L(\vec{r},\hat{s}',t)\mathrm{d}\Omega'-\varepsilon(\vec{r},\hat{s},t)\right\}\hat{s}\mathrm{d}\Omega.\end{aligned} \tag{2.26}$$

Here we can identify five main integrals:

$$I_1=\int_{4\pi}\frac{\partial}{v\partial t}L(\vec{r},\hat{s},t)\hat{s}\mathrm{d}\Omega=\frac{1}{v}\frac{\partial}{\partial t}\vec{J}(\vec{r},t); \tag{2.27}$$

$$I_2=\int_{4\pi}\left\{\hat{s}\cdot\nabla\left[\frac{1}{4\pi}\Phi(\vec{r},t)+\frac{3}{4\pi}\vec{J}(\vec{r},t)\cdot\hat{s}\right]\right\}\hat{s}\mathrm{d}\Omega=I_{2a}+I_{2b}, \tag{2.28}$$

where

$$I_{2a}=\int_{4\pi}\left\{\hat{s}\cdot\nabla\left[\frac{\Phi(\vec{r},t)}{4\pi}\right]\right\}\hat{s}\mathrm{d}\Omega=\frac{\nabla\Phi(\vec{r},t)}{3} \tag{2.29}$$

(since it can be shown that $\int_{4\pi}\left(\hat{s}\cdot\vec{A}\right)\hat{s}\mathrm{d}\Omega=\frac{4\pi}{3}\vec{A}$ for any vector $\vec{A}$ independent on direction $\hat{s}$) and

$$I_{2b}=0 \tag{2.30}$$

(since it can be demonstrated that $\int_{4\pi}\left[\hat{s}\cdot\nabla\left(\vec{A}\cdot\hat{s}\right)\right]\hat{s}\mathrm{d}\Omega=0$, for any vector $\vec{A}$);

$$I_3=\mu_t\int_{4\pi}L(\vec{r},\hat{s},t)\hat{s}\mathrm{d}\Omega=\mu_t\vec{J}(\vec{r},t); \tag{2.31}$$

$$I_4=\int_{4\pi}\left\{\mu_s\int_{4\pi}p(\hat{s},\hat{s}')\left[\frac{\Phi(\vec{r},t)}{4\pi}+\frac{3\vec{J}(\vec{r},t)}{4\pi}\cdot\hat{s}'\right]\mathrm{d}\Omega'\right\}\hat{s}\mathrm{d}\Omega=I_{4a}+I_{4b}, \tag{2.32}$$

where

$$I_{4a}=\int_{4\pi}\left\{\mu_s\int_{4\pi}p(\hat{s},\hat{s}')\frac{\Phi(\vec{r},t)}{4\pi}\mathrm{d}\Omega'\right\}\hat{s}\mathrm{d}\Omega=0 \tag{2.33}$$

and

$$I_{4b}=\int_{4\pi}\left\{\mu_s\int_{4\pi}p(\hat{s},\hat{s}')\frac{3\vec{J}(\vec{r},t)}{4\pi}\cdot\hat{s}'\mathrm{d}\Omega'\right\}\hat{s}\mathrm{d}\Omega=\mu_s g\vec{J}(\vec{r},t) \tag{2.34}$$

(where the asymmetry factor g is defined in 2.2.1 and to manipulate with emerging integrals, again one could use $\int\limits_{4\pi} \left(\hat{s} \cdot \vec{A}\right) \hat{s} \mathrm{d}\Omega = \frac{4\pi}{3}\vec{A}$ for any vector $\vec{A}$ independent on direction $\hat{s}$); the last term stays as it is:

$$I_5 = \int\limits_{4\pi} \varepsilon(\vec{r}, \hat{s}, t)\hat{s}\mathrm{d}\Omega. \tag{2.35}$$

Summing everything up we may write

$$\frac{1}{v}\frac{\partial}{\partial t}\vec{J}(\vec{r}, t) + \frac{\nabla\Phi(\vec{r}, t)}{3} + (\mu_t - g\mu_s)\vec{J}(\vec{r}, t) = \int\limits_{4\pi} \varepsilon(\vec{r}, \hat{s}, t)\hat{s}\mathrm{d}\Omega. \tag{2.36}$$

Taking advantage of the second assumption of the diffusion approximation (2.21), we may neglect the partial derivative of flux vector over time, so we obtain

$$\vec{J}(\vec{r}, t) = \frac{1}{\mu_t - g\mu_s}\left[-\frac{\nabla\Phi(\vec{r}, t)}{3} + \int\limits_{4\pi} \varepsilon(\vec{r}, \hat{s}, t)\hat{s}\mathrm{d}\Omega\right]. \tag{2.37}$$

If the source is isotropic, the previous equation is further simplified to

$$\vec{J}(\vec{r}, t) = -D\nabla\Phi(\vec{r}, t) \tag{2.38}$$

which is the standard form of the Fick's law of diffusion. Here $D = \frac{1}{3(\mu_t - g\mu_s)} = \frac{1}{3(\mu_a + \mu_s')}$ is the diffusion coefficient.

Radiative Transfer Equation (2.12) integrated over entire solid angle transforms into

$$\frac{\partial}{v\partial t}\Phi(\vec{r}, t) + \nabla \cdot \vec{J}(\vec{r}, t) + \mu_a\Phi(\vec{r}, t) = \int\limits_{4\pi} \varepsilon(\vec{r}, \hat{s}, t)\mathrm{d}\Omega, \tag{2.39}$$

which is known as the continuity equation. Applying the divergence operator on both sides of the equation (2.37) and substituting $\nabla \cdot \vec{J}(\vec{r}, t)$ into (2.39) we obtain the time-dependent Diffusion Equation

$$\left[\frac{1}{v}\frac{\partial}{\partial t} - \nabla \cdot (D\nabla) + \mu_a\right]\Phi(\vec{r}, t) = q_0(\vec{r}, t) \tag{2.40}$$

where

$$q_0(\vec{r}, t) = \int\limits_{4\pi} \varepsilon(\vec{r}, \hat{s}, t)\mathrm{d}\Omega - 3\nabla \cdot \left[D\int\limits_{4\pi} \varepsilon(\vec{r}, \hat{s}, t)\hat{s}\mathrm{d}\Omega\right] \tag{2.41}$$

is the source term. In case of a homogeneous medium, μ_a and μ_s' do not depend on coordinates, therefore diffusion coefficient D is constant:

$$\left[\frac{1}{v}\frac{\partial}{\partial t} - D\nabla^2 + \mu_a\right]\Phi(\vec{r},t) = q_0(\vec{r},t). \tag{2.42}$$

If the source is isotropic, i.e. $\varepsilon(\vec{r},\hat{s},t) = \varepsilon(\vec{r},t)$, then the second term in equation (2.41) is equal to zero and we may write

$$q_0(\vec{r},t) = 4\pi\varepsilon(\vec{r},t). \tag{2.43}$$

2.2.8 Solution for the Infinite Medium

First of all, we will provide the solution to a problem in infinite medium. This is very general case, without boundary condition constraints and will be used as an illustrative example how the density of photons propagate in space and time through unbounded diffusive media or any diffusive media in general, since this solution can serve as initial piece of the puzzle for other solutions.

In case of an infinite, homogeneous and diffusive medium in which speed of light is v, with absorption coefficient μ_a and reduced scattering coefficient μ_s', with diffusion coefficient defined as $D = \dfrac{1}{3\mu_s'}$ (where highly scattering medium is assumed, $\mu_a \ll \mu_s'$) and with isotropic source described with the following Dirac delta function in spatial and temporal domain

$$q_0(\vec{r},t) = \delta^3(\vec{r})\delta(t), \tag{2.44}$$

the solution to the Diffusion Equation (2.42) is given by [1]

$$\Phi(\vec{r},t) = \frac{v}{(4\pi Dvt)^{3/2}}\exp\left(-\frac{r^2}{4Dvt} - \mu_a vt\right), \tag{2.45}$$

where $r = |\vec{r}|$ is the distance from the source.

To solve other problems, where the medium is finite, i.e. where bounds and interfaces between two diffusive media or diffusive and non-scattering medium exist, of course, it is required to include boundary conditions. The most common are: Partial Current Boundary Condition (PCBC), Robin Boundary Condition, Extrapolated Boundary Condition (EBC), Zero Boundary Condition (ZBC); for more details, the reader is referred to: [1], [42], [43], [44], [45].

2.3 Diffuse Raman Solution for Homogeneous Case

So far we have only considered Tyndall or elastic scattering of photons while propagating through the scattering medium. At this place, we introduce the

Raman scattering to our model. In addition to all optical parameters used to formulate RTE and DE, we should consider also Raman scattering coefficient μ_{sR}, which will be defined analogously to the Tyndall (or elastic) scattering μ_s.

The idea of this section is to present the reasoning when solving problems of photon propagation in diffusive and Raman scattering media. For the beginning, let us consider a homogeneous medium, described with the following optical properties at the source emission wavelength λ: absorption coefficient μ_a, scattering coefficient μ_s, reduced scattering coefficient μ'_s and Raman scattering coefficient μ_{sR}. A speed of light propagation in the medium at wavelength λ is v. Note that this is the first time we will formally define the Raman scattering coefficient. In analogy with the elastic scattering, this coefficient will also quantify which fraction of incident power (or number of incident photons per unit time) to unit area is inelastically Raman scattered in a unit volume. The model is the same, scattering occurs when a photon hits the scatterer. However, the scattered photon will have different wavelength. The source emission wavelength is λ and it is the wavelength of photons prior to Raman scattering, while the Raman scattered (or re-emitted) wavelength is λ_e. Optical properties at λ_e are μ_{ae}, μ_{se}, μ'_{se}, μ_{sRe} and v_e, in the order of those defined at λ. Here we assume only one type of Raman scatterers which act only with one Raman shift on the incoming photons.[1] Moreover, multiple Raman scatterings that may theoretically occur to a single photon are to be neglected (practically, $\mu_{sRe} = 0$), since the Raman scattering coefficient is always a few orders of magnitude less than the scattering coefficient ($\mu_{sR} \ll \mu_s$). Basically, for a single photon, multiple Tyndall (elastic) scattering events will be allowed, but maximum of only one Raman scattering event will be considered. The whole section relies on the paper of Martelli et al. [39].

2.3.1 General Model of Raman Scattering

We can model our homogeneous medium as a homogeneous background medium with absorption μ_{ab}, scattering μ_{sb} and reduced scattering μ'_{sb} coefficients, optical characteristics at the source wavelength λ. To this background, Raman scattering molecules, evenly distributed in space, are superimposed. The background optical parameters at the Raman emission wavelength λ_e are μ_{abe}, μ_{sbe}, μ'_{sbe}.

In Figure 2.4 an example of photon path from the source at position $\vec{r}_s$ to the detector at position $\vec{r}$ is presented. The photon experienced many elastic Tyndall scattering events in the background medium and only one inelastic Raman scattering. This means that the wavelength of the detected photon is λ_e and it is

[1] This is not a limiting factor, since the Raman scatterig on multiple species can be obtained as a superposition of Raman scatterings on individual species. Multiple Raman shifts can be treated in the same way.

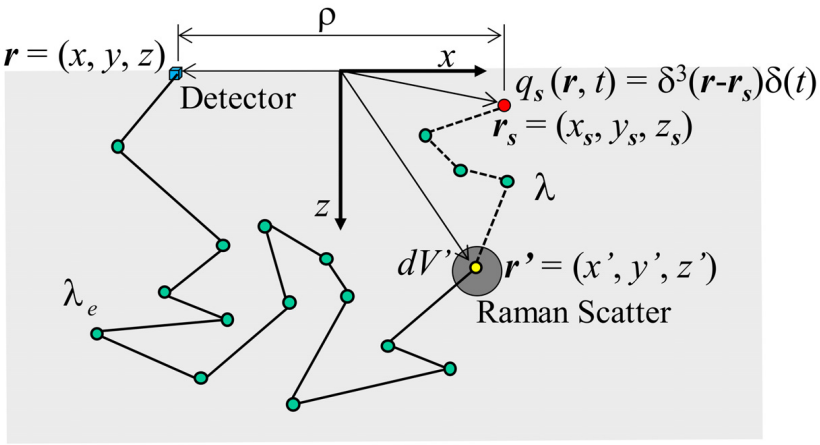

Figure 2.4: Photon path from source to detector trough the medium. Photon experienced multiple elastic Tyndall scatterings (on small circles) and one inelastic Raman scattering (on big circle). Figure taken from [39].

in accordance with the assumption $\mu_{sR} \ll \mu_s$, which allowed us to neglect multiple Raman scatterings of a single photon.

As Martelli et al. did in their paper [39], we will also consider each Raman scattering as an absorption of photon of wavelength λ and immediate emission of a photon at wavelength λ_e in random direction. Thus, the Raman scattering will be responsible for increased absorption of the medium at λ, and new photon generation at λ_e. The latter will have a role of the source of radiation at λ_e. This source will appear at different positions at different times.

We will apply Diffusion Equation (2.42) to model the photon propagation process. Since we have two wavelengths of interest λ and λ_e, we will have two coupled equations. The coupling comes from the fact that Raman emission at $(\vec{r}, t)$, described by $q_e(\vec{r}, t)$, is conditioned with the presence of photon of wavelength λ at position $\vec{r}$ and time instant t, described by the fluence $\Phi(\vec{r}, t)$. The equations for wavelengths λ and λ_e, respectively, are

$$\left[\frac{1}{v}\frac{\partial}{\partial t} - D\nabla^2 + \mu_a\right]\Phi(\vec{r}, t) = q(\vec{r}, t); \tag{2.46}$$

$$\left[\frac{1}{v_e}\frac{\partial}{\partial t} - D_e\nabla^2 + \mu_{ae}\right]\Phi_e(\vec{r}, t) = q_e(\vec{r}, t). \tag{2.47}$$

Here $D = \dfrac{1}{3\mu'_s}$, where $\mu'_s = \mu'_{sb}$ and $D_e = \dfrac{1}{3\mu'_{se}}$, where $\mu'_{se} = \mu'_{sbe}$. The only difference between the corresponding parameters on relation background medium - full medium (background with Raman scatterers) appears for the absorption

coefficient at λ. Raman scattering events act as absorption events for photons at λ, therefore $\mu_a = \mu_{ab} + \mu_{sR}$. From the definition of Raman scattering coefficient, number of Raman scattered photons at wavelength λ in a unit volume is equal to $\mu_{sR}\Phi(\vec{r}, t)$. On the other hand, from the definition of the source term, number of generated photons at wavelength λ_e in unit volume is equal to $q_e(\vec{r}, t)$. From the nature of Raman scattering, these two numbers are equal and hence we may write

$$q_e(\vec{r}', t') = \mu_{sR}\Phi(\vec{r}', t') \tag{2.48}$$

2.3.2 Solution by Green's Function Method

Fluence from equation (2.48) at wavelength λ at position $\vec{r}'$ and time instant t' is obtained as a solution to equation (2.46). Let us assume Dirac delta excitation for $q(\vec{r}, t) = \delta^3(\vec{r} - \vec{r}_s)\delta(t)$. Then the solution of (2.46) for fluence $\Phi(\vec{r}, t)$ will be Green's function $G(\vec{r}_s, \vec{r}, t)$. Here we explicitly write $\vec{r}_s$ as variable of the function G, since we want to emphasize it is the solution when the source is point-like and isotropic, positioned at $\vec{r}_s$. Then we can write

$$q_e(\vec{r}', t') = \mu_{sR}G(\vec{r}_s, \vec{r}', t'). \tag{2.49}$$

On the other hand, according to the Green's function method (see Section 2.2.4) solution for the fluence at λ_e is obtained from the following integral

$$\Phi_e(\vec{r}, t) = \int_0^t \int_{V'} q_e(\vec{r}', t')G_e(\vec{r}', \vec{r}, t - t')\mathrm{d}\vec{r}'^3\mathrm{d}t', \tag{2.50}$$

where G_e is the Green's function obtained as solution to the equation (2.47) when source is Dirac delta, basically the same as G, but with different optical parameters. Finally, Raman fluence (fluence at the wavelength of Raman emission λ_e) is given by

$$\Phi_e(\vec{r}, t) = \mu_{sR} \int_0^t \int_{V'} G(\vec{r}_s, \vec{r}', t')G_e(\vec{r}', \vec{r}, t - t')\mathrm{d}\vec{r}'^3\mathrm{d}t'. \tag{2.51}$$

2.3.3 Heuristic Approach

Here we will derive a very simple equation that connects the Raman fluence at λ_e with the fluence at λ. Of course, the following reasoning is valid only in special cases, but the result may be applied also in practice where not all the conditions are strictly fulfilled.

First of all, we consider a case where optical parameters of the so far considered homogeneous medium are the same at wavelengths λ and λ_e: $\mu_{ab} = \mu_{abe}$, $\mu'_{sb} = \mu'_{sbe}$,

$v = v_e$. We also assume the scattering phase function to be the same on both wavelengths of interest.

Secondly, we know that $\mu_{ae} = \mu_{abe}$, $\mu'_{se} = \mu'_{sbe}$. Therefore, the following relation is obvious:

$$\Phi_e(\vec{r}, t, \mu_{ae}, \mu_{se}) = \Phi_e(\vec{r}, t, \mu_{ab}, \mu'_{sb}), \tag{2.52}$$

where the left-hand side refers to the fluence of Raman photons (at wavelength λ_e) in real medium as it is, while the right-hand side would be the fluence at wavelength λ_e in the background medium, when equality relation exists between optical parameters and functions at two considered wavelengths λ and λ_e.

Now we recall the scaling property for absorption, explained in 2.2.5. Knowing that $\mu_a = \mu_{ab} + \mu_{sR}$ and $\mu'_s = \mu'_{sb}$, we can write

$$\Phi(\vec{r}, t, \mu_a, \mu'_s) = \Phi(\vec{r}, t, \mu_{ab}, \mu'_{sb}) \exp\left(-\mu_{sR} v t\right) \tag{2.53}$$

for the fluence at wavelength λ. The left-hand side of the equation is the fluence as it is, in real medium. The right-hand side consists of two factors, the second one is due to the scaling of absorption, while the first one represents the fluence in case of the background medium, where there are no Raman scattering events.

The fluence of Raman photons can be expressed as the difference between the fluence of all photons (at both wavelengths λ and λ_e) and the fluence of those photons that did not undergo Raman scattering event [39]:

$$\Phi_e(\vec{r}, t, \mu_{ab}, \mu'_{sb}) = \Phi(\vec{r}, t, \mu_{ab}, \mu'_{sb}) - \Phi(\vec{r}, t, \mu_{ab}, \mu'_{sb}) e^{-\mu_{sR} v t}. \tag{2.54}$$

In reality, absorption coefficient is $\mu_a = \mu_{ab} + \mu_{sR}$. However, if we consider absorption only due to background μ_{ab}, then also the Raman scattered photons at λ_e will be accounted in the fluence $\Phi(\vec{r}, t, \mu_{ab}, \mu'_{sb})$. Why can we state this? If the optical parameters at λ and λ_e are the same, including the scattering phase function, then, once a Raman scattering occurs, in theory the wavelength of the photon changes from λ to λ_e, but in practice, it is not seen in its propagation. The photon propagation continues in the same way as it would have continued if the photon had experienced a Tyndall instead of Raman scattering. Moreover, in Raman scattering event absorption (removal) of photon at λ is not taken into account by keeping background value of absorption coefficient μ_{ab} instead of using $\mu_{ab} + \mu_{sR}$. Therefore, fluence $\Phi(\vec{r}, t, \mu_{ab}, \mu'_{sb})$ accounts for both wavelengths λ and λ_e. The second term on the right-hand side of the equation (2.54) clearly represents the number of photons that in the real medium, according to (2.53), avoided Raman scatterings.

Finally, combining (2.52) and (2.54), Raman fluence becomes

$$\Phi_e(\vec{r}, t, \mu_{ae}, \mu'_{se}) = \Phi(\vec{r}, t, \mu_{ab}, \mu'_{sb}) \left(1 - e^{-\mu_{sR} v t}\right). \tag{2.55}$$

Since values for Raman scattering coefficient are usually very small (of the order of $10^{-6}\,\mathrm{mm}^{-1}$), the last equation can be simplified, by approximating the right-hand side's exponential function with the first order Maclaurin polynomial:

$$\Phi_e(\vec{r}, t, \mu_{ae}, \mu'_{se}) \approx \Phi(\vec{r}, t, \mu_{ab}, \mu'_{sb})\mu_{sR} v t. \tag{2.56}$$

Important conclusion from this equation is that, once the Green's function of the problem imposed only for the background medium is known, it can be directly transformed to the Green's function of the Raman signal. Morever, from equation (2.56) we can see how the temporal curve of detected number of photons would change if the detection was switched from wavelength λ to λ_e, and it will be shown in the next section[2], in Figure 2.5. Another obvious observation, justified also by this equation: the longer the photons travel through the medium, the higher the probability for them to be Raman scattered.

In the very end of this section, we would like to recap the key assumptions of this heuristic approach. That will serve as a reminder before we move to the two-layer media case, since we must be conscious under which conditions the model is appropriate, or under which it may produce significant errors. Analysis on the range of validity for the homogeneous case was reported in the paper of Martelli et al. [39]. Similar analysis, on a two-layer media case can be performed by comparing the results (from Section 2.4 or Chapter 3) with the "gold standard" Monte Carlo simulations, but it is beyond the scope of this thesis work. As a message for the next sections, we should bear in mind that the key assumption is: optical parameters at the source emission wavelength λ and the Raman emission wavelength λ_e are identical. In practice, this is never fulfilled. However, we expect to have some range where the results could be treated as reliable, depending on the slopes of the functions representing the optical parameter (absorption, scattering, refractive index) as a function of wavelength, in the intervals of interest.

2.3.4 Plots of the Solutions

In this section we present plots obtained by applying the heuristic model for Raman reflectance calculation, still in the case of a homogeneous medium.

The first plot, represented in Figure 2.5, shows the relation between reflectance detected at λ and Raman reflectance at λ_e. Clearly, the peak of Raman reflectance arrives later and the curve rises and drops slower. This is because of the multiplication by t factor in the heuristic model.

Let us now see how the optical parameters, namely absorption and scattering coefficient affect the Raman reflectance obtained by the heuristic model. In Figure

[2]Of course, the key condition $\mu_{ab} = \mu_{ae}$ must be met, otherwise this is just a rough estimation and only intuitive shortcut to estimate the temporal profile, but not the exact law.

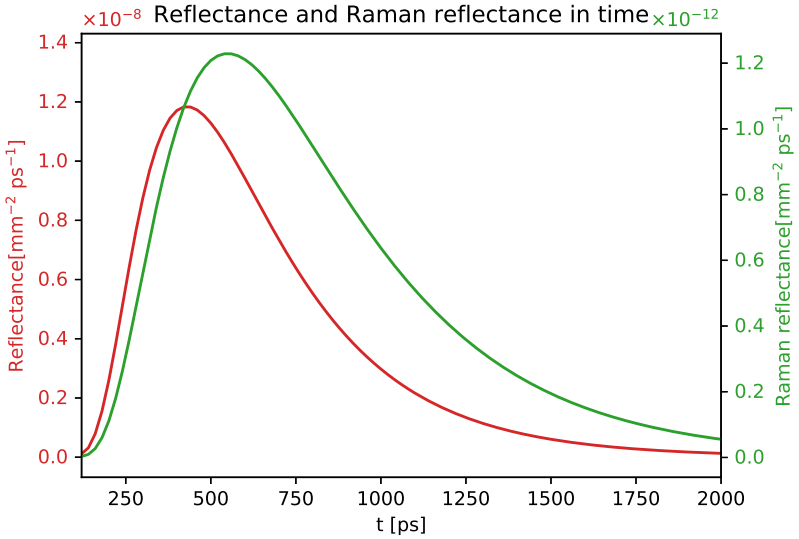

Figure 2.5: Temporal profile of reflectance (red) and Raman reflectance (green). Optical parameters were: $\mu_{ab} = 0.01\,\mathrm{mm}^{-1}$, $\mu'_{sb} = 1\,\mathrm{mm}^{-1}$. Raman scattering coefficient was $\mu_{sR} = 10^{-6}\,\mathrm{mm}^{-1}$. Different scales for the two curves were chosen in order to better show the effects of multiplying by t. Index of refraction was $n = 1.4$. Distance between the source and the detector was $\rho = 20\,\mathrm{mm}$.

2.6 temporal profile of Raman reflectance is shown for different coefficients of absorption. It is evident that for higher absorptions, maximum of the signal is lower and comes earlier in time. Besides that, Raman signal drops more quickly, therefore we can conclude that majority of Raman photons tend to finish their propagation earlier for higher absorptions.

In Figure 2.7 temporal profile of Raman reflectance is shown for different reduced scattering coefficients. It can be noticed that maximum of the signal arrives later and is lower as the scattering coefficient increases. This suggests that for higher scattering coefficients, photons tend to find even more complicated paths, requiring more time to reach the detector. Statistically, due to greater exposure to absorption, the signal becomes weaker for higher scatterings.

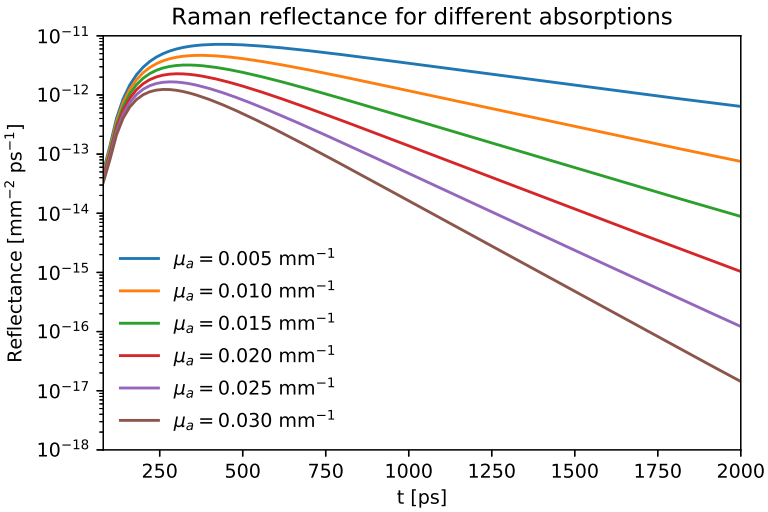

Figure 2.6: Raman reflectance over time in logarithmic scale. Six different curves correspond to six equidistant absorptions $\mu_{ab} \in [0.005; 0.030]$ mm^{-1}. Reduced scattering coefficient was kept constant $\mu'_{sb} = 1\,\text{mm}^{-1}$ as well as Raman scattering coefficient $\mu_{sR} = 10^{-6}\,\text{mm}^{-1}$. Distance between the source and the detector was $\rho = 15\,\text{mm}$. Index of refraction was set to $n = 1.4$.

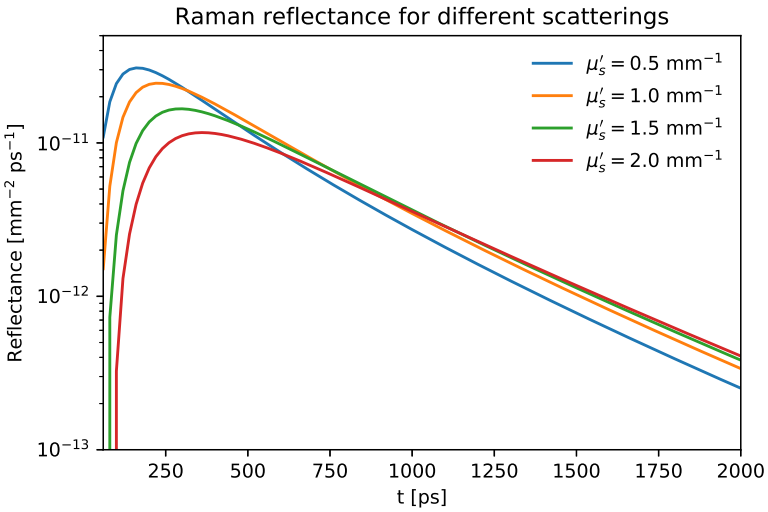

Figure 2.7: Raman reflectance over time in logarithmic scale. Four different curves correspond to four equidistant scatterings $\mu'_{sb} \in [0.5; 2.0]$ mm^{-1}. Absorption coefficient was kept constant $\mu_{ab} = 0.007\,\text{mm}^{-1}$ as well as Raman scattering coefficient $\mu_{sR} = 10^{-6}\,\text{mm}^{-1}$. Distance between the source and the detector was $\rho = 10\,\text{mm}$. Index of refraction was set to $n = 1.4$.

2.4 Heuristic Approach to Two-Layer Diffuse Raman

The concept of a heuristic approach exposed in the previous section for the special case of Raman scattering in homogeneous media can be generalized. The aim of the Section 2.3 was to present the reasoning, modelling, justification for some formulas, and finally, give a review of the performances and limitations of the model. The statement by Martelli et al. in their paper from 2016 [39] about the applicability of the heuristic model described by the equation (2.56) only for homogeneous media, strictly speaking, is true. However, that model contains enough road signs to motivate its generalization to non-homogeneous media, particularly two-layer media.

2.4.1 Generalization from Homogeneous to Two-Layer Media

Since the solution of photon diffusion problems is already found in theory [1] for the case of two-layer media, and the equation (2.56) connects the Raman fluence with the fluence at the wavelength of the source in a very simple way, it is reasonable to think that this equation can be generalized in such a way to keep its simplicity while accounting for the phenomena that take place in two-layer media. That is what Prof. Martelli was working on recently [40]. His assumption was that the general model for the two layers, analogously to the homogeneous case can be expressed as

$$\Phi_e(\vec{r}, t, \mu_{a1e}, \mu'_{s1e}, \mu_{a2e}, \mu'_{s2e}) \approx \Phi(\vec{r}, t, \mu_{a1b}, \mu'_{s1b}, \mu_{a2b}, \mu'_{s2b}) \cdot [\mu_{sR1} v_1 \langle t_1 \rangle + \mu_{sR2} v_2 \langle t_2 \rangle] \tag{2.57}$$

where:

- $\Phi_e(\vec{r}, t, \mu_{a1e}, \mu'_{s1e}, \mu_{a2e}, \mu'_{s2e})$ is the fluence of the photons at wavelength λ_e, i.e. Raman photons, at position $\vec{r}$ and time t;
- $\Phi(\vec{r}, t, \mu_{a1b}, \mu'_{s1b}, \mu_{a2b}, \mu'_{s2b})$ is the fluence of the photons at source emission wavelength λ, at position $\vec{r}$ and time t;
- optical properties for the first (upper) layer: absorption at λ: μ_{a1b}, absorption at λ_e: μ_{a1e}, reduced scattering at λ: μ'_{s1b}, reduced scattering at λ_e: μ_{s1e};
- and for the second (lower) layer: absorption at λ: μ_{a2b}, absorption at λ_e: μ_{a2e}, reduced scattering at λ: μ'_{s2b}, reduced scattering at λ_e: μ_{s2e};
- $\langle t_1 \rangle$ and $\langle t_2 \rangle$ are the mean times of flight in the first and second layer, respectively, calculated according to the formula (2.19).

The detailed explanation for the formula (2.19) is given in Section 2.2.5. Note that the equation (2.19) holds in the general case of Transport Theory. Here we will provide analytical expressions for the estimation of average time of flights for the two layers in case of two-layer media:

$$\langle t_1 \rangle = -\frac{1}{v_1 \Phi(\vec{r}, t, \mu_{a1b}, \mu'_{s1b}, \mu_{a2b}, \mu'_{s2b})} \frac{\partial \Phi(\vec{r}, t, \mu_{a1b}, \mu'_{s1b}, \mu_{a2b}, \mu'_{s2b})}{\partial \mu_{a1b}} \tag{2.58}$$

and

$$\langle t_2 \rangle = -\frac{1}{v_2 \Phi(\vec{r}, t, \mu_{a1b}, \mu'_{s1b}, \mu_{a2b}, \mu'_{s2b})} \frac{\partial \Phi(\vec{r}, t, \mu_{a1b}, \mu'_{s1b}, \mu_{a2b}, \mu'_{s2b})}{\partial \mu_{a2b}}. \tag{2.59}$$

Instead of fluence, reflectance can also be used in the same way.

2.4.2 Application of the Model

If we have a two-layer medium, we are able to calculate the mean time of flight in the upper layer $\langle t_1 \rangle$ and in the lower layer $\langle t_2 \rangle$, according to (2.58) and (2.59). If we represent graphically the time dependence of $\langle t_1 \rangle(t)$ and $\langle t_2 \rangle(t)$ in Figure 2.8, as well as their sum, we notice that the results are in accordance to what we expected.

Let us see in practice the differences between the signal arriving from two different layers. Figure 2.9 shows the Raman reflectance temporal profiles obtained by applying the model for two cases. The first one is the top layer signal case, where Raman scattering coefficient of the bottom layer was set to zero, thus accounting only Raman scattered photons from the top layer. The second one is obtained conversely, by setting the Raman scattering coefficient of the first layer to 0. Non-zero Raman scatterings had same values, for simplicity and easier comparison. We can note that after a certain time, in this case around 2.5 ns, signal from bottom layer becomes stronger than the signal from the top layer. Maximum of the top layer signal is greater than the maximum of the bottom layer signal, and arrives much earlier in time than the other one, which is completely in accordance with the theory exposed.

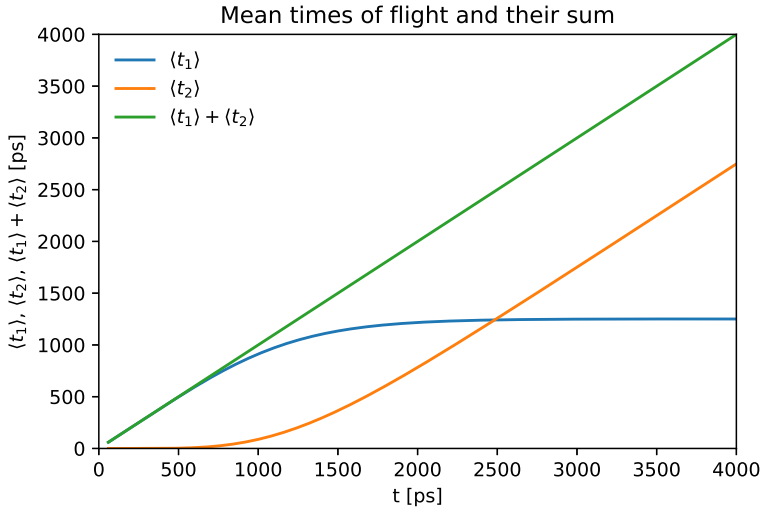

Figure 2.8: Mean times of flight and their sum. Two curves (blue and orange) represent average time that photon spends in two layers, and the third (green) one, which is basically straight, represents its sum. For the computation, thickness of the first layer was $d_1 = 10\,\mathrm{mm}$, of the second layer $d_2 = 60\,\mathrm{mm}$, distance between the source and detector was $\rho = 10\,\mathrm{mm}$. $\mu_{a1} = 0.011\,\mathrm{mm}^{-1}$, $\mu_{a2} = 0.003\,\mathrm{mm}^{-1}$, $\mu'_{s1} = 1.65\,\mathrm{mm}^{-1}$, $\mu'_{s2} = 1.5\,\mathrm{mm}^{-1}$.

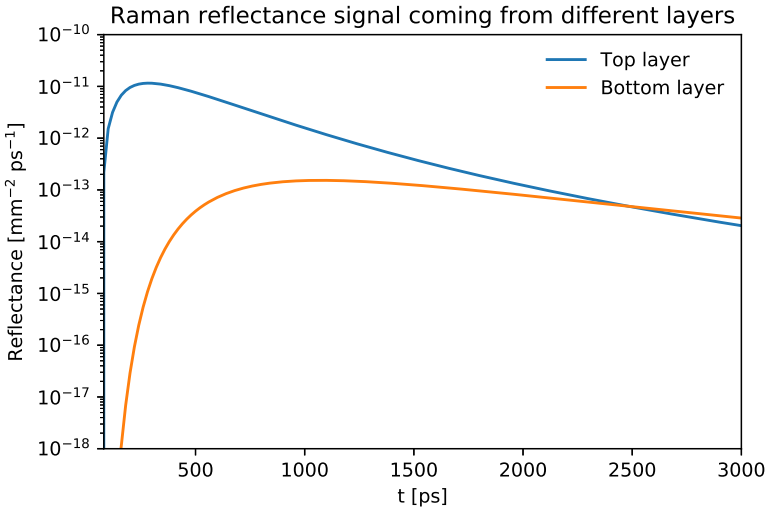

Figure 2.9: Raman reflectance over time in logarithmic scale. Two curves represent Raman signals from two layers. Parameters used for the computation were the same as for the Figure 2.8. Additionally, when different from zero, $\mu_{sR} = 10^{-6}\,\mathrm{mm}^{-1}$.

2.5 Inverse Problem

With the theory exposed so far, we can now think about the reconstruction of spectra of the two layers, when Raman reflectance measurements are provided. We must note that real measurements will be affected by noise and fluorescence, then by the measurement system itself both in temporal and in spectral domain. These are the factors that could make the reconstruction, i.e. retrieval of the Raman scattering coefficients at different wavelengths (Raman spectrum), when measurements (Raman reflectances) are known, difficult or less successful. Reconstruction process is not predefined, various strategies may be followed. What is for sure, reconstruction methods have to be developed to take into account all undesirable effects in such a way to minimize their impact on the reconstruction results. First step towards reconstruction is the formulation of the inverse problem.

2.5.1 Formulation

We are considering the same two-layer geometry, as defined in the previous section. Let us assume we have measurement results, in form of Raman reflectance at different wavelengths and times, $R_e(\lambda, t)$. Wavelengths are defined by the spectrometer of the system and times are defined by the choice of time gating. In principle, available times could be all times for which the system acquired data, but in practice, they are reduced to a set of time gates. Time-gating of photons (or reflectance signal) is the integration over time of the number of photons being collected by the detector per unit time. The total number of photons that fall on the detector during the gating interval (t_{start}, t_{end}) is called "gated signal" or "gated measurement". Time gating could be performed either directly with hardware during the measurement process, or in software during post-processing, as mentioned already in Section 1.4.

According to the equation for the Raman reflectance detected at some wavelength λ and time t, by the detector positioned on the surface of the two-layer medium

$$R_e(\lambda, t) = R(t) \times \left[\mu_{sR1}(\lambda) v_1 \langle t_1 \rangle + \mu_{sR2}(\lambda) v_2 \langle t_2 \rangle\right], \tag{2.60}$$

which follows from (2.57), knowing the reflectance at the source emission wavelength at time t, $R(t)$, and with calculation of average pathlengths $v_1\langle t_1\rangle$ and $v_2\langle t_2\rangle$ according to (2.58) and (2.59), it is possible to retrieve the Raman spectra for upper $\mu_{sR1}(\lambda)$ and lower $\mu_{sR2}(\lambda)$ layer of the medium. Note that the equation (2.60) is linear for $\mu_{sR1}(\lambda)$ and $\mu_{sR2}(\lambda)$. Therefore, we may formulate the inverse problem in the following way. Having the measurements $R_e(\lambda, t)$ and weights $w_1(\lambda, t)$ and $w_2(\lambda, t)$, the goal is to obtain $\mu_{sR1}(\lambda)$ and $\mu_{sR2}(\lambda)$ from the set of equations of form:

$$R_e(\lambda, t) = w_1(\lambda, t)\mu_{sR1}(\lambda) + w_2(\lambda, t)\mu_{sR2}(\lambda). \tag{2.61}$$

It is worth noting that here weights are expressed as functions of both, time and wavelength. This is done in order to cover more general case, even though the theoretical model and equation (2.60) do not predict the dependence of weights on wavelengths, due to the heuristic approximation. In fact, optical parameters that are found in equations of the theoretical model, as it is the case with absorption and scattering, are dependent on wavelength. Therefore, strictly speaking, weights should be functions of both, wavelength and time.

If the number of time gates is N_g, then the system of equations of form (2.61) will consist of N_g equations with 2 unknowns, for each wavelength. If the number of wavelengths is N_w, then the inverse problem will consist of finding solutions to N_w systems, each of N_g equations with 2 unknowns. For each wavelength λ_i, $i \in \{1, 2, 3, \ldots, N_w\}$, the system to be solved can be written as:

$$\begin{aligned} R_e(\lambda_i, t_1) &= w_1(\lambda_i, t_1)\mu_{sR1}(\lambda_i) + w_2(\lambda_i, t_1)\mu_{sR2}(\lambda_i) \\ R_e(\lambda_i, t_2) &= w_1(\lambda_i, t_2)\mu_{sR1}(\lambda_i) + w_2(\lambda_i, t_2)\mu_{sR2}(\lambda_i) \\ &\vdots \\ R_e(\lambda_i, t_{N_g}) &= w_1(\lambda_i, t_{N_g})\mu_{sR1}(\lambda_i) + w_2(\lambda_i, t_{N_g})\mu_{sR2}(\lambda_i) \end{aligned} \tag{2.62}$$

or more compactly in matrix form:

$$\mathbf{R_e}(\lambda_i) = \mathbf{W}(\lambda_i) \cdot \mathbf{S}(\lambda_i) \tag{2.63}$$

where

- $\mathbf{R_e}_{N_g \times 1}(\lambda_i)$ is the measurements column vector;
- $\mathbf{W}_{N_g \times 2}(\lambda_i)$ is the sensitivity matrix whose first column is filled with weights $w_1(\lambda_i, t_j)$ for $j = 1, 2, \ldots, N_g$ and the second column is filled with weights $w_2(\lambda_i, t_j)$ for $j = 1, 2, \ldots, N_g$;
- $\mathbf{S}_{2\times 1}(\lambda_i) = \begin{bmatrix} \mu_{sR1}(\lambda_i) & \mu_{sR2}(\lambda_i) \end{bmatrix}^{\mathrm{T}}$ is the spectrum to be reconstructed.

To solve this problem, one would need at least 2 equations for each λ_i. In practice, number of gates N_g can greater than 2. From now on, we will assume $N_g > 2$, so we have an overdetermined system.

2.5.2 Least Square Solution

The system to be solved is linear and overdetermined. To simplify notation, here we skip explicit writing of dependence on wavelength λ, but always keep in mind that the system to be solved is defined for a specific λ. There are many possible solutions for the spectrum $\mathbf{S}$, but none of them will be exact, since the 2 parameters

μ_{sR1} and μ_{sR2} have only 2 degrees of freedom and in general case it is not possible to simultaneously satisfy $N_g > 2$ equations. Therefore, we should look for the solution which is the closest to the obtained measurements, i.e. some measure of discrepancy between $\mathbf{R_e}$ and $\mathbf{WS}$ should be minimized. The solution for this type of problems is found by applying so-called least square linear fit. In other words, we will look for the least square solution of the problem [46]. In this approach, sum of "distances" (squared differences) between the obtained measurements and fit of the solution is minimal among all possible solutions.

Formally, the vector $\mathbf{S}^*$ is the least square solution of the problem if

$$\|\mathbf{WS}^* - \mathbf{R_e}\|_2 = \min_{\mathbf{S}\in\mathbb{R}^2} \|\mathbf{WS} - \mathbf{R_e}\|_2, \tag{2.64}$$

where $\|\mathbf{x}\|_2 = \sqrt{\sum_{i=0}^{n} x_i^2}$ is the Euclidean norm for vector $\mathbf{x} = (x_1, x_2, \ldots, x_n)$.

Let us consider a multivariable function $f(\mathbf{S}) = \frac{1}{2}\|\mathbf{WS} - \mathbf{R_e}\|_2^2$. By expanding we obtain

$$f(\mathbf{S}) = \frac{1}{2}\left(\mathbf{WS} - \mathbf{R_e}\right)^{\mathrm{T}}\left(\mathbf{WS} - \mathbf{R_e}\right) = \frac{1}{2}\mathbf{S}^{\mathrm{T}}\mathbf{W}^{\mathrm{T}}\mathbf{WS} - \mathbf{S}^{\mathrm{T}}\mathbf{W}^{\mathrm{T}}\mathbf{R_e} + \frac{1}{2}\mathbf{R_e}^{\mathrm{T}}\mathbf{R_e}. \tag{2.65}$$

If $\nabla f(\mathbf{S}) = 0$, then $\mathbf{S}$ is a stationary point, a candidate for local extreme. It will be minimum and also global in this case, since the function is quadratic. Therefore, the least square solution $\mathbf{S}^*$ satisfies the condition

$$\nabla f(\mathbf{S}^*) = 0. \tag{2.66}$$

Since

$$\nabla f(\mathbf{S}) = \mathbf{W}^{\mathrm{T}}\mathbf{WS} - \mathbf{W}^{\mathrm{T}}\mathbf{R_e}, \tag{2.67}$$

the normal equations to be solved are

$$\mathbf{W}^{\mathrm{T}}\mathbf{WS}^* = \mathbf{W}^{\mathrm{T}}\mathbf{R_e}. \tag{2.68}$$

Here we highlight the term "normal equations", since this system is now square, $\mathbf{W}^{\mathrm{T}}\mathbf{W}$ is a 2×2 matrix in case of 2-layer media. Retrieval of $\mathbf{S}^*$ is now very simple. However, this has to be done on all wavelengths λ_i, $i = 1,2,\ldots,N_w$. In case $\mathbf{W}(\lambda_\mathbf{i})$ actually depends on λ_i also in the model, much more computational effort is spent on calculating sensitivity matrices for different wavelengths. About the computational realization, we will talk in the following section.

2.6 Software Implementation

In order to turn ideas and equations into practice, it was required to develop a computer program, which will perform all the necessary computations regarding the forward model and the reconstruction.

2.6.1 Development of The Program

Starting point of the development of a new program able to simulate Raman reflectance signal for the two-layer media was the C language code which I received from Prof. Martelli. That code was written back in year 2003, and contained methods to calculate reflectance (as well as transmittance, but it is not of interest here) in the two-layer cylindrical and bounded media. Reflectance could be calculated at different points of the time domain, when the excitation is unitary Dirac delta on top of the first layer. Source-detector separation, as well as thicknesses of the layers and optical parameters could be specified. The methods that had been written present numerical implementation of the solution of the Diffusion Equation for bounded media, with boundary conditions at the interface between the two layers and at the interfaces between the top layer and the environment, as well as the bottom layer and the environment.

To move from this point towards the two-layer Diffuse Raman, I had to exploit the equation (2.57). Note that mean times of flight are calculated performing the partial derivative in theory (recall the equations (2.58) and (2.59)). However, here it had to be a numerical derivation, where the forward model calculations of reflectance were performed for two cases: for the actual absorption coefficient and for its incremented value, with a relative increment of 10^{-4}. Note that we use reflectance now, but as stated in Section 2.4.1, equations for mean times of flight (2.58) and (2.59), are also applicable when we substitute fluence with the reflectance.

By adding two new optical parameters, Raman scattering coefficients of both layers, C program became complete to simulate Raman reflectance response in time domain, at a certain Raman emission wavelength. However, this was not enough in practice. We know that Raman spectrum is extremely chemically specific and it would make no sense if we operate only with one wavelength, or in other words, if we are blind for wavelengths. Moreover, simulations that were to be performed would require Poisson statistics, then, reconstruction would need operation with matrices and numerical methods for solving systems of equations, and finally, graphical representation of the results on the spot was highly desirable. All of that was pointless to implement in C in the development phase. Therefore, the decision was to move to the Python language, adapt the methods from C code, and enable further generalization with the implementation of classes for Spectrum, Signal, System, Forward Model, Inversion, and many others including the ones replacing the old data structures from C.

2.6.2 Exact Forward Model

In the previous sections (2.4), setup of the two-layer medium was implicitly assumed. The geometry could have been any, with the two layers one on top of the other.

However, since we are now dealing with the specific software, precise formulation of the geometry and optical properties is needed.

We assume to have a medium composed of two layers. Thickness of the first layer is d_1, and of the second d_2. We may assume a cylindrical geometry of the medium, but if we also impose constraint that lateral dimensions are big enough to practically appear as unbounded medium for photons propagating in lateral direction (due to absorption phenomenon, this can be met), then this assumption is not crucial.[3] A light source is on the surface of the top layer, as well as the detector, separated by some distance ρ. For easier visualisation, geometry of the system is shown in Figure 2.10.

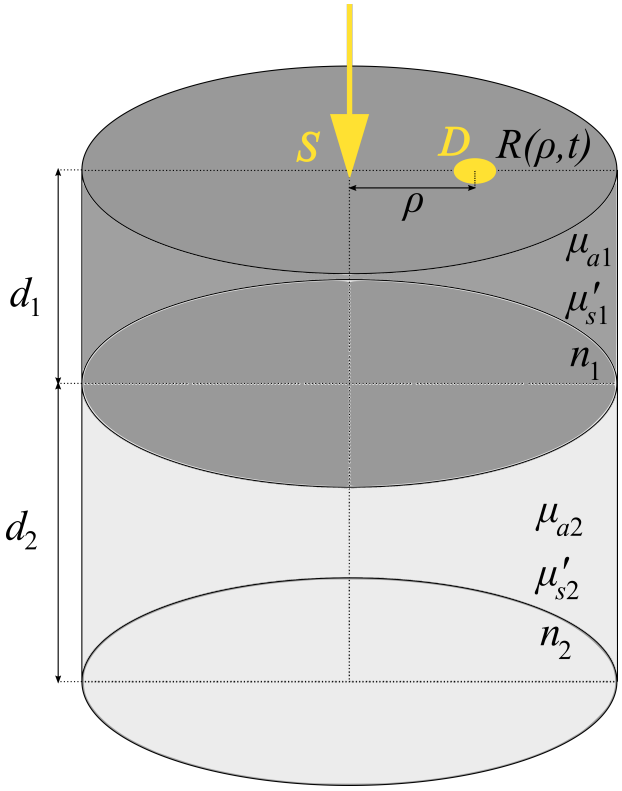

Figure 2.10: Two-layer medium in a cylindrical geometry. The laser source (S) and the detector (D) are marked with yellow colour. Reflectance $R(\rho, t)$ is measured by the detector.

Additionally, we assume that both the layers are homogeneous, i.e. characterized

[3]Anyway, all geometrical parameters, including this one (the lateral dimension), are specified in an input file, or inside the program, when defining the forward model. That is how we can choose either practically unbounded medium or strictly bounded.

by optical parameters independent of the position. For the first, or upper layer, absorption coefficient is μ_{a1}, reduced scattering coefficient is μ'_{s1}, refraction index n_1, light propagation speed $v_1 = c/n_1$. For the second, or lower layer, the parameters are denoted analogously: μ_{a2}, μ'_{s2}, n_2 and $v_2 = c/n_2$. Note that the optical parameters, already independent on coordinate, here are defined as independent of wavelength as well.[4] This will be the assumption for the whole Chapter 3. Only in Chapter 4 we will consider also this variability which appears in reality.

Finally, we have to consider the Raman spectra of the two layers. We assume that the Raman spectrum of the first layer is $\mu_{sR1}(\lambda)$, and of the second $\mu_{sR2}(\lambda)$, where $\mu_{sR1}(\lambda)$ is the Raman scattering coefficient characteristic for the upper layer medium, for the Raman emission wavelength λ, and $\mu_{sR2}(\lambda)$ is the Raman scattering coeffcient of the lower layer medium, for the same Raman emission wavelength.

The Raman reflectance is expressed from the equation (2.57) (where the fluence is substituted by the reflectance). To calculate the value, the reflectance at the source emission wavelength has to be calculated for the two-layer cylindrical geometry. Equations are given in [1], while that part of the software had been already developed before the Raman modification, as stated in 2.6.1.

2.6.3 Architecture and Data Flow

Architecture of the program with flow of data (inputs and outputs from program blocks) is presented in Figure 2.11. Optical and geometrical parameters are provided to the Diffuse Optics Forward Model block. This block produces the following outputs: sensitivity matrix $\mathbf{W}$, reflectance vector $\mathbf{R}$, average times of flight $\langle t_1 \rangle$ and $\langle t_2 \rangle$. Then, in Heuristic correction block, input data in form of Raman spectra $\mu_{sR1}(\lambda)$ and $\mu_{sR2}(\lambda)$ is added to the data obtained from the Diffuse Optics Forward Model to calculate Raman reflectance $\mathbf{R_e}(\lambda)$. Then, such obtained signal is passed to the Instrument block, where filtering is performed (convolution with the impulse response function of the Instrument). Upon that, the filtered signal is gated in the Signal gating block, after which the Noise block simulates the Poisson noise and adds it to the input signal, producing the simulated measurements $\tilde{\mathbf{M}}$ in the output. Sensitivity matrix is gated in the Matrix gating block, producing the gated sensitivity matrix $\mathbf{W_g}$ at the output. In the Inversion block, inputs $\mathbf{W_g}$ and measurements $\mathbf{M}$ (real experimental data, Chapter 4) or $\tilde{\mathbf{M}}$ (simulated data, Chapter 3) are used to obtain the reconstructed spectra at the output $\hat{\mu}_{sR1}(\lambda)$ and $\hat{\mu}_{sR2}(\lambda)$. In the Figures of Merit (FOM) block, input reconstructed spectra $\hat{\mu}_{sR1}(\lambda)$ and $\hat{\mu}_{sR2}(\lambda)$ are compared with the theoretical spectra $\mu_{sR1}(\lambda)$ and $\mu_{sR2}(\lambda)$ thus

[4] Actually, the dependence on wavelength can also be included in the program, but in that case, it is not one single forward model, rather many of them, each defined for a specific wavelength. Then, forward problem calculations are performed on different forward models.

producing the Figures of Merit in the output. After the rejection of fluorescence from the real measurements spectra, finally reconstructed Raman spectra of the two layers are obtained at the output of the Background Removal block.

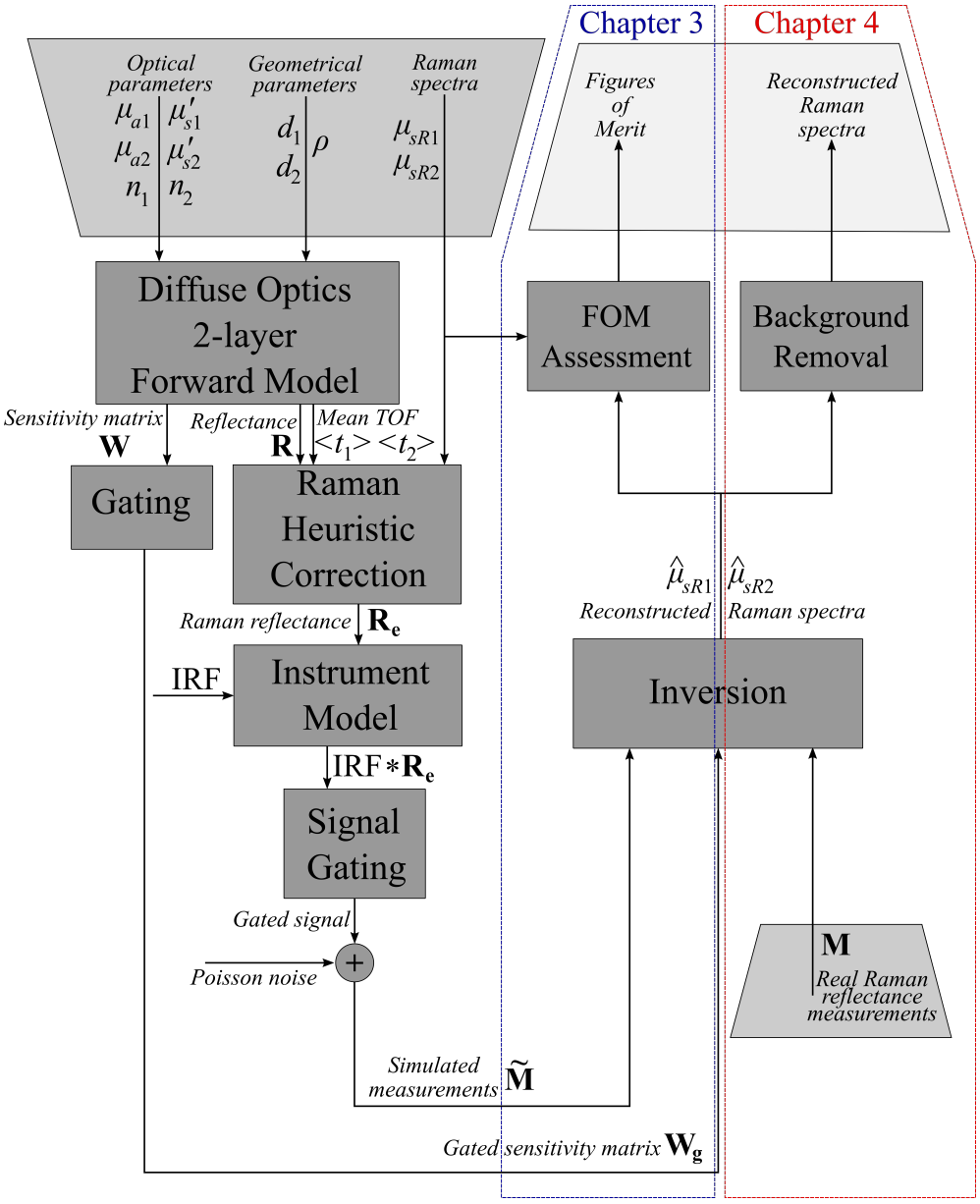

Figure 2.11: Program architecture and data flow. Main blocks are coloured with dark gray. Input and output blocks are coloured with lighter grays. Labels for signals (data) are near the corresponding arrows. The parts highlighted with blue and red are specific to the Chapter 3 and 4, respectively.

Chapter 3

Reconstruction on Simulations

In this chapter, we are presenting the scenarios for the computer simulations and the results obtained. The analysis of the impact of various parameters to the quality of reconstruction, which will be measured in a precisely defined way, will also be provided. We start with the formulation of the problem.

3.1 General Formulation of The Problem

Let us consider a two-layer medium, defined in Section 2.6.2. We want to retrieve the information from deep, in other words, from the bottom layer (see Figure 2.10). As argued in Chapter 1, Raman spectrum has excellent chemical specificity. The goal is to successfully reconstruct the Raman spectra of both layers, top and bottom, upper or lower, first and second, as these terms have been and will be used throughout this work.

Here, for the sake of simplicity and because of practical reasons when defining the figures of merit, we neglect the dependence of optical parameters (absorption coefficient, reduced scattering coefficient, refractive index) on wavelength. However, in simulations we may define whatever Raman spectra we want for the top and bottom layer.

The goal is, provided that the reflectance configuration measurements are obtained (simulated), to reconstruct the unknown spectra $\mu_{sR1}(\lambda)$ and $\mu_{sR2}(\lambda)$. We will rely on the theoretical model elaborated in Chapter 2, assuming all of the parameters: d_1, d_2, μ_{a1}, μ_{a2}, μ'_{s1}, μ'_{s2}, n_1, n_2 to be known.

The process of reconstructing the unknown spectra from the known measurements, applying the theoretical model, is actually the process of finding the solution to the inverse problem, well defined in Section 2.5. We will follow the method

described there. We have to be sure that there are more than two Raman reflectance measurements. Each measurement represents a time-gated reflectance signal. To recap, the time-gating is actually an integration over time of the number of photons being collected by the detector per unit time, i.e. the total number of photons that fall on the detector from the start time of the gate t_{start} to the end time of the gate t_{end}. The number of gates N_g should be greater than 2, since we have two unknown spectra. Usually, here N_g will be around 10 (10 or 12). Basically, if we have N_g time gates defined by their start and end times, N_g integrals of Raman reflectance will be calculated over the corresponding N_g time intervals[1].

One part of the story is a numerical mathematics part, where, due to the nature of the problem, we solve overdetermined linear system, according to the 2.5.2. The other part is a computational physics part, where in order to prepare everything for solving the inverse problem, it is required to solve the forward problem, i.e. calculate the sensitivity matrices using the computer program described in Section 2.6.

3.2 Noise and Instrument Response Function in Simulations

Here we present the key features of a real measurement that will be incorporated into the simulations. We identified the necessity of including the noise and instrument response function of the acquisition system into our simulations[2]. If these features of a real measurement had not been simulated, reconstructions would have been meaningless, since the inversion procedure would always return the ideally reconstructed spectra (precise to the order of machine epsilon, i.e. rounding error).

Therefore, to obtain meaningful simulations, note that we had to add the simulation of noise on the detection side, in form of Poisson noise, due to the discrete nature of single photon detection. A total number of C_t photons detected in all gates is assumed. Let the theoretical response to the Dirac delta pulse excitation results in C_1 photons detected in all gates aggregated, and c_i photons in gates $i = 1, 2, \ldots, N_g$. With information on C_t and C_1 we know for how long the source should repeat its very short light pulses as excitations to our two-layer medium. According to the Poisson statistics, a random variable with expected

[1]Strictly, the reflectance is expressed per unit area and unit time. To obtain the number of photons one would need to multiply by the area of the detector or cell, but it is not of relevance here.

[2]Note that this part is the specificity of the simulations and thus it is a feature of this chapter. In Chapter 4, where real experimental data will be considered, this part would be not only unnecessary, but also completely wrong to add.

value $c_i \cdot \frac{C_t}{C_1}$ is sampled for each gate i, to represent a simulated number of collected photons when quantum noise is taken into account.

The acquisition system (in short the "instrument"), never has an ideal Dirac delta impulse response in time domain. We assume a gaussian shape for the instrument impulse response function (IRF), described by the equation:

$$\mathrm{IRF}(t) = A \exp\left(-\frac{t^2 \cdot \ln 2}{(\mathrm{FWHM}/2)^2}\right), \tag{3.1}$$

which is centred around $t = 0$ and amplitude A satisfies:

$$\int_{-\infty}^{+\infty} \mathrm{IRF(t)d}t = 1. \tag{3.2}$$

Note that here FWHM is the full width at half maximum ($A/2$) of the gaussian IRF(t) curve. The lower the FWHM, the closer to Delta impulse IRF is. In Figure 3.1 an example of the IRF is presented.

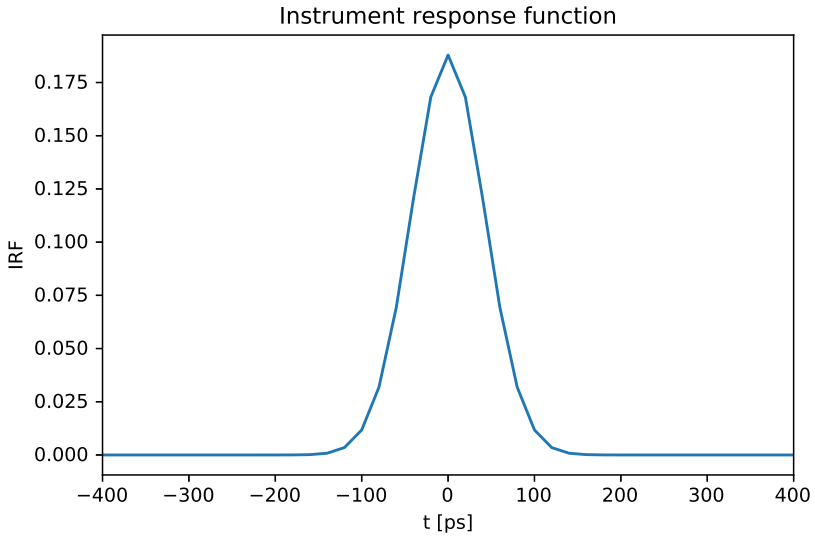

Figure 3.1: Instrument response function of the acquisition system. Steps at which IRF is calculated are 20 ps, because it is also the time step of the simulations done. FWHM = 100 ps.

3.3 A Few Examples of Simulations and Reconstructions

The aim of this section is to introduce the reader with the impact of noise and instrument response function on the quality of reconstruction. Therefore, a few characteristic scenarios will be presented.

Let us define our initial assumptions. For all simulations in this section, we assume gaussian Raman spectra for both layers, with maximum of $10^{-6}\,\mathrm{mm}^{-1}$ (this number is actually irrelevant, it can be arbitrary for the needs of simulations, but assumed like that to keep touch with reality). For the first (top) layer, centre of the gaussian curve is at λ_{m1}, corresponding to Raman shift $\Delta\overline{\nu}_{m1} = 1411\,\mathrm{cm}^{-1}$, and for the bottom layer the centre is positioned at λ_{m2}, corresponding to Raman shift $\Delta\overline{\nu}_{m2} = 1087\,\mathrm{cm}^{-1}$. Standard deviation of both curves is $20\,\mathrm{cm}^{-1}$, so they are well separated. The initial, theoretical, spectra are represented in Figure 3.2. For the

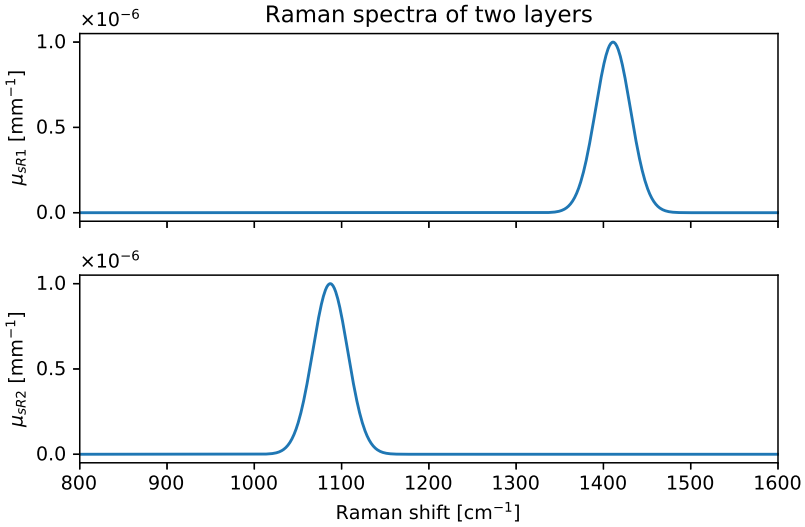

Figure 3.2: Theoretical Raman spectra of the first layer (top) and second layer (bottom).

following simulations, we have chosen the geometrical: $d_1 = 10\,\mathrm{mm}$, $d_2 = 60\,\mathrm{mm}$ (thick enough to appear unbounded), $\rho = 10\,\mathrm{mm}$, and optical parameters: $\mu_{a1} = 0.011\,\mathrm{mm}^{-1}$, $\mu_{a2} = 0.003\,\mathrm{mm}^{-1}$, $\mu'_{s1} = 1.65\,\mathrm{mm}^{-1}$, $\mu'_{s2} = 1.50\,\mathrm{mm}^{-1}$, $n_1 = n_2 = 1.4$.

Before starting with the reconstruction, it could be instructive to visualize the effect of noise on the temporal profile of the reflectance, or the number of photons detected. A simulated number of collected photons at two wavelengths λ_{m1} (top layer) and λ_{m2} (bottom layer) is presented in Figure 3.3. It might be difficult to understand how such noisy signal (particularly when considering signal level

from the bottom layer and its fluctuations) can be used to reconstruct the spectra. Moreover, the dynamic range of the top layer signal is around 3 decades, while for the bottom layer signal it is around 2. At the beginning (up to around 700 ps), the top layer signal is 2-3 orders of magnitude stronger than the bottom layer signal. Nevertheless, what we should bear in mind is that the time gating helps in diminishing the noise impact, and the least square method usually works well for linear problems if enough amount of data is provided. The top-to-bottom-layer-signal ratio decreases over time, and after around 2 ns the signals from the two layers become comparable, suggesting to select the time gates to extend at least up to that moment. In the following examples, we will see the reconstruction results, in terms of shapes of the obtained spectra, and discuss the effect of number of photon counts.

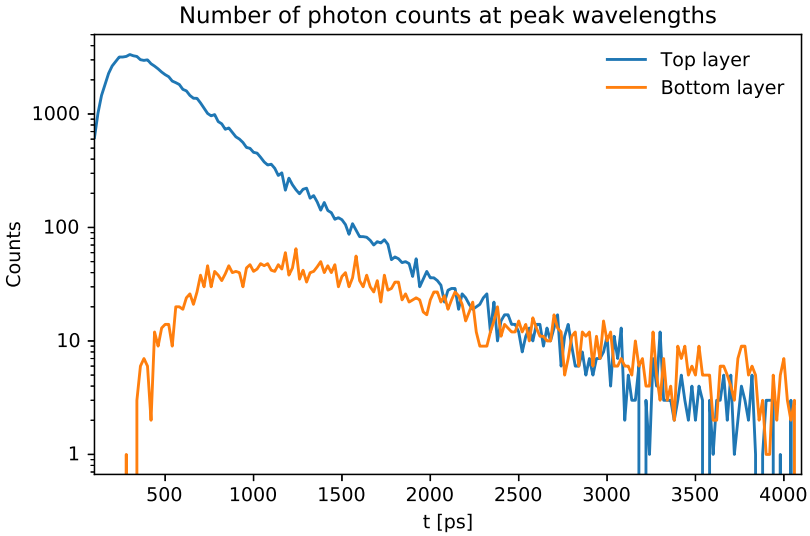

Figure 3.3: Time resolved number of photons detected at wavelengths characteristic to the Raman emission peaks of the two layers. Total number of photons collected at all wavelengths was assumed to be 10^6.

We start with a moderate scenario, where total photon counts of 10^6 is assumed and instrument response function with FWHM = 100 ps. The reconstructed spectra are shown in Figure 3.4. Clearly, the top layer is reconstructed without problems. On the other hand, reconstruction of the bottom layer, although with appropriate position of its inherent peak and height only slightly affected by noise, has problems at wavelengths around the peak of the top layer. The non-existing components in theoretical spectrum appeared here in reconstructed, due to the coupling between the layers. We will later show it is a consequence of noise, not the model.

First, we want to see the effect of instrument response function, so we change

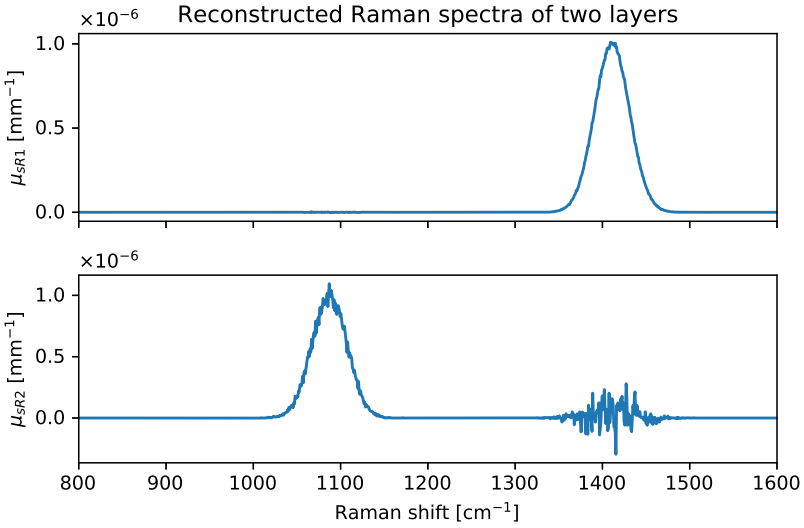

Figure 3.4: Reconstructed Raman spectra of the first layer (top) and second layer (bottom). Total photon counts was 10^6. IRF's FWHM was 100 ps.

its FWHM to 40 ps. The reconstructed spectra are shown in Figure 3.5. There is no meaningful difference in respect to the previous case (see Figure 3.4). Therefore, we may conclude that for FWHM $\leq$ 100 ps, IRF does not produce negative effects on the reconstruction.

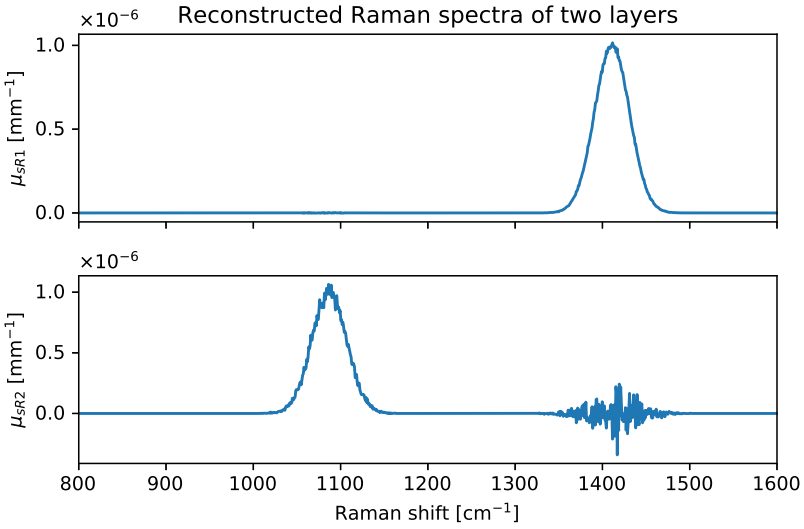

Figure 3.5: Reconstructed Raman spectra of the first layer (top) and second layer (bottom). Total photon counts was 10^6. IRF's FWHM was 40 ps.

Let us now consider a more optimistic case in terms of noise, where a total number of 10^7 photons is collected. The higher the number of photons detected, the lower the relative standard deviation, according to theory of Poisson distribution, signal-to-noise ratio is proportional to the square root of the number of photon counts. Therefore, we expect much better reconstruction of the bottom layer. The results are reported in Figure 3.6.

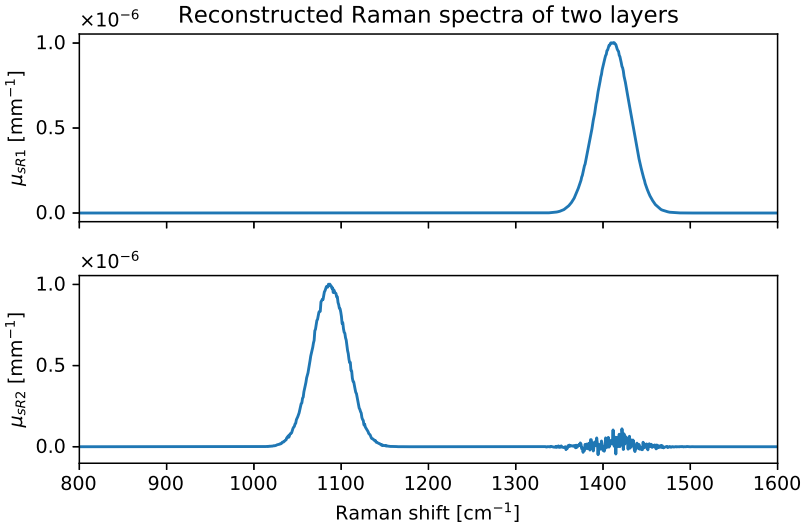

Figure 3.6: Reconstructed Raman spectra of the first layer (top) and second layer (bottom). Total photon counts was 10^7. IRF's FWHM was 100 ps.

If we go completely on the other side and assume very poor situation in terms of number of collected photons, 10^4, we expect to have bad results, as shown in Figure 3.7. We notice also that the top layer is affected by noise. The situation in the bottom layer now becomes suspicious. One may argue that the strong spectral components (including negative values which are nonphysical) at wavelengths characteristic to the top layer are to be expected and could be neglected. However, the region around the bottom layer inherent peak is contaminated by high amount of noise, as well, leading to a non-negligible error in reconstruction of the peak height.

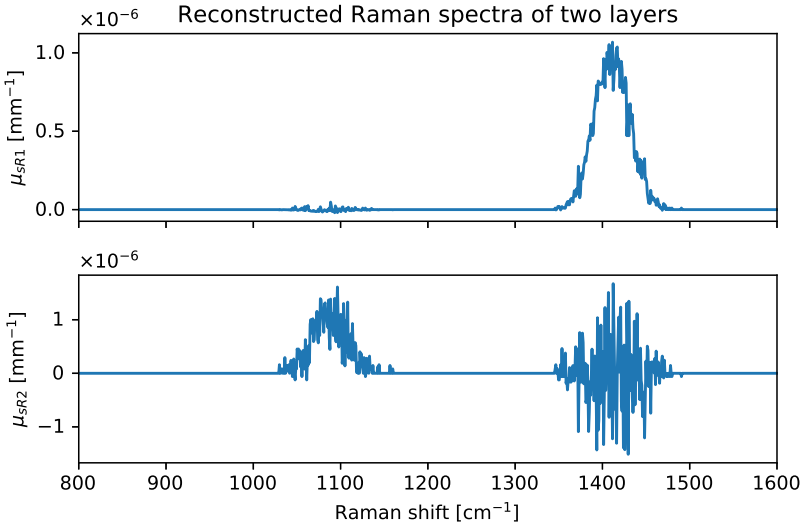

Figure 3.7: Reconstructed Raman spectra of the first layer (top) and second layer (bottom). Total photon counts was 10^4. IRF's FWHM was 100 ps.

Let us see what is the impact of the IRF when there is no noise. We assume relatively wide impulse response function of the instrument with FWHM = 200 ps. The results are shown in Figure 3.8. Obviously, the IRF has some impact on the coupling between the layers, which does not emerge from the theoretical physics model, rather is a consequence of convolution in temporal domain between the theoretically simulated signal and impulse response function of the acquisition system. We have said many times so far that the signal from top layer arrives first, and the information from bottom is expected later. However, if the system has such impulse response that early photons cause presence of signal also later in time, then it should not be unexpected to observe some components of the upper layer in the reconstructed spectrum of the lower layer.

To conclude this section, we would like to show what happens in an ideal case, when there is no noise, and when the IRF of the system is Dirac delta. Figure 3.9, representing the absolute error of the retrieved Raman scattering coefficients, shows that the spectra are faithfully reconstructed (notice the order of magnitude of the absolute error). Obviously, "noisy" parts are consequence of numerics, but they are so low that have to be neglected. The point is only that we should be conscious that errors can happen even in numerical mathematics part, when solving the inverse problem, despite a good theoretical model. However, values from Figure 3.9 demonstrate that these numerical errors are not meaningful at all.

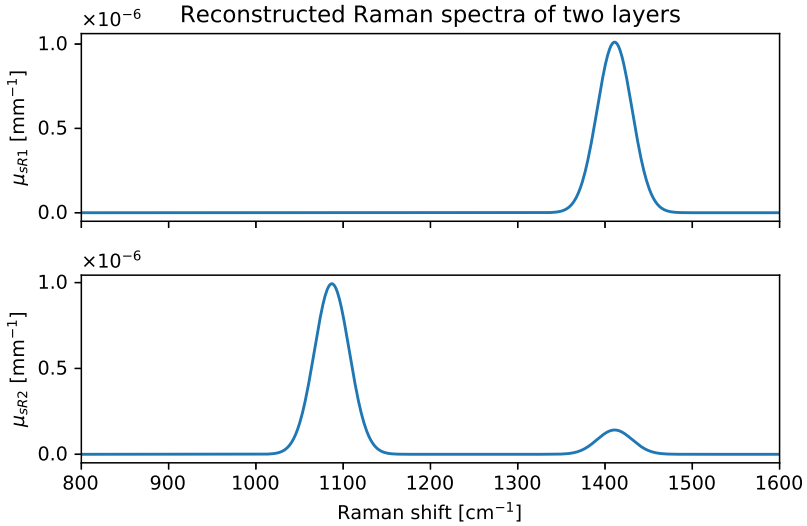

Figure 3.8: Reconstructed Raman spectra of the first layer (top) and second layer (bottom). IRF's FWHM was 200 ps. Noise was completely neglected.

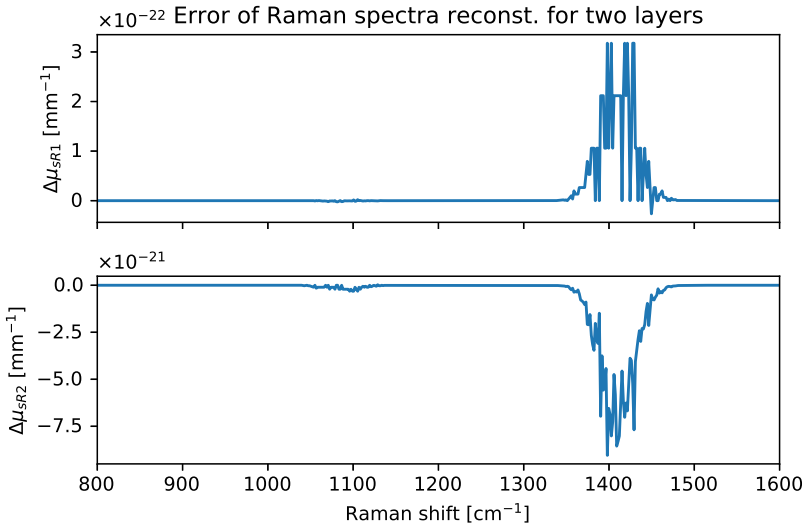

Figure 3.9: Difference (error) between the reconstructed and theoretical Raman spectra of the first layer (top) and second layer (bottom). The results are represented in form of error - deviation between reconstructed and theoretical value. Noise was completely neglected and IRF was set to unitary Dirac delta.

3.4 Systematic Study of Different Scenarios

In the previous section we have seen the effects of noise and instrument response function on the reconstruction, in a few exemplary cases. Besides the number of photon counts and FWHM of IRF, we could also vary geometrical and optical parameters. The process of varying parameters may continue infinitely. Nevertheless, if we perform a systematic analysis and introduce some measures of quality, we may obtain more quantitative conclusions. Results of such analysis will be presented in this section.

3.4.1 Figures of Merit - FOM

For the systematic study, we have to introduce some metrics to assess the quality of reconstruction. A few figures of merit (FOM) will be defined in this section. Before that, we formally assume notation: $\mu_{sR}(\lambda)$ - theoretical Raman spectrum, $\hat{\mu}_{sR}(\lambda)$ - reconstructed Raman spectrum, λ_m - wavelength of the peak in theoretical spectrum, $\hat{\lambda}_m$ - wavelength of the peak in reconstructed spectrum, $e(\lambda) = \hat{\mu}_{sR}(\lambda) - \mu_{sR}(\lambda)$ - reconstruction error at wavelength λ. When analysing reconstructed spectra, this error will have the sense of noise added to the theoretical spectrum.

Note that index 1 or 2 should be added to the labels of the above (and below) defined quantities, to specify which layer they refer to. The following figures of merit will be used.

- Relative error of the height of the peak: $\delta\mu_{sR} = \dfrac{\hat{\mu}_{sR}(\hat{\lambda}_m)}{\mu_{sR}(\lambda_m)} - 1.$
- Relative error of the position of the peak: $\delta\lambda_m = \dfrac{\hat{\lambda}_m}{\lambda_m} - 1.$
- Contrast-to-noise ratio: $\mathrm{CNR} = \dfrac{\hat{\mu}_{sR}(\hat{\lambda}_m)}{\sqrt{\mathrm{Var}}}$, where Var is the average variance calculated as $\mathrm{Var} = \dfrac{1}{N}\sum\limits_i e^2(\lambda_i)$, where the sum goes over all i satisfying $\mu_{sR}(\lambda_i) \geq 0.5\mu_{sR}(\lambda_m)$, and N is total number of such λ_i among all wavelengths of the discrete spectrum. Note that such defined Var has a meaning of the noise power.
- Suppression lower/upper: $S_{LU} = \dfrac{A_{L2}}{A_{L1}}$, where $A_{L2} = \sum\limits_j |\hat{\mu}_{sR2}(\lambda_j)|$ where the sum goes over all j satisfying $\mu_{sR2}(\lambda_j) \geq 0.5\mu_{sR2}(\lambda_{m2})$, while $A_{L1} = \sum\limits_i |\hat{\mu}_{sR2}(\lambda_i)|$ where the sum goes over all i satisfying $\mu_{sR1}(\lambda_i) \geq 0.5\mu_{sR1}(\lambda_{m1})$. It represents the area of reconstructed lower layer signal at the correct positions,

which is considered as useful signal, divided by the area of reconstructed lower layer signal at the positions around the peak of the upper layer, which is considered as undesirable coupling.

- Suppression upper/lower: $S_{UL} = \frac{A_{U1}}{A_{U2}}$, where $A_{U1} = \sum_i |\hat{\mu}_{sR1}(\lambda_i)|$ where the sum goes over all i satisfying $\mu_{sR1}(\lambda_i) \geq 0.5\mu_{sR1}(\lambda_{m1})$, while $A_{U2} = \sum_j |\hat{\mu}_{sR1}(\lambda_j)|$ where the sum goes over all j satisfying $\mu_{sR2}(\lambda_j) \geq 0.5\mu_{sR2}(\lambda_{m2})$. It represents the area of reconstructed upper layer signal at the correct positions, divided by the area of reconstructed upper layer signal at the positions around the peak of the lower layer.

3.4.2 Simulation Results and Discussion

In this section, we present the dependence of figures of merit on some optical and geometrical parameters, as well as more systematic view on noise and IRF. The interval for each parameter was chosen to cover the range of reasonable and realistic values. Here we will vary only one parameter at a time and observe the results. With this simple method, we may draw preliminary conclusions in which way and to what extent the chosen parameter affects the reconstruction.

Absorption coefficient of the upper layer

The first varied parameter was absorption of the first layer μ_{a1}. In Figure 3.10 two plots are presented. The upper one represents the contrast-to-noise ratio (CNR) for the reconstructed spectrum of the first layer, while the lower one refers to the CNR of the second layer. A decreasing trend can be observed in the upper layer, where the CNR drops from around 80 to below 20. These numbers are quite high, suggesting that the noise is not affecting the reconstruction of the upper layer spectrum on a major part of interval of simulated μ_{a1}; we can say the reconstruction is good in terms of CNR_1 for $\mu_{a1} \leq 0.03\,\mathrm{mm}^{-1}$. On the other hand, values for the second layer CNR are around 20-25, without meaningful impact from μ_{a1}. These numbers again are acceptable in terms of the ratio between the useful value and undesirable component, but as well a few times lower in comparison to the first layer CNR, when considering $\mu_{a1} \in [0; 0.02]$ mm^{-1}. The profile of $\mathrm{CNR}_1(\mu_{a1})$ is quite informative and we may conclude that higher absorptions of the first layer increase the number of lost photons in the first layer, and the signal compared to noise is degraded. The noise, in a broader sense defined as a difference between the reconstructed and the theoretical value, may come also from coupling with the second layer that is affected by very similar amount of noise for all simulated values of μ_{a1}, and thus making stable factor of disturbance for ever decreasing signal from the first layer.

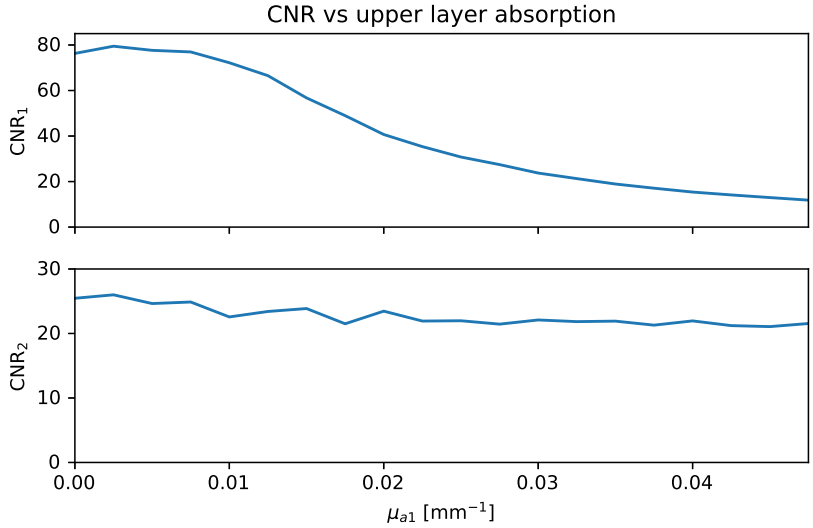

Figure 3.10: Contrast-to-noise ratio of the first layer (top) and second layer (bottom) dependence on the absorption coefficient of the first layer. Number of total photon counts was 10^6. IRF's FWHM was 100 ps. Geometrical parameters were $d_1 = 10\,\text{mm}$, $d_2 = 60\,\text{mm}$, $\rho = 10\,\text{mm}$. Optical parameters were $\mu_{a1} \in [0; 0.0475]\ \text{mm}^{-1}$, $\mu_{a2} = 0.01\,\text{mm}^{-1}$, $\mu'_{s1} = 1\,\text{mm}^{-1}$, $\mu'_{s2} = 1\,\text{mm}^{-1}$, $n_1 = n_2 = 1.4$.

If we look at the relative error of the height of the peak, shown in Figure 3.11, we may find similar conclusions. Second layer is affected to the similar extent over the whole simulated interval of μ_{a1}. The reconstruction error for the height of the peak is always between 7 and 10 percent. For the first layer, as CNR was decreasing with an increasing absorption, now the relative error of peak height is increasing from very good 2.5% to 12.5%, which is slightly above some acceptable limit of 10%. For what concerns the position of the peak, we obtained that it is always correct or almost correct, with extremely low relative errors ($2.3 \cdot 10^{-3}$ or less).

In Figure 3.12, both suppression factors are shown: upper/lower (above) and lower/upper (below). In the reconstructed spectrum of one layer this factor measures how well the spectral components from the other layer are suppressed. High values are desired, since it means that the importance of the spectrum obtained by the reconstruction at the desired positions is much higher than at the positions of the other layer's peak. We can observe that the suppression in the reconstructed spectrum of the upper layer is very high, roughly around 300, with lower values (still above 200) for higher absorptions μ_{a1}. The physical explanation for this slight decrease basically is the same as for the $\text{CNR}_1(\mu_{a1})$ trend. On the other hand, suppression factor in the reconstructed spectrum of the lower layer is around 10, which is the lowest acceptable limit for a good reconstruction. If we think more

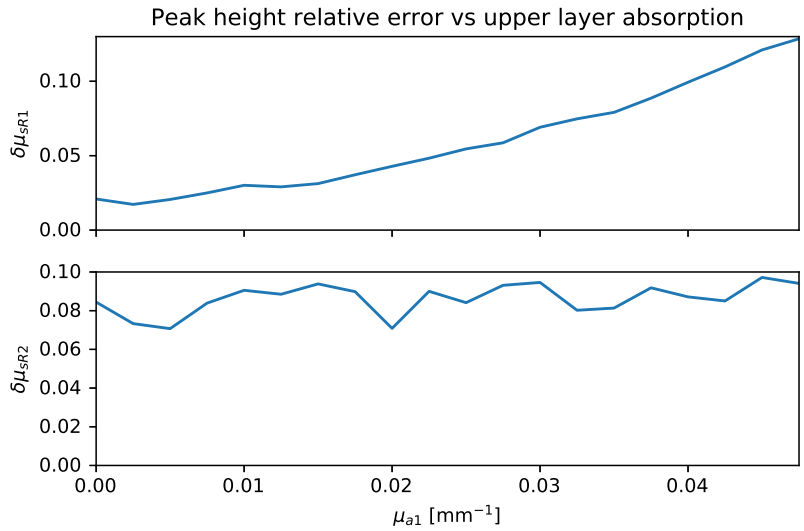

Figure 3.11: Relative error of the reconstruction of the peak height for the first layer (top) and second layer (bottom) versus absorption coefficient of the first layer. Number of total photon counts was 10^6. IRF's FWHM was 100 ps. Geometrical parameters were $d_1 = 10\,\text{mm}$, $d_2 = 60\,\text{mm}$, $\rho = 10\,\text{mm}$. Optical parameters were $\mu_{a1} \in [0; 0.0475]\ \text{mm}^{-1}$, $\mu_{a2} = 0.01\,\text{mm}^{-1}$, $\mu'_{s1} = 1\,\text{mm}^{-1}$, $\mu'_{s2} = 1\,\text{mm}^{-1}$, $n_1 = n_2 = 1.4$.

deeply, for higher μ_{a1}, photons from the top layer, which are scattering around, are absorbed in that layer to a greater extent than those that directly propagate deeper with much shorter paths. This is confirmed with S_{LU} factor plotted in Figure 3.12 (bottom part). Higher absorptions are favourable for the lower layer suppression of the upper layer signal, but there is also limit, since for extremely high absorptions, no photons would reach the bottom layer. This is, however, not so meaningful for the orders of magnitude, but demonstrates the physics.

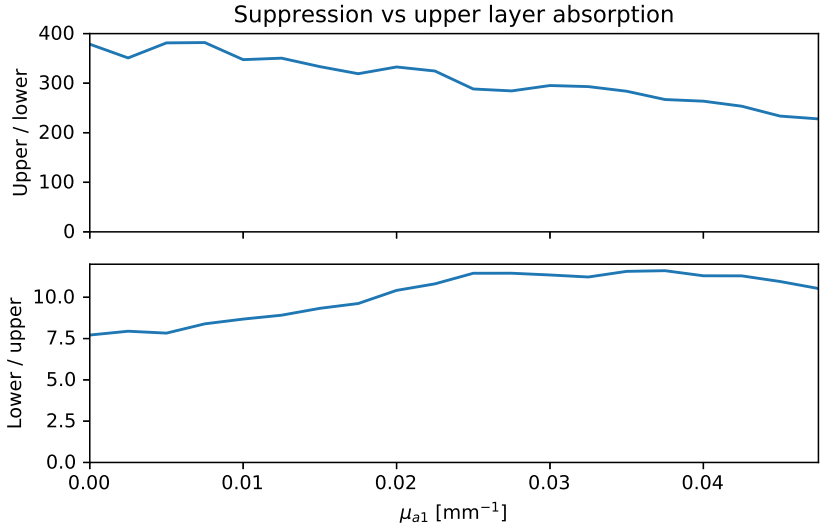

Figure 3.12: Suppression factor upper/lower (top) and lower/upper (bottom) dependence on the absorption coefficient of the first layer. Number of total photon counts was 10^6. IRF's FWHM was 100 ps. Geometrical parameters were $d_1 = 10\,\text{mm}$, $d_2 = 60\,\text{mm}$, $\rho = 10\,\text{mm}$. Optical parameters were $\mu_{a1} \in [0; 0.0475]\ \text{mm}^{-1}$, $\mu_{a2} = 0.01\,\text{mm}^{-1}$, $\mu'_{s1} = 1\,\text{mm}^{-1}$, $\mu'_{s2} = 1\,\text{mm}^{-1}$, $n_1 = n_2 = 1.4$.

Scattering coefficient of the upper layer

Now we study the effect of the scattering coefficient μ'_{s1} on our figures of merit. Again, we start with the contrast-to-noise ratio. Dependence of this parameter on the first layer scattering is reported in Figure 3.13. We see that for increasing μ'_{s1} from $0.5\,\text{mm}^{-1}$ to $2\,\text{mm}^{-1}$, CNR_1 increases from around 50 to almost 120. These numbers are high and suggest that the reconstruction of the top layer on the whole interval of μ'_{s1} is not affected by noise. Rising trend of CNR_1 can be explained by thinking about photon paths. For higher scattering coefficients, the photons will stay longer in the first layer and the signal from that layer will be much more intense than the signal from the bottom layer, since it would be more difficult for photons to straightly reach the depth. For what regards the contrast-to-noise ratio of the second layer, it is around 20-25, and is not significantly affected by the parameter μ'_{s1}. Conclusions may be similar to those from the bottom part of Figure 3.10.

We have observed so far that the figures of merit we are considering are mutually correlated. Therefore, for the analysis of the plots from Figure 3.14 we can have very similar conclusions to those drawn from the analysis of Figure 3.13. The relative error of the height of the peak of first layer is decreasing when μ'_{s1} is increasing, which is in accordance with theory exposed above. Values from 4%

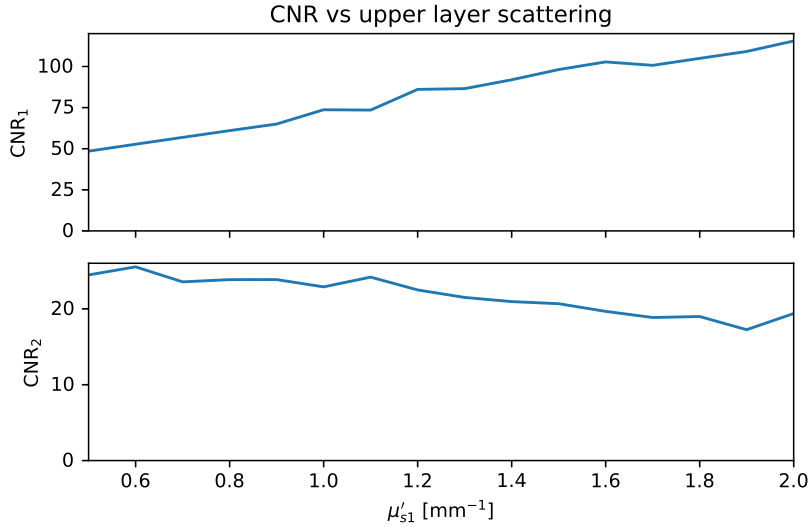

Figure 3.13: Contrast-to-noise ratio of the first layer (top) and second layer (bottom) dependence on the reduced scattering coefficient of the first layer. Number of total photon counts was 10^6. IRF's FWHM was 100 ps. Geometrical parameters were $d_1 = 10\,\text{mm}$, $d_2 = 60\,\text{mm}$, $\rho = 10\,\text{mm}$. Optical parameters were $\mu_{a1} = 0.01\,\text{mm}^{-1}$, $\mu_{a2} = 0.01\,\text{mm}^{-1}$, $\mu'_{s1} \in [0.5; 2]\ \text{mm}^{-1}$, $\mu'_{s2} = 1\,\text{mm}^{-1}$, $n_1 = n_2 = 1.4$.

down to 1% are excellent for the reconstruction of the first layer's peak. However, for the second layer, the relative error exceeds the limit of tolerance for higher scatterings μ'_{s1}.

In Figure 3.15, suppression factors are plotted. In the reconstructed spectrum of the upper layer, components from the lower layer are successfully suppressed, with factor rising from a few hundreds for small μ'_{s1} to almost 1500 for $\mu'_{s1} = 2\,\text{mm}^{-1}$. However, suppression of the upper layer in the reconstructed spectrum of the lower layer is acceptable only for smaller μ'_{s1}, we can estimate $\mu'_{s1} \leq 1\,\text{mm}^{-1}$. The decreasing trend could be explained by losing of "sharpness", due to the scattering, or in other words, smaller number of photons propagates directly to the lower layer, allowing the upper layer signal to be dominant.

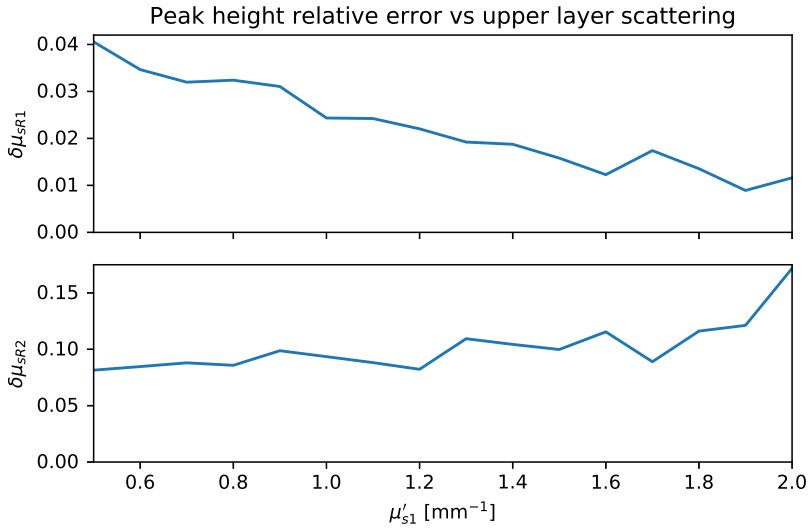

Figure 3.14: Relative error of the peak height reconstruction for the first layer (top) and second layer (bottom) versus reduced scattering coefficient of the first layer. Total of 10^6 photon counts, IRF's FWHM = 100 ps. Geometrical parameters were $d_1 = 10\,\text{mm}$, $d_2 = 60\,\text{mm}$, $\rho = 10\,\text{mm}$. Optical parameters were $\mu_{a1} = \mu_{a2} = 0.01\,\text{mm}^{-1}$, $\mu'_{s1} \in [0.5; 2]\ \text{mm}^{-1}$, $\mu'_{s2} = 1\,\text{mm}^{-1}$, $n_1 = n_2 = 1.4$.

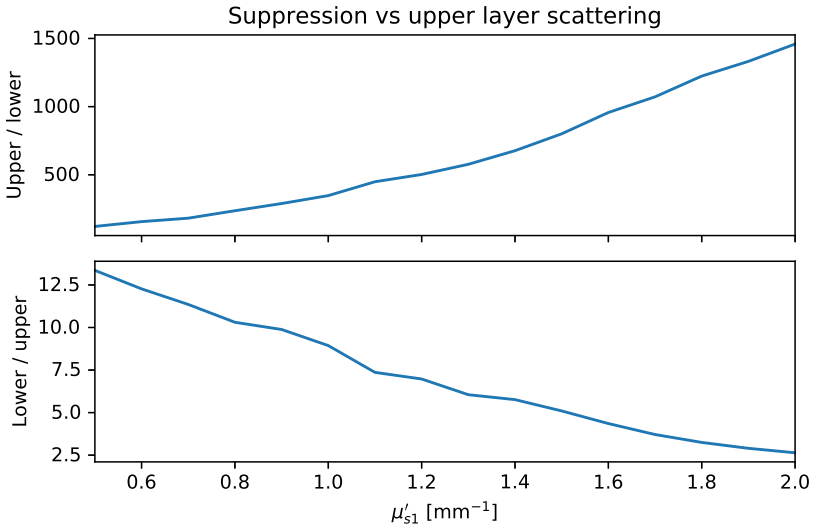

Figure 3.15: Suppression factor upper/lower (top) and lower/upper (bottom) dependence on the reduced scattering coefficient of the first layer. Number of total photon counts was 10^6. IRF's FWHM was 100 ps. Geometrical parameters were $d_1 = 10\,\text{mm}$, $d_2 = 60\,\text{mm}$, $\rho = 10\,\text{mm}$. Optical parameters were $\mu_{a1} = 0.01\,\text{mm}^{-1}$, $\mu_{a2} = 0.01\,\text{mm}^{-1}$, $\mu'_{s1} \in [0.5; 2]\ \text{mm}^{-1}$, $\mu'_{s2} = 1\,\text{mm}^{-1}$, $n_1 = n_2 = 1.4$.

Thickness of the upper layer

We now move to geometrical parameters analysis. In the following simulations, the thickness of the upper layer d_1 was varied. Results are shown in Figures 3.16 (CNR), 3.17 (peak height relative error) and 3.18 (suppression of spectral components of one layer in reconstructed spectrum of another layer). As expected, for thin top layers (up to 10-12 mm), reconstruction of the bottom layer could be considered as acceptable. Only in terms of the suppression factor, we could impose a limit of $d_1 \leq 10\,\text{mm}$ to guarantee a reliable reconstruction, under the conditions considered. For very thin top layers (less than 3 mm), reconstruction of its spectrum is affected by the bottom layer's spectrum. An additional comment on the bottom plot of Figure 3.16: a sudden increment of CNR_2 is not natural. It appears as a consequence of a wrong reconstruction of the position of the peak of the bottom layer. For all values of $d_1 \geq 15\,\text{mm}$, there is no way to obtain reliable reconstruction of the bottom layer. Interesting behaviour can be seen on the plots of suppression (Figure 3.18). They are given in logarithmic scale, and represented in such way, they appear to be linear.

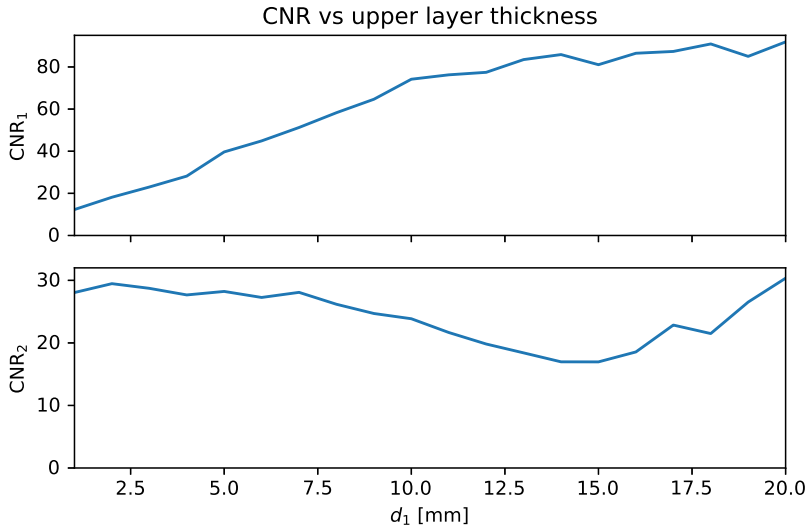

Figure 3.16: Contrast-to-noise ratio of the first layer (top) and second layer (bottom) dependence on the reduced scattering coefficient of the first layer. Total of 10^6 photon counts, IRF's FWHM = 100 ps. Geometrical parameters were $d_1 \in [1; 20]$ mm, $d_2 = 60\,\text{mm}$, $\rho = 10\,\text{mm}$. Optical parameters were $\mu_{a1} = \mu_{a2} = 0.01\,\text{mm}^{-1}$, $\mu'_{s1} = \mu'_{s2} = 1\,\text{mm}^{-1}$, $n_1 = n_2 = 1.4$.

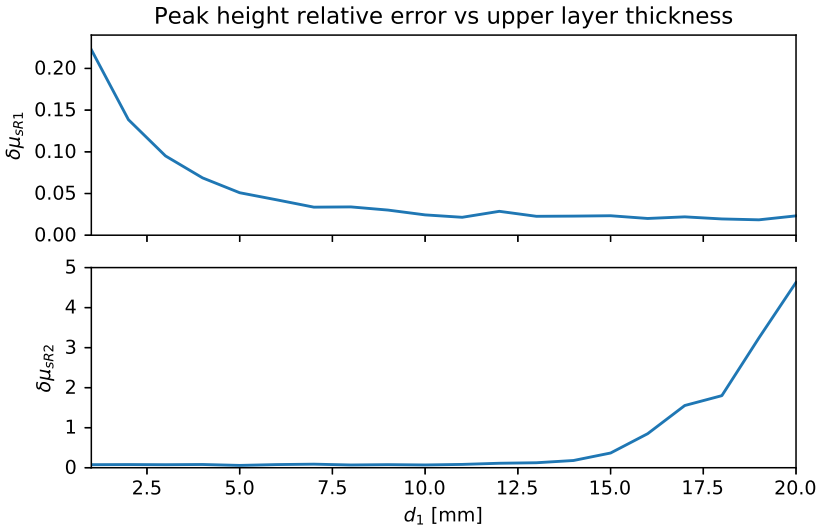

Figure 3.17: Relative error of the peak height reconstruction for the first layer (top) and second layer (bottom) versus thickness of the first layer. Total of 10^6 photon counts, IRF's FWHM = 100 ps. Geometrical parameters were $d_1 \in [1; 20]$ mm, $d_2 = 60$ mm, $\rho = 10$ mm. Optical parameters were $\mu_{a1} = \mu_{a2} = 0.01\,\mathrm{mm}^{-1}$, $\mu'_{s1} = \mu'_{s2} = 1\,\mathrm{mm}^{-1}$, $n_1 = n_2 = 1.4$.

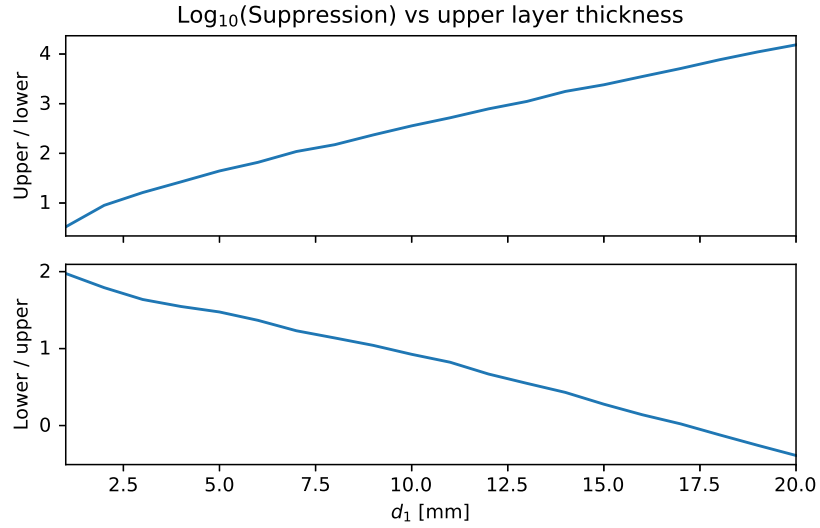

Figure 3.18: Suppression factor upper/lower (top) and lower/upper (bottom) dependence on the thickness of the first layer. Logarithmic (base 10) scale for suppression was adopted. Total of 10^6 photon counts, IRF's FWHM = 100 ps. Geometrical parameters were $d_1 \in [1; 20]$ mm, $d_2 = 60$ mm, $\rho = 10$ mm. Optical parameters were $\mu_{a1} = \mu_{a2} = 0.01\,\mathrm{mm}^{-1}$, $\mu'_{s1} = \mu'_{s2} = 1\,\mathrm{mm}^{-1}$, $n_1 = n_2 = 1.4$.

Distance between the source and the detector

We can now analyze the figures of merit when the distance between the source and detector is varied from $\rho = 6\,\text{mm}$ to $\rho = 32\,\text{mm}$. The results are shown, in usual order, in Figures 3.19 (CNR), 3.20 (peak height relative error) and 3.21 (suppression upper/lower and lower/upper). As expected, according to the general concept of SORS (as described in Section 1.3.2), greater source-detector distances are favourable for detecting the signal from depth. Therefore, the results which show the increament of CNR_2 and of suppression factor S_{LU}, as well as the decreament of relative error of the reconstructed peak height $\delta\mu'_{sR2}$, with increasing values for ρ are not surprising. We can say that for $\rho \geq 16\,\text{mm}$ results are very good for both the reconstructed spectra. Optimal values for the top layer are smaller, but if the goal is to successfully reconstruct both layers and with special accent on the information from depth, then one should look for greater source-detector separations. However, it is expected to detect fewer photons when the separation between the source and the detector grows. Number of detected photons should not decrease so much, in order to be able to collect reliable (strong enough in comparison with noise) signal in a reasonable amount of time. Note that here the total number of photon counts was always 10^6, which might be unreachable for some greater distances between the source and the detector.

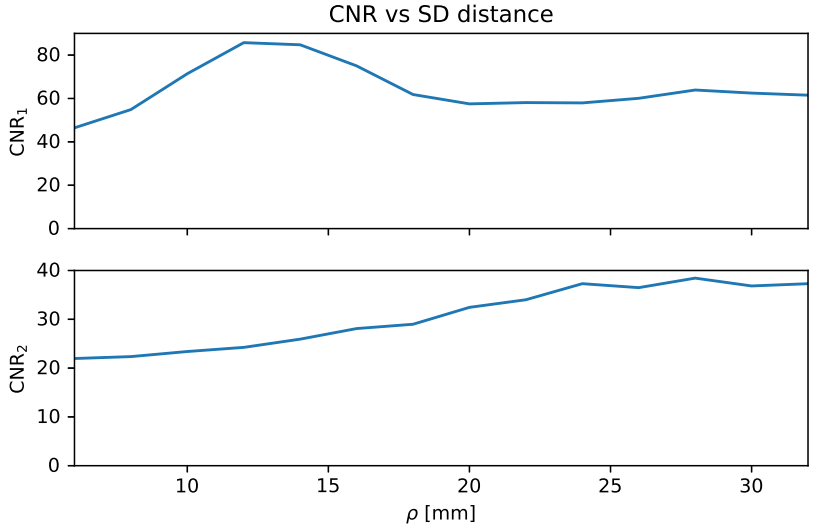

Figure 3.19: Contrast-to-noise ratio of the first layer (top) and second layer (bottom) dependence on the source-detector separation. Total of 10^6 photon counts was assumed, IRF's FWHM = 100 ps. Geometrical parameters were $d_1 = 10\,\text{mm}$, $d_2 = 60\,\text{mm}$, $\rho \in [6; 32]$ mm. Optical parameters were $\mu_{a1} = \mu_{a2} = 0.01\,\text{mm}^{-1}$, $\mu'_{s1} = \mu'_{s2} = 1\,\text{mm}^{-1}$, $n_1 = n_2 = 1.4$.

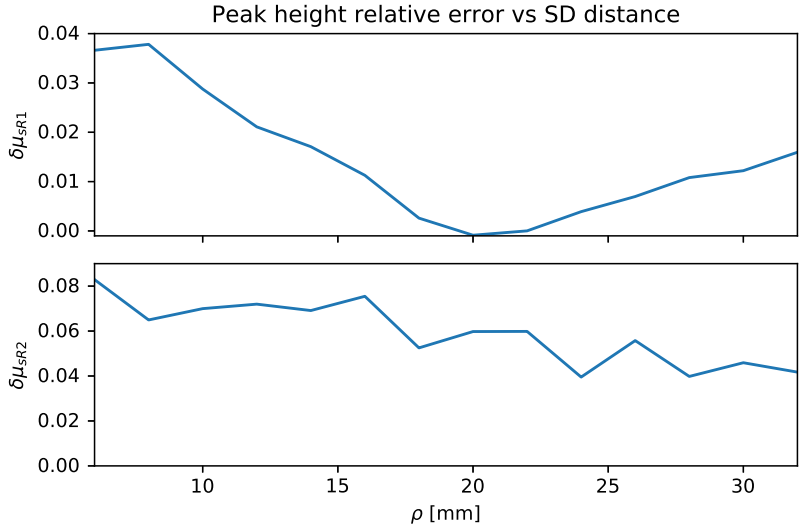

Figure 3.20: Relative error of the peak height reconstruction for the first layer (top) and second layer (bottom) versus source-detector distance. Total of 10^6 photon counts was assumed, IRF's FWHM = 100 ps, $d_1 = 10\,\text{mm}$, $d_2 = 60\,\text{mm}$, $\rho \in [6; 32]$ mm, $\mu_{a1} = \mu_{a2} = 0.01\,\text{mm}^{-1}$, $\mu'_{s1} = \mu'_{s2} = 1\,\text{mm}^{-1}$, $n_1 = n_2 = 1.4$.

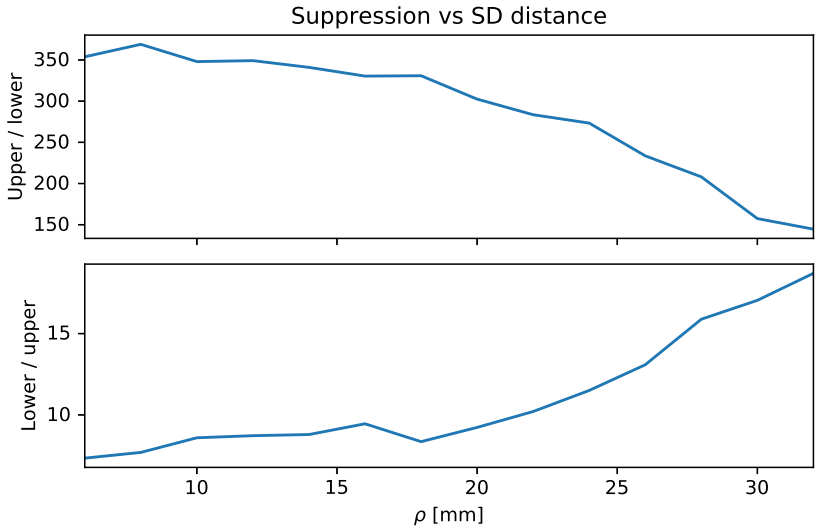

Figure 3.21: Suppression factor upper/lower (top) and lower/upper (bottom) versus the source-detector distance. IRF's FWHM = 100 ps, number of photon counts was 10^6. Geometrical parameters: $d_1 = 10\,\text{mm}$, $d_2 = 60\,\text{mm}$, $\rho \in [6; 32]$ mm. Optical parameters: $\mu_{a1} = \mu_{a2} = 0.01\,\text{mm}^{-1}$, $\mu'_{s1} = \mu'_{s2} = 1\,\text{mm}^{-1}$, $n_1 = n_2 = 1.4$.

Instrument Response Function (IRF)

Firstly, FWHM of the instrument response function is varied. Note that the reconstructions were always performed without the knowledge of the IRF. Here we just modelled what could be the IRF (width in time is the most important information, that is why we are interested in FWHM). Knowing the exact impulse response function of the acquisition system, one could think about deconvolving the obtained signal and eliminating the factor of the instrument. However, this was not done here. We just study the effects, since for practical use one should know what can disturb the performances of the system, and to what extent the system is robust to the errors. Results are shown in Figures 3.22, 3.23 and 3.24. Obviously, as it was expected, wide impulse response function in time domain gives raise to stronger coupling between the layers and therefore deterioration of the reconstruction results. For FWHM $\geq 200\,\text{ps}$, suppression of upper layer from the spectrum of the lower layer is not acceptable. Decreasing trend for both suppression factors and increasing trend for relative errors of the peak height reconstruction is expected, when FWHM increases. Contrast-to-noise ratio for both layers was always in acceptable region, but we must note that for FWHM $\geq 460\,\text{ps}$, the position of the peak of the second layer in its reconstructed spectrum had unacceptable errors.

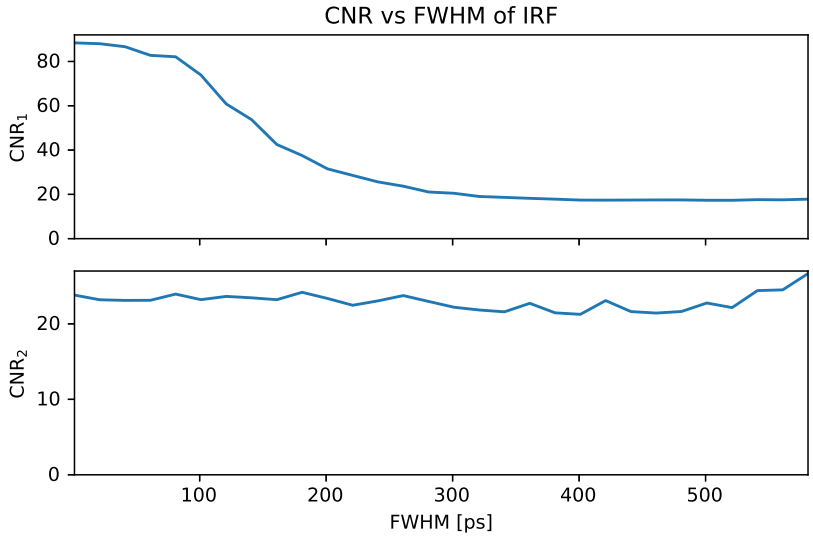

Figure 3.22: Contrast-to-noise ratio of the first layer (top) and second layer (bottom) dependence on the FWHM of the IRF. Total of 10^6 photon counts was assumed, FWHM $\in$ [1,581] ps. Geometrical parameters were $d_1 = 10\,\text{mm}$, $d_2 = 60\,\text{mm}$, $\rho = 10\,\text{mm}$. Optical parameters were $\mu_{a1} = \mu_{a2} = 0.01\,\text{mm}^{-1}$, $\mu'_{s1} = \mu'_{s2} = 1\,\text{mm}^{-1}$, $n_1 = n_2 = 1.4$.

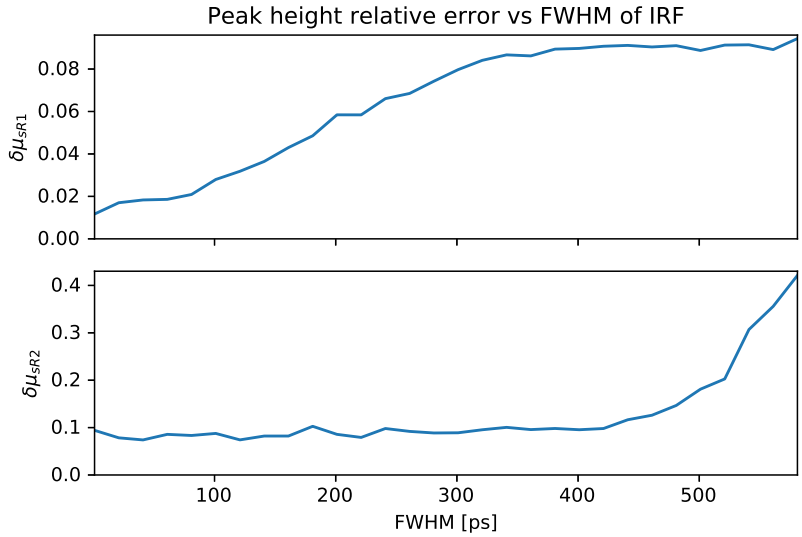

Figure 3.23: Relative error of the peak height reconstruction for the first layer (top) and second layer (bottom) versus FWHM of the IRF. Total of 10^6 photon counts was assumed, FWHM $\in$ [1,581] ps. Geometrical parameters were $d_1 = 10\,\text{mm}$, $d_2 = 60\,\text{mm}$, $\rho = 10\,\text{mm}$. Optical parameters were $\mu_{a1} = \mu_{a2} = 0.01\,\text{mm}^{-1}$, $\mu'_{s1} = \mu'_{s2} = 1\,\text{mm}^{-1}$, $n_1 = n_2 = 1.4$.

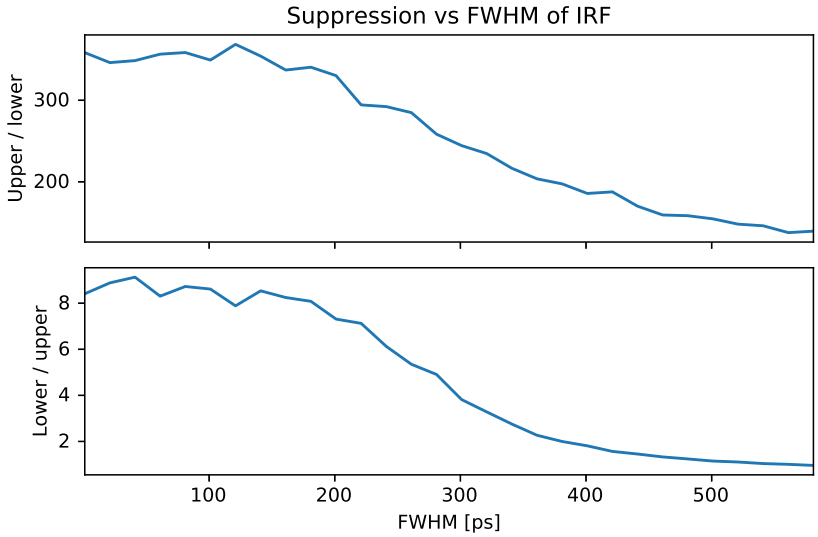

Figure 3.24: Suppression factor upper/lower (top) and lower/upper (bottom) dependence on the FWHM of the IRF. Total of 10^6 photon counts was assumed, FWHM $\in$ [1; 581] ps. Geometrical parameters were $d_1 = 10\,\text{mm}$, $d_2 = 60\,\text{mm}$, $\rho = 10\,\text{mm}$. Optical parameters were $\mu_{a1} = \mu_{a2} = 0.01\,\text{mm}^{-1}$, $\mu'_{s1} = \mu'_{s2} = 1\,\text{mm}^{-1}$, $n_1 = n_2 = 1.4$.

Number of photon counts

Finally, here we present the results of the noise simulations, or in a different way, number of photon counts (the greater this number is, the lower the impact of noise). Signal-to-noise ratio, due to Poisson noise is proportional to the square root of number of photon counts. Therefore, we expect an improvement of the contrast-to-noise ratio, a decrease of the relative error of the reconstructed height of the peak and, of course, an increase of the suppression of unwanted components in reconstructed spectra of both layers. The results, presented in Figures 3.25, 3.26 and 3.27, proved our expectations to be correct. From numerical values of the figures of merit obtained, we can conclude that the number of collected photons should be 10^6 or higher, to ensure reliable reconstruction with the chosen configuration of parameters.

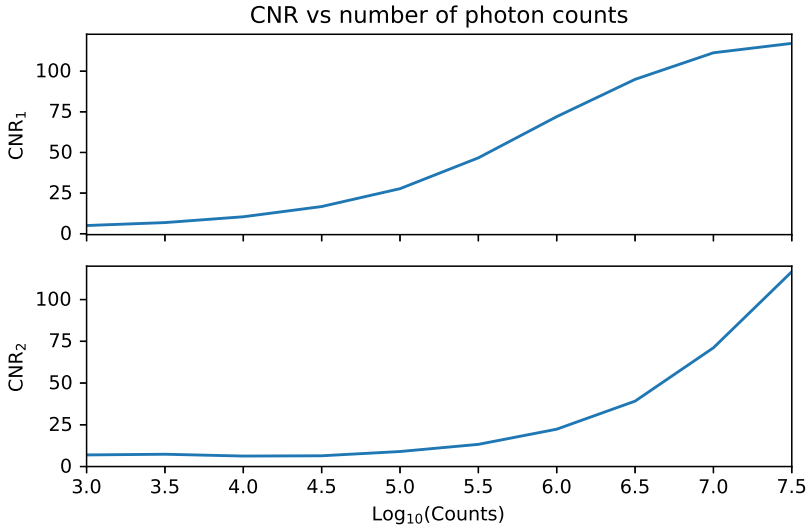

Figure 3.25: Contrast-to-noise ratio of the first layer (top) and second layer (bottom) dependence on the photon counts ($\log_{10}$ scale). Number of photon counts was in the interval $[10^3; 10^{7.5})$. FWHM = 100 ps. Geometrical parameters were $d_1 = 10\,\text{mm}$, $d_2 = 60\,\text{mm}$, $\rho = 10\,\text{mm}$. Optical parameters were $\mu_{a1} = \mu_{a2} = 0.01\,\text{mm}^{-1}$, $\mu'_{s1} = \mu'_{s2} = 1\,\text{mm}^{-1}$, $n_1 = n_2 = 1.4$.

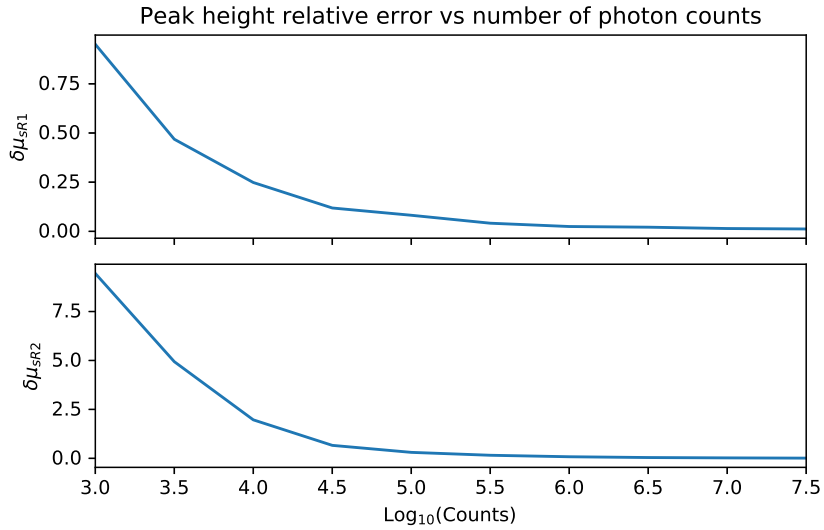

Figure 3.26: Relative error of the peak height reconstruction for the first layer (top) and second layer (bottom) versus photon counts ($\log_{10}$ scale). Number of photon counts was in the interval $[10^3; 10^{7.5})$. FWHM $= 100\,\mathrm{ps}$. Geometrical parameters were $d_1 = 10\,\mathrm{mm}$, $d_2 = 60\,\mathrm{mm}$, $\rho = 10\,\mathrm{mm}$. Optical parameters were $\mu_{a1} = \mu_{a2} = 0.01\,\mathrm{mm}^{-1}$, $\mu'_{s1} = \mu'_{s2} = 1\,\mathrm{mm}^{-1}$, $n_1 = n_2 = 1.4$.

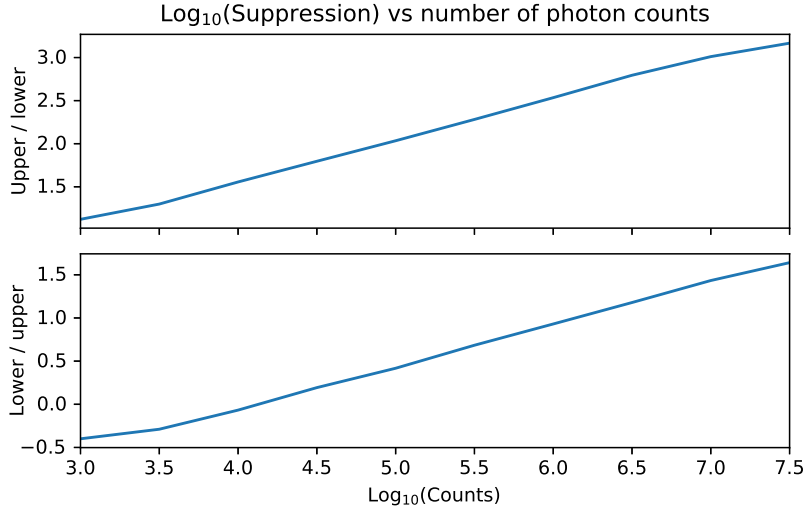

Figure 3.27: Base 10 logarithm of the suppression factor upper/lower (top) and lower/upper (bottom) versus the number of photon counts ($\log_{10}$ scale). Number of photon counts was in the interval $[10^3; 10^{7.5})$. FWHM $= 100\,\mathrm{ps}$. Geometrical parameters were $d_1 = 10\,\mathrm{mm}$, $d_2 = 60\,\mathrm{mm}$, $\rho = 10\,\mathrm{mm}$. Optical parameters were $\mu_{a1} = \mu_{a2} = 0.01\,\mathrm{mm}^{-1}$, $\mu'_{s1} = \mu'_{s2} = 1\,\mathrm{mm}^{-1}$, $n_1 = n_2 = 1.4$.

3.4.3 Some Results of Two Parameter Variation

In the previous section, we could see the impact of single parameters on the figures of merit. Here we would like to present some interesting combinations of two parameters varying at the same time. Since our main goal is to faithfully reconstruct the spectrum of the bottom layer (actually both layers, but the top layer is usually not a concern), in this section we will just present the results for the suppression factor of the top layer's spectral components in the reconstructed spectrum of the bottom layer.

In Figure 3.28, two parameters μ_{a1} and μ'_{s1} were varied at the same time. Four discrete curves for four different values of μ'_{s1} were plotted over the whole interval of μ_{a1}. Obtained results show us what we expected. For higher scatterings in the first layer, reconstruction of the second layer is deteriorated. However, for lower values of μ'_{s1}, suppression factor S_{LU} is very good over the whole inspected interval of μ_{a1}. Eventually, to have better suppression of first layer's components from the reconstructed spectrum of the second layer, one would need higher abosrption μ_{a1} and lower scattering μ'_{s1} in the first layer.

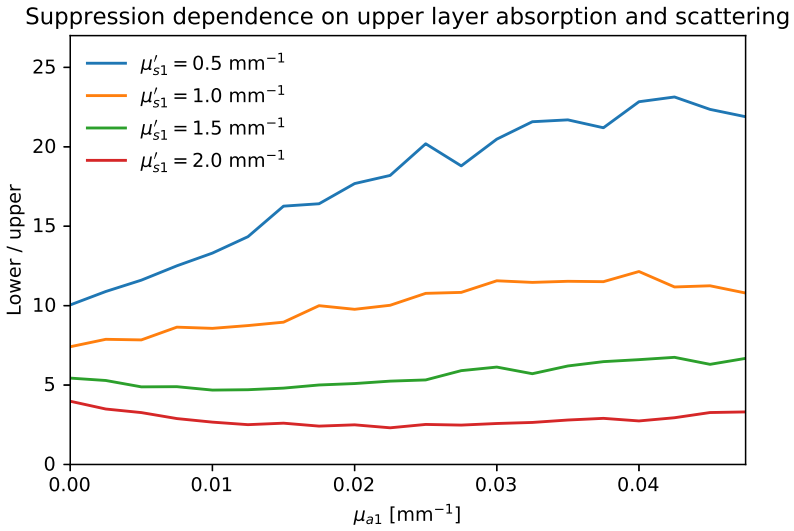

Figure 3.28: Suppression factor lower / upper dependence on the absorption coefficient of the first layer. Four curves are represented for four different reduced scatterings coefficients of the first layer. Number of photon counts was 10^6, FWHM = 100 ps. Geometrical parameters were $d_1 = 10$ mm, $d_2 = 60$ mm, $\rho = 10$ mm. Optical parameters were $\mu_{a1} \in [0; 0.0475]$ mm^{-1}, $\mu'_{s1} \in [0.5; 2.0]$ mm^{-1}, $\mu_{a2} = 0.01$ mm^{-1}, $\mu'_{s2} = 1$ mm^{-1}, $n_1 = n_2 = 1.4$.

In Figure 3.29, two parameters: absorption coefficient of the first layer μ_{a1} and total photon counts C_t were varied at the same time. Four discrete curves for four

different photon counts levels were plotted over the whole interval of μ_{a1}. It is evident that the total number of photon counts is a dominant factor here, which determines the quality of reconstruction.

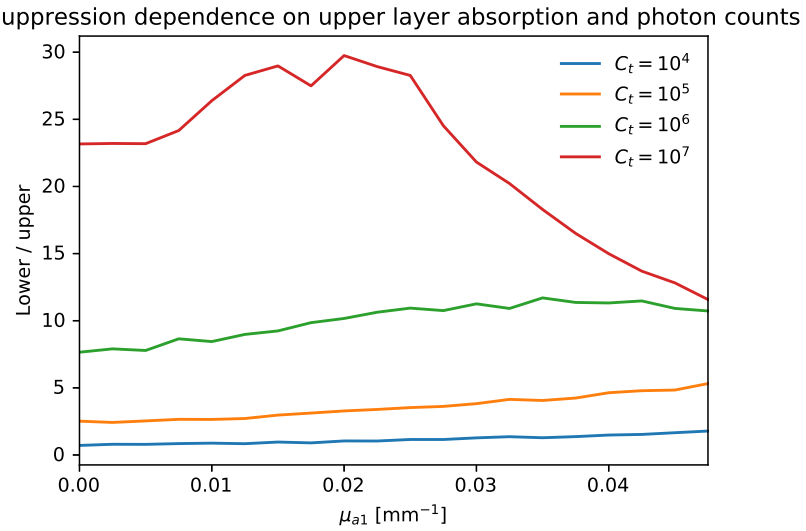

Figure 3.29: Suppression factor lower / upper dependence on the absorption coefficient of the first layer. Four curves are represented for four different photon counts. Number of photon counts was from the set $\{10^4, 10^5, 10^6, 10^7\}$. IRF's FWHM = 100 ps. Geometrical parameters were $d_1 = 10\,\text{mm}$, $d_2 = 60\,\text{mm}$, $\rho = 10\,\text{mm}$. Optical parameters were $\mu_{a1} = 0.01\,\text{mm}^{-1}$, $\mu'_{s1} = 1\,\text{mm}^{-1}$, $\mu_{a2} = 0.01\,\text{mm}^{-1}$, $\mu'_{s2} = 1\,\text{mm}^{-1}$, $n_1 = n_2 = 1.4$.

In Figure 3.30, two parameters: thickness of the first layer d_1 and source-detector distance ρ were varied at the same time. Four discrete curves for four different source-detector separations were plotted over the whole interval of d_1. For thin top layers, there is no much difference between these curves, and thus smaller SD separation could be fine, because of the intensity of the signal detected. However, thicker upper layers would require greater distances between the source and the detector in order to improve the reconstruction of the second layer. If the upper layer is thicker than 15 mm, reconstruction of the lower layer spectrum would be noticeably contaminated with the upper layer components even for greater source-detector separations.

In Figure 3.31, two parameters: thickness d_1 and absorption coefficient μ_{a1} of the first layer were varied at the same time. Six discrete curves for six different μ_{a1} were plotted over the whole interval of d_1. For $d_1 \leq 12\,\text{mm}$, behaviour of the curves is similar, for better suppression more favourable are those with higher μ_{a1}. What happens for thicker top layers is interesting, but not completely surprising.

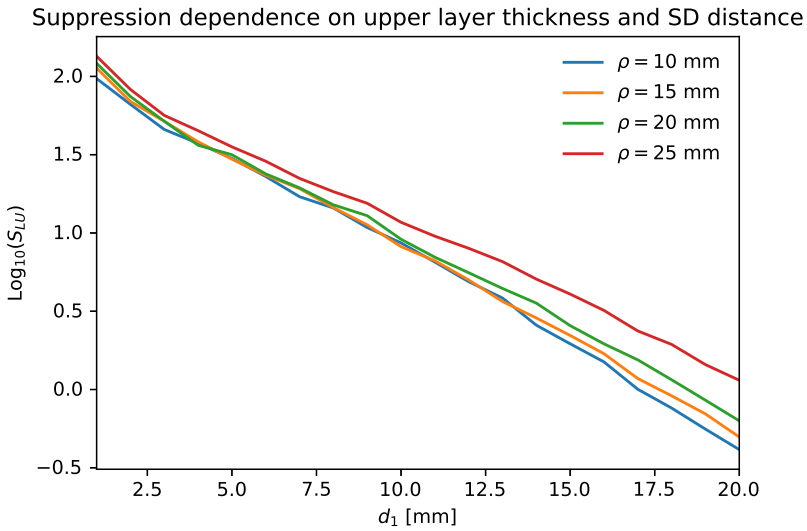

Figure 3.30: Base 10 logarithm of the suppression factor lower / upper dependence on the thickness of the first layer. Four curves are represented for four different source-detector distances. Number of photon counts was 10^6. IRF's FWHM $= 100\,\text{ps}$. Geometrical parameters were $d_1 \in [1; 20]$ mm, $d_2 = 60\,\text{mm}$, $\rho \in \{10, 15, 20, 25\}$ mm. Optical parameters were $\mu_{a1} = 0.01\,\text{mm}^{-1}$, $\mu'_{s1} = 1\,\text{mm}^{-1}$, $\mu_{a2} = 0.01\,\text{mm}^{-1}$, $\mu'_{s2} = 1\,\text{mm}^{-1}$, $n_1 = n_2 = 1.4$.

At some point, for thick enough top layers with high enough absorption coefficient, photons can barely reach the bottom layer, thus producing poor Raman signal from depth. Even high absorptions μ_{a1}, which in general favour sharpening of the signal because of the fact that photons with more direct paths survive rather than those scattering around, are not helpful in overcoming physical barrier of thick top layer. On the contrary, they make it even worse.

In Figure 3.32 it can be clearly seen that the FWHM of IRF not higher than 150 ps produce almost no effect on the reconstruction, whatever the thickness of the upper layer is. Thickness itself is very limiting factor, as we have seen already on many examples.

The impact of noise, or total number of photon counts, could be easily understood from Figure 3.33, where suppression factor S_{LU} for different photon counts levels was plotted over the whole interval of the top layer thicknesses.

From Figure 3.34, we can see that the suppression factor S_{LU} increases, as source-detector distance ρ increases, starting from $\rho \geq 16\,\text{mm}$, if the constant number of collected photons is assumed. This could be problematic in practice, since the rightmost parts (for greater ρ) of green and red curve (higher number of photon counts) could be unreachable.

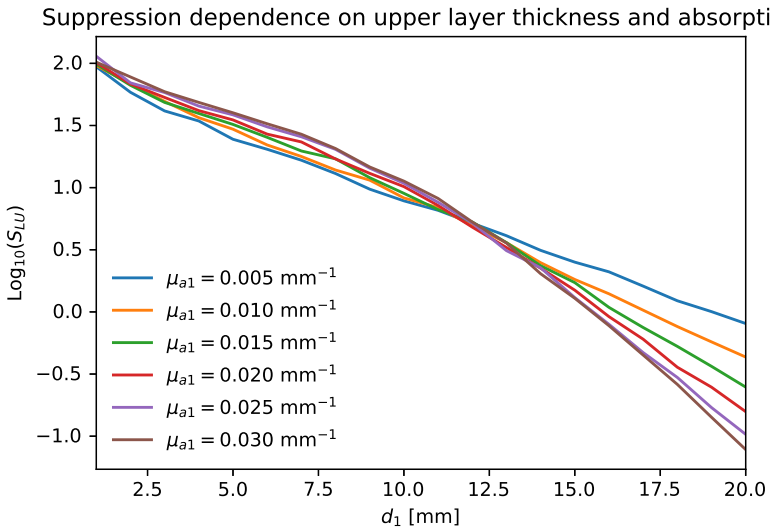

Figure 3.31: Base 10 logarithm of the suppression factor lower / upper dependence on the thickness of the first layer. Six curves are represented for six different absorption coefficients of the first layer. Number of photon counts was 10^6. IRF's FWHM $= 100\,\text{ps}$. Geometrical parameters were $d_1 \in [1; 20]$ mm, $d_2 = 60\,\text{mm}$, $\rho = 10\,\text{mm}$. Optical parameters were $\mu_{a1} \in [0.005; 0.030]$ mm^{-1}, $\mu'_{s1} = 1\,\text{mm}^{-1}$, $\mu_{a2} = 0.01\,\text{mm}^{-1}$, $\mu'_{s2} = 1\,\text{mm}^{-1}$, $n_1 = n_2 = 1.4$.

From Figure 3.35, we can observe that greater source-detector distances improve the reconstruction of the second layer, when the reduced scattering coefficient of the first layer is high.

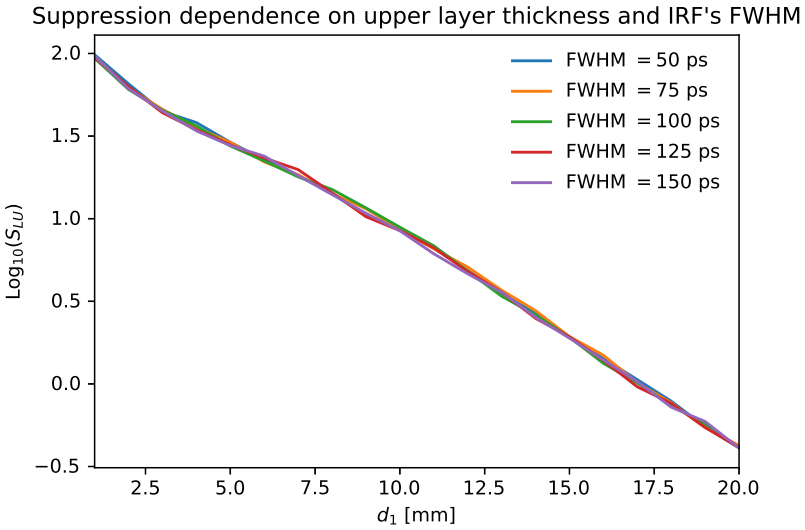

Figure 3.32: Base 10 logarithm of the suppression factor lower / upper dependence on the thickness of the first layer. Five curves are represented for five different values of IRF's FWHM $\in \{50, 75, 100, 125, 150\}$ ps. Number of photon counts was 10^6. Geometrical parameters were $d_1 \in [1; 20]$ mm, $d_2 = 60$ mm, $\rho = 10$ mm. Optical parameters were $\mu_{a1} = \mu_{a2} = 0.01\,\mathrm{mm}^{-1}$, $\mu'_{s1} = \mu'_{s2} = 1\,\mathrm{mm}^{-1}$, $n_1 = n_2 = 1.4$.

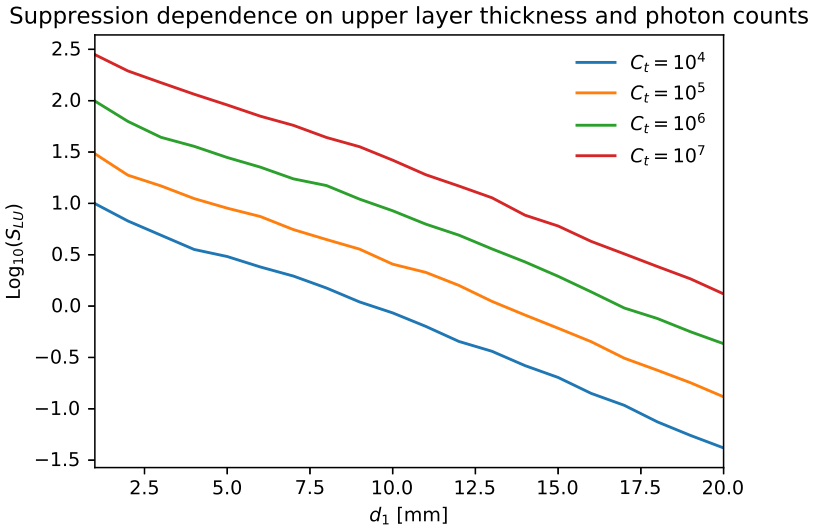

Figure 3.33: Base 10 logarithm of the suppression factor lower / upper dependence on the thickness of the first layer. Four curves are represented for four different values of photon counts from the set $\{10^4, 10^5, 10^6, 10^7\}$. IRF's FWHM = 100 ps. Geometrical parameters were $d_1 \in [1; 20]$ mm, $d_2 = 60$ mm, $\rho = 10$ mm. Optical parameters were $\mu_{a1} = \mu_{a2} = 0.01\,\mathrm{mm}^{-1}$, $\mu'_{s1} = \mu'_{s2} = 1\,\mathrm{mm}^{-1}$, $n_1 = n_2 = 1.4$.

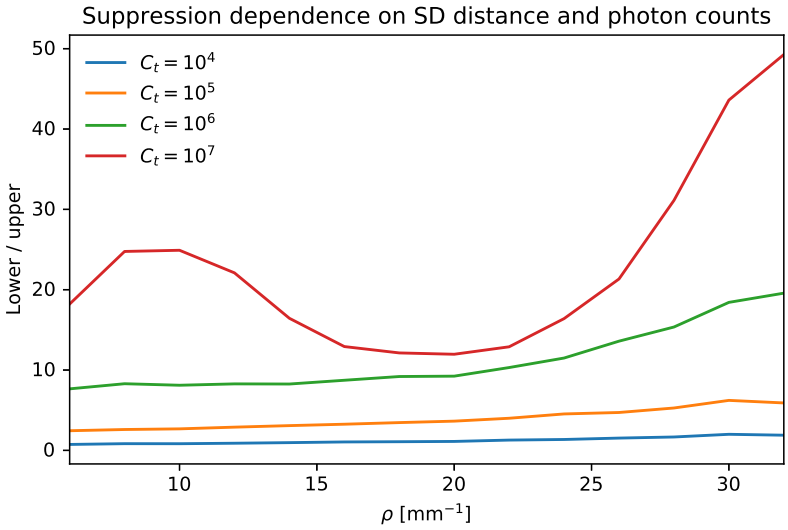

Figure 3.34: Suppression factor lower / upper dependence on the source-detector distance. Four curves are represented for four different values of photon counts from the set $\{10^4, 10^5, 10^6, 10^7\}$. IRF's FWHM = 100 ps. Geometrical parameters were $d_1 = 10$mm, $d_2 = 60$ mm, $\rho \in [6; 32]$ mm. Optical parameters were $\mu_{a1} = \mu_{a2} = 0.01\,\mathrm{mm}^{-1}$, $\mu'_{s1} = \mu'_{s2} = 1\,\mathrm{mm}^{-1}$, $n_1 = n_2 = 1.4$.

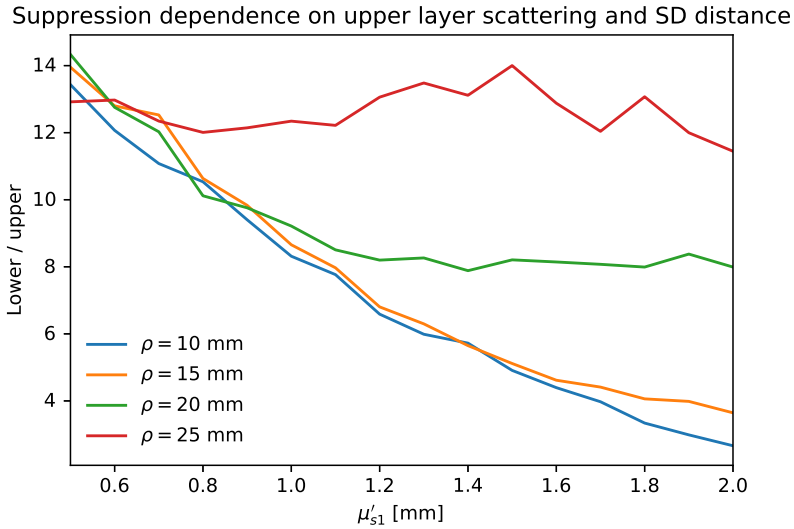

Figure 3.35: Suppression factor lower / upper dependence on the reduced scattering of the first layer. Four curves are represented for four different SD distances. Number of photon counts was 10^6. IRF's FWHM = 100 ps. Geometrical parameters were $d_1 = 10$mm, $d_2 = 60$ mm, $\rho \in \{10, 15, 20, 25\}$ mm. Optical parameters were $\mu_{a1} = \mu_{a2} = 0.01\,\mathrm{mm}^{-1}$, $\mu'_{s1} \in [0.5; 2]$, $\mu'_{s2} = 1\,\mathrm{mm}^{-1}$, $n_1 = n_2 = 1.4$.

3.5 Conclusion

We applied the reconstruction method based on the two-layer Raman heuristic model, presented in Chapter 2. The reconstructions were performed on simulated data. To account for features of real systems, a convolution with the instrument impulse response function was added, as well as the detection noise.

The systematic analysis was performed, involving the effects of different factors on the figures of merit. These factors were key optical parameters: absorption coefficient of the upper layer, reduced scattering coefficient of the upper layer, then geometrical parameters: thickness of the upper layer, distance between the source and detector, and finally FWHM of the instrument response function and number of photon counts. Only one parameter was varied at a time. Results in the form of figure of merit plots were reported. The discussed figures of merit were: relative error of the peak height reconstruction, contrast-to-noise ratio, factor of suppression of spectral components of one layer in the reconstructed spectrum of the other layer. From the figures presented, we could confirm some theories of Diffuse Optics, we could also learn how sensitive to noise the reconstruction process is. Moreover, we discussed the intervals of parameters in which the reconstruction is reliable. Then, a few two-variable simulations were performed, to provide an overall image and help in formulating the conclusions.

In summary, we noticed that the reconstruction quality strongly depends on the thickness of the top layer. To have a reliable reconstruction, it is desirable that the upper layer is no more than 10 mm thick. Different source-detector separations could enhance the reconstruction of the bottom layer, but the number of collected photons is also to be considered. With moderate values for other parameters, at least 10^6 collected photons are required. Optical parameters affect the figures of merit in an expected way, explained by Diffuse Optics theory. Particularly, higher absorptions, but still within reasonable limits, and lower scatterings of the top layer are favourable for better reconstruction of the bottom layer. However, overall the effect of optical parameters is not so significant. Namely, we found that the top layer absorption and scattering coefficients mostly affect the figures of merit of the top layer reconstruction, but this is not a concern, since the top layer signal is reconstructed well for all analysed values of the optical parameters. Instrument response functions with a full width at half maximum FWHM ≤ 100 ps produce no effect on the reconstruction.

For what concerns the practical point of view and application, a knowledge of optical parameters of both layers was needed for simulations, and also the exact thickness of the upper layer, while the lower layer was assumed to be thick. Each simulation takes some time to be performed, mainly because of the forward model calculation. The process of Raman scattering coefficients retrieval is very simple and quick, but has to be performed on many different wavelengths (depending on

the resolution of the system). If more advanced methods are to be developed, which could include guessing (fitting) of the optical parameters, then the computations would last much longer and, depending on the number of parameters and fineness of approaching the solution, the process could become even unfeasible. This relatively simple model and reconstruction method were proven to work on theoretical data, producing the results with a processing time of around one minute (or less, depending on the implementation), on an average PC, and with a resolution of 10^3 different wavelengths. Such obtained results are reliable for a certain range of parameters (amount of noise, width of IRF in time domain, optical and geometrical parameters).

Chapter 4

Reconstruction on Experimental Data

In the previous chapter, we tried to predict under which circumstances the reconstruction of both layers (with accent to the bottom) will be reliable. Simulations included modelling of noise, according to Poisson statistics, modelling of instrument response function, as a gaussian distribution with a certain width. Yet, there are always elements which are not modelled. Every model is a certain simplification of reality. We identified noise as the main factor that limits the performance. Its effect can be diminished by enhancing the photon collecting efficiency, or capturing signal for a longer time, since the Raman signal is weak by its nature. However, there are also geometrical limitations such as thickness of the top layer, or even worse, intrinsic material constraints such as extremely high absorptions or scatterings, which cannot be overcome in some cases.

This is all we studied by theoretical simulations. However, in practice, there are many factors which we do not even know to be present or important, unless we face them in a real experiment. The goal of this chapter is to try the method on real experimental data obtained using the Time-Correlated Single Photon Counting (TCSPC) camera and see the results. From the results we may identify problems that we could not predict with theoretical simulations. That is why this chapter and experimental part is very important. We will see that some anticipated factors in Chapter 1, such as background radiation, particularly fluorescence, are present and could affect the reconstruction of the two-layer spectra to a great extent. What is more important, we will be able to see that this concept, a model-based approach to the two-layer spectra reconstruction, actually can work on real data. The limitations and drawbacks could be fixed in future. We will stress out in this chapter what is necessary to focus on, since there will be many factors that have to be improved or optimized.

In the following sections, we are going to describe the experimental setup used to obtain data, give specifications on format of measured signals and how they can be processed, including software gating, and proceed with the reconstruction. Then, we will present the key outcome of the reconstruction and discuss the limitations and perspectives.

4.1 Description of the System Setup

In this section, the experimental equipment and setup which S. Konugolu et al. used for their experiments in Time-Domain Diffuse Raman Spectroscopy [20] is described.

To perform the temporal Raman signal acquisition, a time resolved single photon counting camera (TCSPC) was used [47]. The camera, developed in Leibniz-Institute for Neurobiology, Magdeburg, is shortly called "LINCam", or "Pico-Quant" (PQ camera), according to the company "PicoQuant Gmbh", Germany, placing it to the market. Technical details about the camera are given in [48].

Now we will summarize the details about the experimental setup published in the mentioned paper on time-domain Diffuse Raman for depth analysis of diffusive media [20]. The system setup is schematically represented in Figure 4.1. The pulsed laser, with wavelength of 532 nm was used as an excitation source. It was coupled with 100 μm-core optical fiber to the probe, shown in Figure 4.2. The probe was operating without contact with the phantoms, with ring illumination and point collection, as illustrated in Figure 4.3. An axicon lens was used to provide ring illumination, while a narrow band-pass filter at 532 nm was used to provide clean excitation. Collection optics, consisting of lenses L_1, L_2, L_3, L_4 to stop light from unwanted directions, and a long-pass filter, blocking up to 532 nm was used, to prepare only the useful signal for the spectral analysis. The probe and the spectrometer were connected with the 1 mm-core detection fiber, with numerical aperture NA = 0.39. The spectrograph ("Acton SpectraPro2150", Princeton Instruments) had a 200 μm entrance slit, $f/4$ diameter of the entrance pupil and grating of 1200 grooves per millimetre. The spectrally resolved signal was then captured by the TCSPC camera, "LINCam".

Phantoms designed to imitate a two-layer tissue were a silicon elastomer and a marble slab. The top layer, made of silicon was $d_1 = 5\,\text{mm}$ thick, with the absorption coefficient $\mu_{a1} = 0.011\,\text{mm}^{-1}$, the reduced scattering coefficient[1] $\mu'_{s1} = 1.65\,\text{mm}^{-1}$ and the refractive index $n_1 = 1.41$. The bottom layer, made of marble, $CaCO_3$,

[1]This value was officially reported in the paper [20]; however, trying the reconstruction with different optical parameters, and combining with the knowledge from the paper on FORS [13], value of $\mu'_{s1} = 1.1\,\text{mm}^{-1}$ was assumed for the model used in the reconstructions.

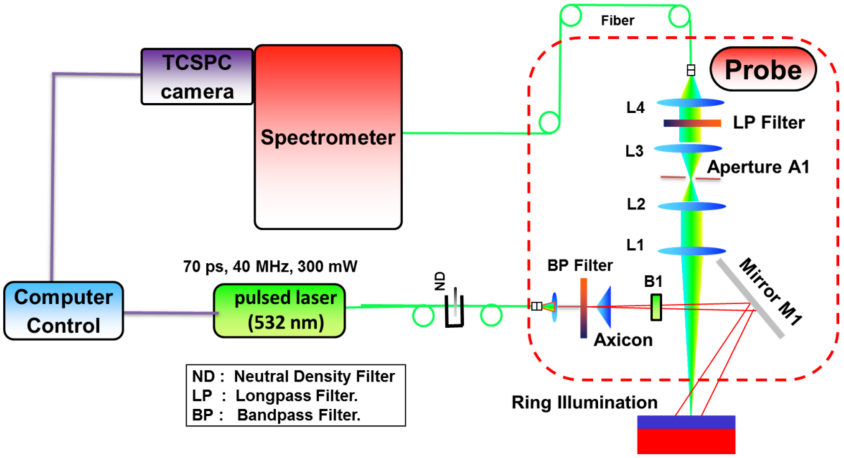

Figure 4.1: Optical chain of the experimental setup [20].

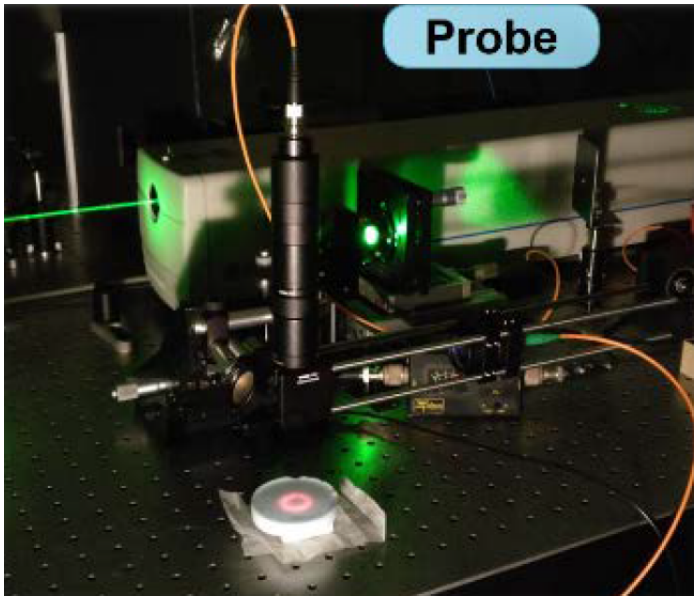

Figure 4.2: Non contact probe and the phantom [20].

aimed to simulate the bone tissue, had optical parameters: $\mu_{a2} = 0.003\,\mathrm{mm}^{-1}$ $\mu'_{s2} = 1.65\,\mathrm{mm}^{-1}$, $n_2 = 1.66$, and thickness $d_2 = 17\,\mathrm{mm}$. All the optical parameters were expressed for 532 nm wavelength, but assumed to be constant over the Raman measurement range. As said before, the ring geometry was implemented for illumination and collection. The source-detector separation, or the distance between the illumination zone and the collection point, i.e. radius of the ring was $\rho = 10\,\mathrm{mm}$.

The temporal histogram [47] of Raman photons was being acquired for 300 s.

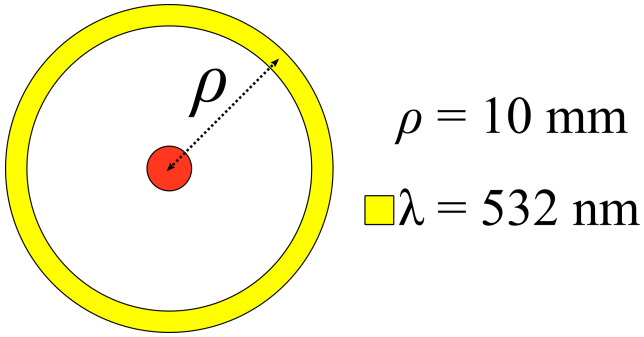

Figure 4.3: Ring illumination (yellow) and collection point (red).

The laser power was 100 mW.

We will now describe the format of raw data used for the post processing. The measurement data is structured in three-dimensional arrays. One dimension is for time, two other dimensions are for spatial positions. One of them is the axis, let us call it x, along which the spectrograph resolves the light by wavelengths, the other one, y, is orthogonal to x. Information from y-axis is aggregated, summing all the numbers of photons collected in that direction (of course, in a limited range of interest), for one given wavelength (x). Temporal histogram had steps of 11.8 ps, there was a total of 1300 time windows (each lasting 11.8 ps), and a total of 512 Raman shifts, from 369.40162 cm^{-1} to 3253.16369 cm^{-1}. Another small technical detail which has an impact on the reconstruction, time instant of 212 ps was associated with the start of the 189^{th} time window of the measurement signal.

4.2 Raw Experimental Data Analysed With Temporal Gates

The top layer, made of silicon, has its Raman emission peak at $\Delta\overline{\nu}_{m1} = 2888\,\mathrm{cm}^{-1}$. On the other hand, the peak of the bottom layer, made of marble, is at $\Delta\overline{\nu}_{m2} = 1087\,\mathrm{cm}^{-1}$. Obtained measurements, resolved in time and by wavelengths, we can prepare in any desirable form. Here we choose to show the signal components from marble (bottom layer) and silicon (top layer), as well as the background signal. That is why we plot three curves of measured Raman reflectance at (and around) three wavelengths (see Figure 4.4). The first is determined by position of the peak of silicon Raman spectrum, the second is determined by position of the peak of marble Raman spectrum. For the third curve, which should represent the background signal, originating from fluorescence, we have chosen wavelengths just before the peak of the top layer. In Figure 4.4 three curves represent these three signals. Note that silicon (top layer) signal and marble (bottom layer) signal

were obtained by subtracting background fluorescence signal from raw signals at characteristic wavelengths. Background for silicon is the one represented in Figure 4.4, while the background for marble signal was obtained in analogous way, but it is not presented in the plot. It is interesting to see that fluorescent signal appears later in time in comparison to Raman signal from the top layer, but very soon it overwhelms the useful signal. Signal from the bottom layer, arrives with a certain delay, but continues to exist for a longer time, although parallel with fluorescence processes. An important question is how to extract the most useful information from the obtained measurements. With time gating, we could eliminate fluorescence existing later in time and rely on the instantaneous nature of Raman emission. If we position time gates in the first 1.5 ns (see Figure 4.4 and the time instant when the top layer signal becomes too small), we could facilitate the reconstruction of the top layer Raman spectrum. However, to reconstruct the spectrum of the bottom layer, according to the physics of the problem, we will have more difficulties, which might be evident from the Figure 4.4.

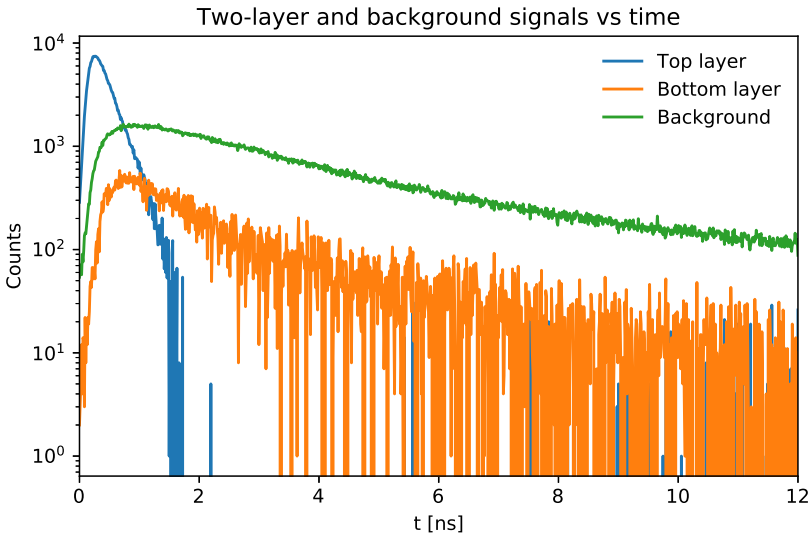

Figure 4.4: Three curves representing the signal (time resolved photon counts) obtained at and around three wavelengths (Raman shifts): 2888 cm^{-1} for the top layer (silicon), 1087 cm^{-1} for the bottom layer (marble) and 2700 cm^{-1} for the background fluorescence. The curves for the Raman signals from top and bottom layer were obtained by subtracting the background signal at neighbouring wavelengths.

Let us now see what we can obtain with time gating. The gating is chosen to exclude early photons and to cover the interval of dynamics of our problem, as it was done in [20]. Firstly, in Figure 4.5 we present the raw time gated signal. The signal

is raw because the reconstruction is not yet performed. However, we normalized the signal from 0 to 1, in order to enhance the visibility of the peaks characteristic to top and bottom layer. Top layer (silicon) peaks (around 2888 cm^{-1}) are noticeable at early gates, and gradually disappear after around 800 ps, as expected from the analysis of the Figure 4.4. The peak from the bottom layer (marble, around 1087 cm^{-1}) starts appearing from around 500 ps. Obviously, to be able to retrieve spectra of both layers, early and late gates among given twelve would be needed. We will discuss later about the selection of gates, in terms of their number and starting and ending times.

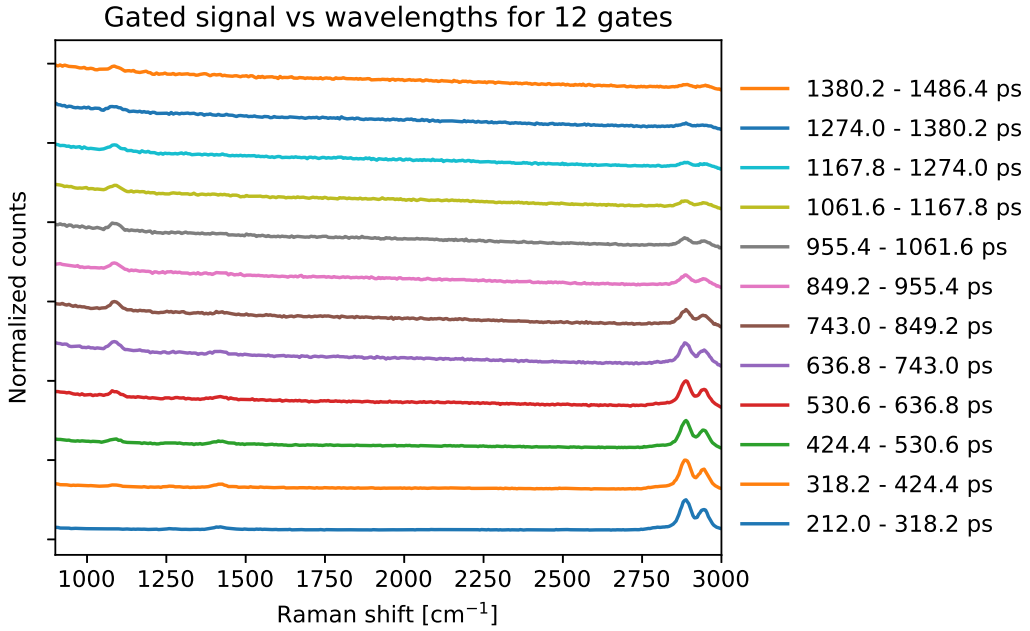

Figure 4.5: Time intervals (on the right) for 12 gates. Normalized counts signal is resolved by wavelengths. Ordinate positions are not absolute.

4.3 Reconstructed Spectra

When we apply the suggested gating, with gate intervals defined in the legend of Figure 4.5, using the forward model instructed with optical parameters: μ_{a1}, μ'_{s1}, μ_{a2}, μ'_{s2}, n_1 and n_2 and geometrical parameters: d_1, d_2 and ρ we obtain the gated sensitivity matrix $\mathbf{W_g}$. Inversion method (described in 2.5) applied on raw gated measurements (without normalization) and with the knowledge of $\mathbf{W_g}$ produces the reconstructed spectra for the two layers $S_1(\lambda)$ and $S_2(\lambda)$. The spectra for the upper and lower layer are shown in Figures 4.6 and 4.7, respectively. In the

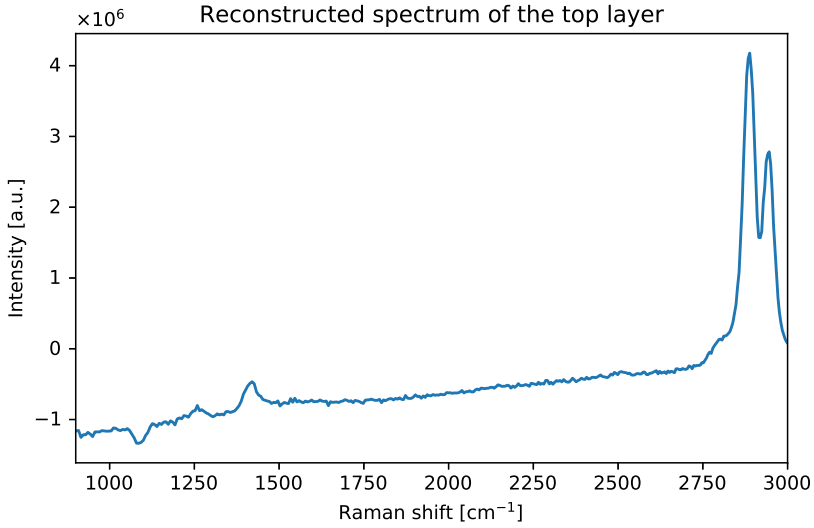

Figure 4.6: Reconstructed Raman spectrum of the top layer, directly obtained from the solution of the inverse problem.

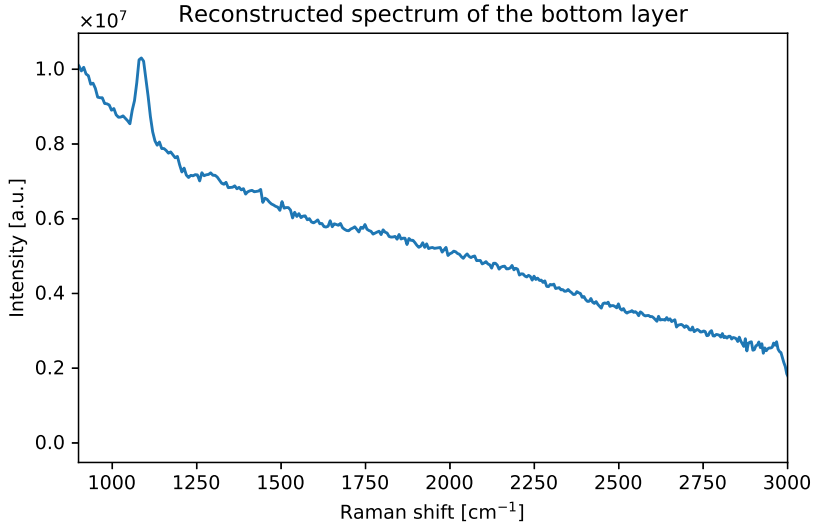

Figure 4.7: Reconstructed Raman spectrum of the bottom layer, directly obtained from the solution of the inverse problem.

reconstructed spectra, the peak of marble (1087 cm^{-1}) in the bottom layer is clearly separated from the peaks of silicon (1260 cm^{-1}, 1411 cm^{-1}, 2888 cm^{-1}, 2941 cm^{-1}) in the upper layer. We also notice that all these peaks are at the correct (inherent for marble and silicon) spectral positions. However, we can immediately observe

that these spectra cannot be purely Raman. Obviously, negative values, which appear in Figure 4.6 are physically impossible. A background signal is present. This background, then coupling between the layers as a consequence of instrument response function of the system or optical parameters mismatch[2], as well as always present noise, are the sources of some non-physical values and other values which are unexpected. In theory, it is expected to have only peaks at positions around $2888\,\mathrm{cm}^{-1}$, $2941\,\mathrm{cm}^{-1}$, possibly small peaks around $1411\,\mathrm{cm}^{-1}$ and $1260\,\mathrm{cm}^{-1}$, for the top layer, and one at $1087\,\mathrm{cm}^{-1}$ for the bottom layer, and almost straight line around zero intensity, everywhere else. To see what is the source of the problem we can correct these spectra by normalizing them from 0 to 1 and compare with the values obtained by direct Raman spectrum measurements on silicon and marble. The results are shown in Figures 4.8 and 4.9, for silicon and marble, respectively.

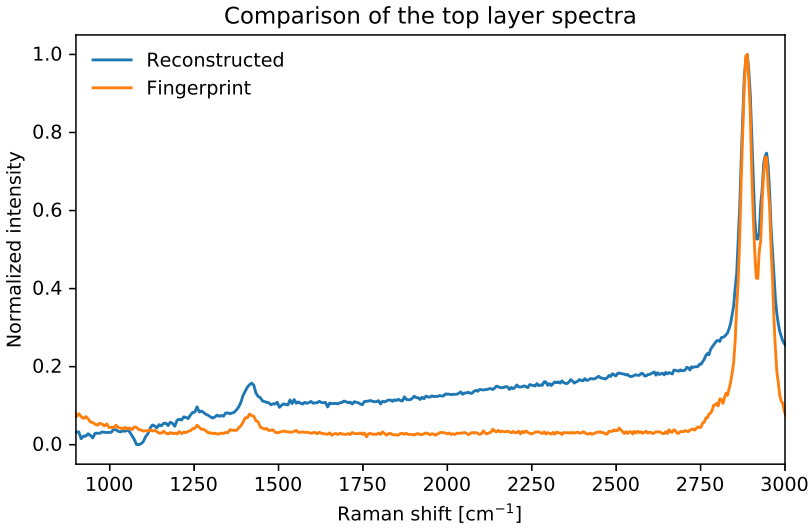

Figure 4.8: Normalized reconstructed Raman spectrum of the top layer compared to the fingerprint spectrum of silicon.

From Figure 4.9 we can conclude that the background problem is affecting both the spectra (fingerprint and reconstructed). In Figure 4.8 it can be seen that the differences between the reconstructed and fingerprint spectra of silicon (top layer) are mainly due to coupling between the layers and problematic reconstruction of the bottom layer, which is due to the background fluorescence. It is now evident that the fluorescence is highly affecting the reconstruction of Raman spectrum

[2]Besides a certain wavelength dependence of the optical parameters which is neglected, there could also be a mismatch between the actual parameters and those passed as the inputs to the forward model. Simply, a lack of precise knowledge on the parameters of the medium is probable.

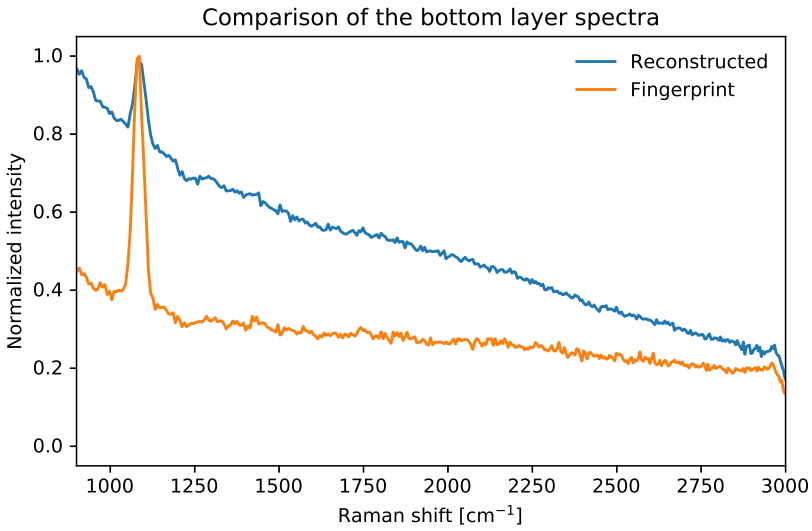

Figure 4.9: Normalized reconstructed Raman spectrum of the bottom layer compared to the fingerprint spectrum of marble.

from depth. Fluorescent signal is continuous over wavelengths and quite strong. It is because even fluorescence generated from top layer may appear late in time as if it was coming from depth, but much stronger since the source of emission is much closer to the detector than Raman emitters from the bottom layer are. One is sure, peak positions are correctly identified, while the overall spectrum reconstruction could be improved if we succeed in rejecting the background fluorescence.

4.4 Problem of Background Removal

In this section, we will try some methods to improve the quality of reconstruction, regarding the question of background fluorescence removal. One may think to model the fluorescence and include it in the overall forward model, but that would require more parameters and the model would become much more complicated, which is not of interest for us now. Here we will focus on spectra already obtained in Section 4.3 and try to estimate the contribution of the fluorescence to the overall spectrum or signal.

Firstly, we try a polynomial fit, which should estimate the background by fitting the polynomial of the chosen order through the selected points. We can call these points "stable" (according to the value of the first derivative of the spectrum), because we select only those points that are in a so-called "flat region" (smaller absolute values of the first derivative), not in a "dynamical" one, where the peaks are expected. The "stable points" are selected according to the absolute value of

the first derivative of the spectrum. If the derivative of the spectrum at the given point as well as at a few (in this case 3) neighbouring points (in both directions, 3 from left and 3 from right) is in certain range (by absolute value less than 40% of maximum absolute value of derivative on the considered interval of wavelengths), then the point is selected. Third order polynomial fit was chosen. The values of 40% and 3 neighbouring points per direction are free parameters. They can be optimized. The results of this algorithm are presented in Figures 4.10 and 4.11.

After subtraction of such estimated fluorescence background spectrum, the reconstructed spectra are shown in Figures 4.12 and 4.13.

From Figures 4.12 and 4.13 we see that the peaks clearly stand out. Reconstructed spectrum of the upper layer (silicon) could be even considered good, with one problematic negative component at the wavelength of the peak of the lower layer, though of very small amplitude. On the other hand, reconstructed spectrum of the lower layer is much more "noisy", however with good reconstruction of the marble inherent peak at $1087\,\mathrm{cm}^{-1}$. For silicon, besides the main peaks present at $2888\,\mathrm{cm}^{-1}$ and $2941\,\mathrm{cm}^{-1}$, appearance of smaller peaks at Raman shifts $1411\,\mathrm{cm}^{-1}$ and $1260\,\mathrm{cm}^{-1}$ is also characteristic [20].

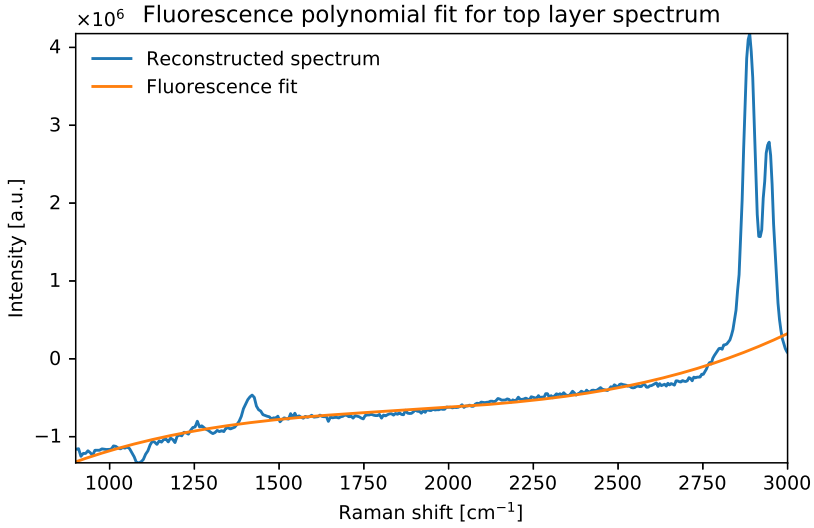

Figure 4.10: Third order polynomial estimation of the background fluorescence spectrum for the top layer. Blue line represents the originally retrieved spectrum (Raman with background), orange line represents the fit for the background.

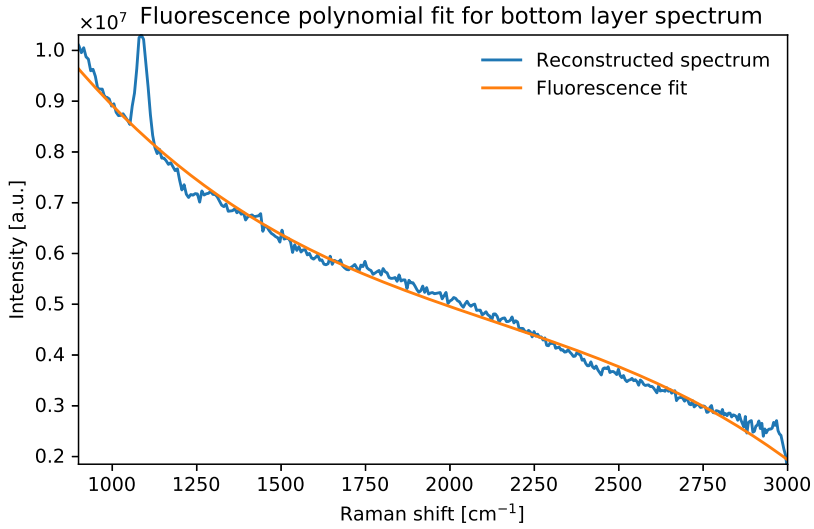

Figure 4.11: Third order polynomial estimation of the background fluorescence spectrum for the bottom layer. Blue line represents the originally retrieved spectrum (Raman with background), orange line represents the fit for the background.

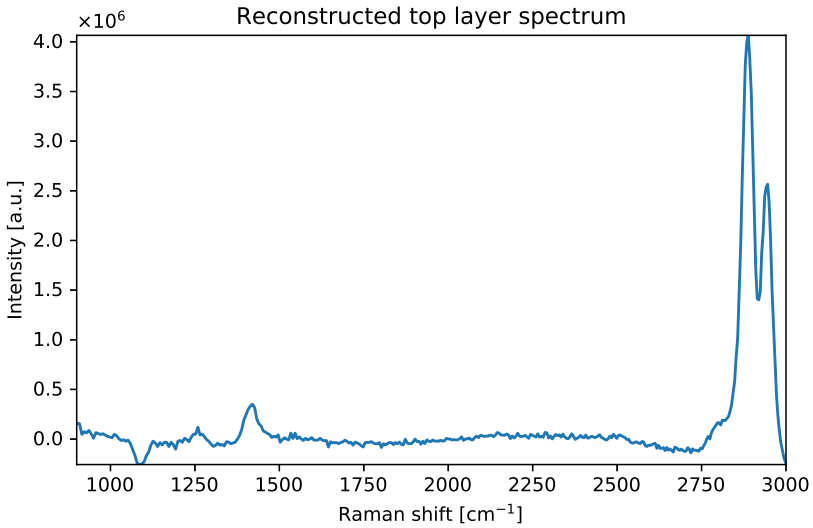

Figure 4.12: Reconstructed spectrum of the first layer, obtained by subtracting the third order polynomial estimation of the fluorescence background from the originally retrieved (Raman with background) spectrum of the top layer.

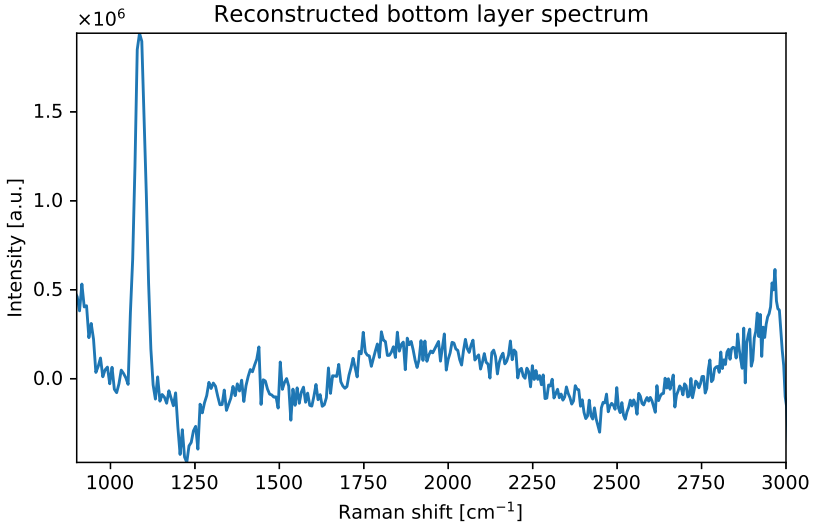

Figure 4.13: Reconstructed spectrum of the bottom layer, obtained by subtracting the third order polynomial estimation of the fluorescence background from the originally retrieved (Raman with background) spectrum of the bottom layer.

Another method we could propose is based on a cubic spline interpolation of the background through the selected points. The points are selected if they meet the following criteria: 1) first derivative at that point is changing sign from negative to positive (practically, local minimum points) [49]; and 2) the change is not too abrupt (in some chosen range, (10-20)% of the maximum of absolute value of the spectrum first derivative). The results of this method are shown in Figures 4.14 and 4.15.

Reconstructed spectra, after subtraction of such estimated background, are represented in Figures 4.16 and 4.17.

With this method, reconstruction of top and bottom layer is even closer to real spectra of silicon and marble. For what regards the top layer, there are no negative peaks, but the height of the peak at $2888\,\mathrm{cm}^{-1}$ is slightly lower than in the previous case. The bottom layer is reconstructed much better in comparison to the previous method. There are some parts which are "noisy", but the amplitude is so low, that it can be easily neglected. Main features, peak height and position are reconstructed well.

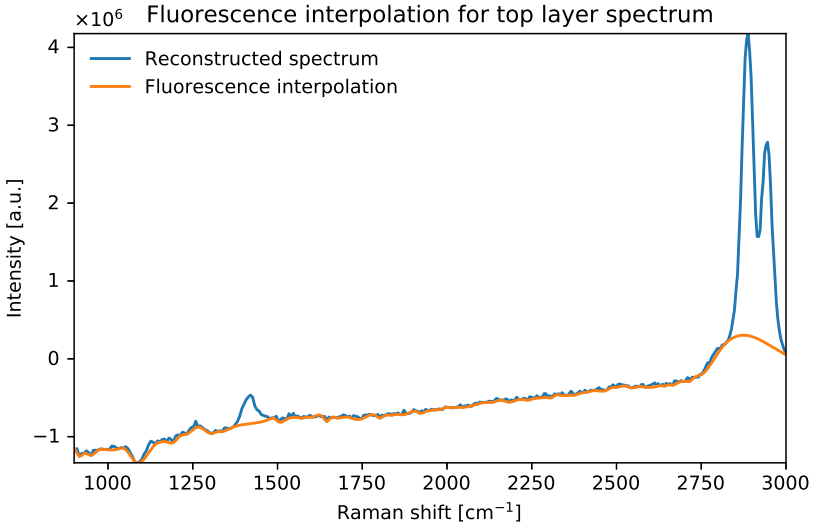

Figure 4.14: Cubic spline interpolation of the background fluorescence spectrum for the top layer. Blue line represents the originally retrieved spectrum (Raman with background), orange line represents the curve for the background.

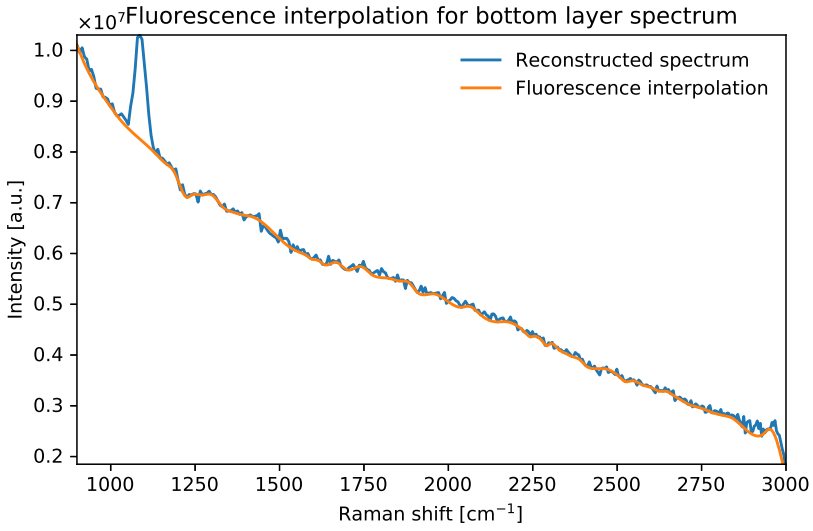

Figure 4.15: Cubic spline interpolation of the background fluorescence spectrum for the bottom layer. Blue line represents the originally retrieved spectrum (Raman with background), orange line represents the curve for the background.

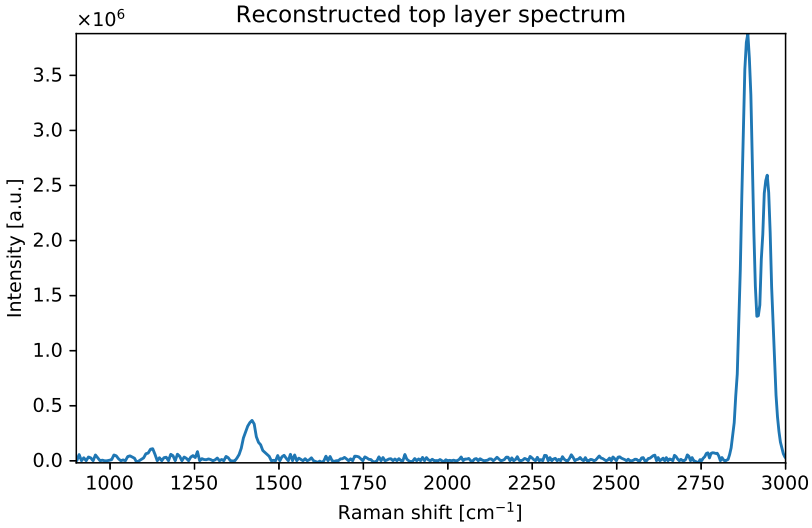

Figure 4.16: Reconstructed spectrum of the first layer, obtained by subtracting the cubic spline interpolation of the fluorescence background from the originally retrieved (Raman with background) spectrum of the top layer.

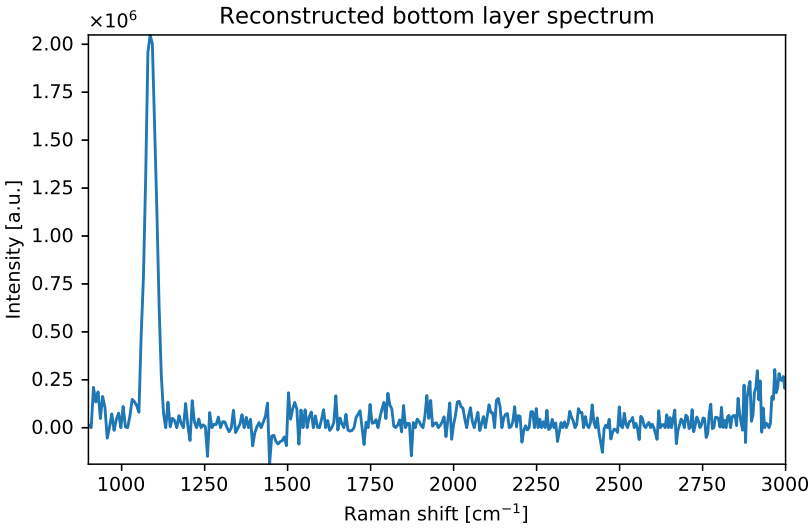

Figure 4.17: Reconstructed spectrum of the bottom layer, obtained by subtracting the cubic spline interpolation of the fluorescence background from the originally retrieved (Raman with background) spectrum of the bottom layer.

4.5 Open Issues

After discussing the results of the reconstruction on real experimental data, we may now focus on practical issues that are to be tackled. Besides the fluorescence background issue that we faced in the previous section, there is also a question of determining optimal gates, then the anticipated problem of optical properties which are wavelength dependent in practice, but that dependence is not included in the model we have used.

4.5.1 Fluorescence Background

We have already seen the problem of the background and proposed some methods to subtract it, but anyway, it affects the measured signal and afterward reconstructed spectra, whenever there is a phenomenon of fluorescence. We could further discuss about different methods for the background removal. However, if we completely change the direction, and instead of thinking how to remove the background which is already overwhelming the useful signal, we start thinking about how to avoid the fluorescence, then we may conclude that different experimental setups could diminish its impact. Fluorescence is much more intense when the excitation frequencies are high (i.e. wavelengths are low). With this experimental setup, described in Section 4.1, excitation laser had wavelength of 532 nm which is quite short, i.e. at this wavelength, great fluorescence contribution is expected. Fluorescence is significantly weaker at higher excitation wavelengths. Typically, in range (785-1064) nm, fluorescence-to-Raman signal ratio is often very small or negligible [50]. This should be considered, in order to obtain cleaner Raman spectra by the reconstruction methods proposed. Another possibility is to include the fluorescence term in the forward model. This could make the model more complete, however more complex at the same time, also it would require more parameters.

4.5.2 Optimal Selection of Gates

Besides the time gates defined in Section 4.2 and later applied for the reconstruction in 4.3, we tried a few other possibilities. Moving gates to later times affects the reconstruction of the top layer. Time shift equal to the duration of six gates completely distorts the reconstruction of the top layer spectrum. If the top layer is not reconstructed well, also the bottom layer reconstruction will be wrong. Conversely, moving gates to earlier times, only one gate (106.2 ps) earlier, would lead to worse reconstruction of the bottom layer. In this case, bottom layer would contain more intense components of the top layer. Many other tries with similar number of gates, or even double or half, resulted in similar reconstructions of the two layer spectra. To summarize, the time gating proposed in Section 4.2 seems

close to optimal, but it can be stated just for this specific experimental setup and obtained data set. It is always advisory to be careful when choosing number and positions of time gates, if gating is done by software, in order not to lose the information.

4.5.3 Optical Properties

In reality, optical parameters, absorption and scattering of the first and second layer, μ_{a1}, μ'_{s1}, μ_{a2}, μ'_{s2}, are wavelength dependent. To obtain a more realistic model, one should also take that into account precisely and calculate the sensitivity matrix at each wavelength. Here we have two main issues. The first, in real experiments it is questionable if we can precisely know absorption and scattering coefficients. Every mistake in modelling of the absorption and scattering will be projected directly to the reconstruction results. Peak height is very sensitive to the values of absorption and scattering coefficients. Another problem concerns the modelling. Even if we exactly know all the optical parameters at both wavelengths (source emission and Raman emission), it is not clear which value should be taken for the absorption and scattering coefficients. One may think to assume half of photon pathlength at each of the two wavelengths, and therefore a mean value for the optical properties at the excitation and Raman emission wavelength, but it has to be argued[3]. Moreover, strictly speaking, the heuristic model is only valid when optical parameters, absorption and scattering are the same on both wavelengths [39].

4.6 Conclusion

In this chapter we have tested the proposed reconstruction method on real measurements. With the messages taken from the simulations performed in Chapter 3, we could have expected to get an acceptable reconstruction in terms of depth sensitivity (thickness of the upper layer was $d_1 = 5\,\text{mm}$, which is quite promising), and optical parameters, since they, as well, were not a limiting factor in these measurements. Also the number of photon counts and the IRF were in the limits of safe operation of the method analyzed in Chapter 3. The obtained results showed that the reconstructed spectra of the two layers were well separated. The inherent Raman peaks of the two layers could have been recognized with its expected relative intensity and correct spectral position. However, the overwhelming background

[3] A more rigorous approach would be to derive the Diffusion Equation for the two layers following the same method for the homogeneous solution of Diffuse Raman [39], thus adopting different optical parameters at the excitation and Raman emission wavelength.

fluorescence radiation was present and affected the raw reconstruction results, i.e. those obtained just with application of the theory from Chapter 2.

For this reason, we discussed the possibilities for the background removal and proposed some relatively simple and fast software methods. Upon their application, the obtained results appeared to be closer to the real Raman spectra of silicon and marble, without fluorescence, but not completely correct. We concluded that the background removal was needed, but we should also be aware not to overestimate the fluorescence contribution. Due to the long decay times, fluorescence presents much bigger problem for the reconstruction of the bottom layer spectrum, as it happened to be the case also here. However, with the proposed methods for the background removal, inherent peaks could stand out easily and with intensities depending on the parameters of the model. Proper time gating may help in fluorescence suppression. However, as it was the case with the experimental data set we had here to analyze, if the measurements are done with very short excitation wavelengths, the fluorescence contribution is expected to be high. Moving to longer wavelengths, the Raman-to-fluorescence signal ratio is expected to be increased.

If the parameters, from geometrical to optical are correct, we have a reason to trust the proposed reconstruction method. However, where we should be careful is the limitation of the heuristic model. In practice, optical parameters are wavelength dependent, therefore, strictly speaking, heuristic approach will not for granted produce reliable results. We neglected this fact while retrieving the unknown Raman spectra. What can be done is, taking also this dependence into account, trying to make a model even closer to reality. The truth is that we may never have formal guarantees the method is correct, since the formal requests could not be satisfied in realistic case, but, as long as we obtain satisfactory results, we may have reasons to use this method and try to make it even better with taking into account other effects.

To summarize, the goal of this chapter was to obtain the reconstructed spectra of the two layers, starting from the real experimental data, which was achieved. The spectra were affected by the fluorescence, which is assumed to be the specificity of the measurement at relatively short wavelength. Fluorescence may be further suppressed even in software, as we suggested. Finally, satisfactory, but not excellent results were obtained. The conclusion is that this method can work with experimental data, but it is highly desirable to have data prepared in a better way. Moreover, the method itself has a lot of potential to be improved, starting from the optical parameters dependence on wavelength, then trying to find the optimal software gating, or even by including fluorescence in the theoretical model.

Since the method was validated on real experimental data, which was the final goal of the thesis work, we can conclude this chapter by stating that the proposed concept for the two-layer reconstruction of Raman spectra in diffusive media was proven for the first time.

Chapter 5

Conclusions and Perspectives

The aim of this thesis work was to make a step forward in developing methods for the reconstruction of the Raman spectra in heterogeneous diffusive media, particularly two-layered case, by time domain approaches. Time domain approach due to depth sensitivity in diffusive media showed a great potential for application in many different fields, among which clinical diagnostics is, especially because of the great chemical specificity of Raman Spectroscopy. So far, the time gating of collected photons was applied, however the information obtained has never been used for a rigorous reconstruction, but rather in a qualitative way. In this thesis work, a new application of Diffuse Raman photon propagation modelling in time domain, combined with a generalization of a heuristic approach from homogeneous to the two-layer media was presented. According to this heuristic Diffuse Raman model for the two-layer media, a complete forward problem of a cylindrical two-layer geometry was solved for Raman reflectance. This enabled the calculation of sensitivity matrices, which establish a linear relation between the measurements and Raman spectra of the two layers. With that information, the inverse problem, i.e. the retrieval of unknown Raman spectra of the two layers, when Raman reflectance measurements are known, can be solved directly and rigorously. The inverse problem is linear and the solution is computationally cheap. All these methods have been implemented in software. The software was used to run simulations and reconstruct the spectra. Spectra were reconstructed both from simulated measurements and from real experimental data set. Thus, a rigorous, model-based reconstruction of two-layer Raman spectra was demonstrated for the first time.

We ran simulations on different scenarios, and as a result, obtained the figures of merit, which quantitatively evaluated the quality of reconstruction. These figures

of merit: relative error of the peak height reconstruction, contrast-to-noise ratio and suppression factor of one layer's components in the reconstructed spectrum of the other layer, depend on various parameters, including geometrical (thickness of the layer, source-detector distance), optical (absorption and scattering coefficients) and more experimental (total number of photon counts and instrument response function in the time domain). Analyzing the figures of merit, we obtained expected theoretical limits at which the reconstruction of both layer spectra is reliable and to which extent faithful. Main limiting factors are the thickness of the top layer, which should be no larger than 10 mm, as well as the total number of collected photons, which should be at least 10^6, in order to obtain a reliable reconstruction. We must be also conscious about the limitations of the model itself. The model based on the heuristic approach, yet simple, relies on the assumption of the equality of the optical parameters on all wavelengths.

Finally, the proposed approach was tested on real measurements, on the data set obtained by S. Konugolu et al, by the application of a time-correlated single photon counting camera [20]. The reconstruction results showed us the potential of further development and application of this new concept. The reconstruction was successful in terms of layer separation. Inherent peaks of a two-layer phantom (silicon and marble) were correctly retrieved, in terms of spectral position and relative intensity. The novel concept, in which the depth sensitivity is rigorously modelled, was proven to work on experimental data. This proof of concept should serve as a cornerstone for further research on model-based reconstruction of multi-layer Raman spectra in diffusive media. Therefore, in the following paragraphs, we would like to summarize the main limitations and potential directions to follow in order to improve this concept.

The impact of fluorescence background signal on experimental data was noticeable, we suggested a few particular software solutions to reject the fluorescence from the reconstructed spectra. For the final refinement of the reconstructed spectra, there is still a lot of room for improvement. Background and noise removal are to be optimized, to make the spectra smoother and without non-existing peaks. More interesting approach would be to try to include the fluorescence phenomenon in the theoretical model. This may complicate the methods, but in perspective, it is the direction to think in. Furthermore, a study on optimal selection of time gates is recommended.

One weak point of the current model is the requirement for the absorption and scattering coefficients of the two layers. In practical applications they might not be available, or could be, but not very precisely, and not at all wavelengths. One may think to estimate also these parameters, but that would mean in practice increment in number of unknowns from 2 to 6 at each wavelength, though some models for the wavelength dependence of absorption and scattering could be assumed. However, more complex model considering absorption and scattering coefficients as unknowns

would probably become computationally unfeasible in reasonable amount of time. Therefore, although with obvious roughness and drawbacks because of the heuristic approximation, the proposed model and the reconstruction method is very efficient in computational sense, due to its linearity and simplicity.

The perspective of this model, in a short term could be its generality, or capability to be generalized easily. This means that, with the same approach, Spatially Offset Raman Spectroscopy (SORS) and Frequency Offset Raman Spectroscopy (FORS) problems could be treated by developing the specific sensitivity matrices for each scenario, and retrieving the spectra in the same way. Instead of time gates, one would exploit spatial or spectral differentiation, but everything is analogous to the concept we proposed, and easy to implement, with the difference that instead of time resolved solutions, one should look for continuous-wave solutions.

In perspective, thoroughly post processed spectra could be analyzed with methods from the field of statistical pattern recognition or artificial neural networks to recognize the specific molecules. These methods could be even directly used to extract Raman features from raw spectra, just after the inversion method which could be a shortcut to the final goal. The furthest vision in this field could be to use neural networks to find the solution, avoiding the application of the inversion method, just considering the forward model and the measurements, and assuming different spectra. The forward model could be updated during the process of iterations in this case, opening the possibility to find the exact values for the thicknesses and optical parameters, since in practice there might be an error in input parameters due to the model ignorance. All eventual implementations in this direction would strongly rely on the feasibility of these artificial intelligence methods.

Bibliography

[1] Fabrizio Martelli, Samuele Del Bianco, Andrea Ismaelli, and Giovanni Zaccanti. *Light Propagation through Biological Tissue and Other Diffusive Media - Theory, Solutions and Software*. Bellingham, Washington, USA: SPIE, 2010. ISBN: 978-0-8194-7658-6 (cit. on pp. 2, 17–19, 29, 37, 45).

[2] Alessandro Torricelli, Antonio Pifferi, Lorenzo Spinelli, Rinaldo Cubeddu, Fabrizio Martelli, Samuele Del Bianco, and Giovanni Zaccanti. «Time-resolved reflectance at null source-detector separation: Improving contrast and resolution in diffuse optical imaging». In: *Physical Review Letters* 95.7 (2005), pp. 2–5. ISSN: 00319007. DOI: 10.1103/PhysRevLett.95.078101 (cit. on p. 4).

[3] Antonio Pifferi et al. «Time-resolved diffuse reflectance using small source-detector separation and fast single-photon gating». In: *Physical Review Letters* 100.13 (2008), pp. 1–4. ISSN: 00319007. DOI: 10.1103/PhysRevLett.100.138101 (cit. on p. 4).

[4] C. V. Raman and K. S. Krishnan. «A new type of secondary radiation». In: *Nature* 121.3048 (1928), pp. 501–502. ISSN: 00280836. DOI: 10.1038/121501c0 (cit. on p. 5).

[5] Pavel Matousek and Nicholas Stone. «Development of deep subsurface Raman spectroscopy for medical diagnosis and disease monitoring». In: *Chemical Society Reviews* 45.7 (2016), pp. 1794–1802. ISSN: 14604744. DOI: 10.1039/c5cs00466g (cit. on pp. 7, 8, 13).

[6] P. Matousek, I. P. Clark, E. R. C. Draper, M. D. Morris, A. E. Goodship, N. Everall, M. Towrie, W. F. Finney, and A. W. Parker. «Subsurface Probing in Diffusely Scattering Media Using Spatially Offset Raman Spectroscopy». In: *Appl. Spectrosc.* 59.4 (Apr. 2005), pp. 393–400. URL: http://as.osa.org/abstract.cfm?URI=as-59-4-393 (cit. on p. 7).

[7] P. Matousek, C. Conti, M. Realini, and C. Colombo. «Micro-scale spatially offset Raman spectroscopy for non-invasive subsurface analysis of turbid materials». In: *Analyst* 141 (3 2016), pp. 731–739. DOI: 10.1039/C5AN02129D. URL: http://dx.doi.org/10.1039/C5AN02129D (cit. on p. 8).

[8] Dana Cialla, Anne März, René Böhme, Frank Theil, Karina Weber, Michael Schmitt, and Jürgen Popp. «Surface-enhanced Raman spectroscopy (SERS): Progress and trends». In: *Analytical and Bioanalytical Chemistry* 403.1 (2012), pp. 27–54. ISSN: 16182642. DOI: 10.1007/s00216-011-5631-x (cit. on p. 8).

[9] Isaac Pence and Anita Mahadevan-Jansen. «Clinical instrumentation and applications of Raman spectroscopy». In: *Chemical Society Reviews* 45.7 (2016), pp. 1958–1979. ISSN: 14604744. DOI: 10.1039/c5cs00581g. URL: http://dx.doi.org/10.1039/C5CS00581G (cit. on p. 8).

[10] B. Schrader and G. Bergmann. «Die Intensität des Ramanspektrums polykristalliner Substanzen». In: *Anal. Chem.* 225 (1967), pp. 230–247. DOI: 10.1007/BF00983673 (cit. on p. 8).

[11] Sara Mosca, Priyanka Dey, Tanveer A. Tabish, Francesca Palombo, Nicholas Stone, and Pavel Matousek. «Spatially Offset and Transmission Raman Spectroscopy for Determination of Depth of Inclusion in Turbid Matrix». In: *Analytical Chemistry* 91.14 (2019), pp. 8994–9000. ISSN: 15206882. DOI: 10.1021/acs.analchem.9b01222 (cit. on p. 8).

[12] Fabrizio Martelli, Tiziano Binzoni, Antonio Pifferi, Lorenzo Spinelli, Andrea Farina, and Alessandro Torricelli. «There ' s plenty of light at the bottom : statistics of photon penetration depth in random media». In: *Scientific Reports* 6 (2016), pp. 1–14. DOI: 10.1038/srep27057 (cit. on p. 9).

[13] Sanathana Konugolu Venkata Sekar, Sara Mosca, Andrea Farina, Fabrizio Martelli, Paola Taroni, Gianluca Valentini, Rinaldo Cubbedu, and Antonio Pifferi. «Frequency Offset Raman Spectroscopy (FORS) for depth probing of diffusive media». In: *Optics Express* 25.5 (2017), pp. 4585–4597. DOI: 10.1364/OTS.2018.OTu4D.1 (cit. on pp. 9, 80).

[14] P. Matousek, N. Everall, M. Towrie, and A. W. Parker. «Depth profiling in diffusely scattering media using Raman spectroscopy and picosecond Kerr gating». In: *Applied Spectroscopy* 59.2 (2005), pp. 200–205. ISSN: 00037028. DOI: 10.1366/0003702053085115 (cit. on p. 10).

[15] P. Matousek, M. Towrie, A. Stanley, and A. W. Parker. «Efficient rejection of fluorescence from Raman spectra using picosecond Kerr gating». In: *Applied Spectroscopy* 53.12 (1999), pp. 1485–1489. ISSN: 00037028. DOI: 10.1366/0003702991945993 (cit. on p. 10).

[16] Emad L. Izake, Biju Cletus, William Olds, Shankaran Sundarajoo, Peter M. Fredericks, and Esa Jaatinen. «Deep Raman spectroscopy for the non-invasive standoff detection of concealed chemical threat agents». In: *Talanta* 94 (2012), pp. 342–347. ISSN: 00399140. DOI: 10.1016/j.talanta.2012.03.053. URL: http://dx.doi.org/10.1016/j.talanta.2012.03.053 (cit. on pp. 11, 14).

[17] Biju Cletus, William Olds, Emad L. Izake, Shankaran Sundarajoo, Peter M. Fredericks, and Esa Jaatinen. «Combined time- and space-resolved Raman spectrometer for the non-invasive depth profiling of chemical hazards». In: *Analytical and Bioanalytical Chemistry* 403.1 (2012), pp. 255–263. ISSN: 16182642. DOI: 10.1007/s00216-012-5792-2 (cit. on pp. 11, 14).

[18] Jan Hein Hooijschuur, Ingeborg E. Iping Petterson, Gareth R. Davies, Cees Gooijer, and Freek Ariese. «Time resolved Raman spectroscopy for depth analysis of multi-layered mineral samples». In: *Journal of Raman Spectroscopy* 44.11 (2013), pp. 1540–1547. ISSN: 03770486. DOI: 10.1002/jrs.4369 (cit. on p. 11).

[19] Dax Kepshire, Niculae Mincu, Michael Hutchins, Josiah Gruber, Hamid Dehghani, Justin Hypnarowski, Frederic Leblond, Mario Khayat, and Brian W. Pogue. «A microcomputed tomography guided fluorescence tomography system for small animal molecular imaging». In: *Review of Scientific Instruments* 80.4 (2009), p. 043701. DOI: 10.1063/1.3109903. URL: https://doi.org/10.1063/1.3109903 (cit. on p. 11).

[20] S. Konugolu Venkata Sekar et al. «Time domain diffuse Raman spectrometer based on a TCSPC camera for the depth analysis of diffusive media». In: *Optics Letters* 43.9 (2018), p. 2134. ISSN: 0146-9592. DOI: 10.1364/ol.43.002134 (cit. on pp. 11, 12, 15, 80, 81, 83, 88, 98).

[21] Pascal Berto, Camille Scotté, Frédéric Galland, Hervè Rigneault, and Hilton B. de Aguiar. «Programmable single-pixel-based broadband stimulated Raman scattering». In: *Optics Letters* 42.9 (2017), pp. 1696–1699. ISSN: 0146-9592. DOI: 10.1364/ol.42.001696 (cit. on p. 12).

[22] M. Lacerenza, S. K. V. Sekar, A. Farina, G. Valentini, C. D'Andrea, and A. Pifferi. «Compressive sensing time-domain Raman spectrometer for depth sensing of diffusive media». In: *Diffuse Optical Spectroscopy and Imaging VII*. Ed. by Hamid Dehghani and Heidrun Wabnitz. Vol. 11074. International Society for Optics and Photonics. SPIE, 2019, pp. 291–293. DOI: 10.1117/12.2526673. URL: https://doi.org/10.1117/12.2526673 (cit. on p. 12).

[23] Matthew D. Keller, Shovan K. Majumder, and Anita Mahadevan-Jansen. «Spatially offset Raman spectroscopy of layered soft tissues». In: *Opt. Lett.* 34.7 (Apr. 2009), pp. 926–928. DOI: 10.1364/OL.34.000926. URL: http://ol.osa.org/abstract.cfm?URI=ol-34-7-926 (cit. on p. 13).

[24] Matthew V. Schulmerich, Jacqueline H. Cole, Kathryn A. Dooley, Michael D. Morris, Jaclynn M. Kreider, Steven A. Goldstein, Subhadra Srinivasan, and Brian W. Pogue. «Noninvasive Raman tomographic imaging of canine bone tissue». In: *Journal of Biomedical Optics* 13.2 (2008), pp. 020506-1–020506-3. ISSN: 10833668. DOI: 10.1117/1.2904940 (cit. on p. 13).

[25] Eliana Cordero, Ines Latka, Christian Matthäus, Iwan W. Schie, and Jürgen Popp. «In-vivo Raman spectroscopy: from basics to applications». In: *Journal of Biomedical Optics* 23.7 (2018), pp. 1–23. DOI: 10.1117/1.JBO.23.7.071210. URL: https://doi.org/10.1117/1.JBO.23.7.071210 (cit. on p. 13).

[26] Fay Nicolson, Moritz F. Kircher, Nick Stone, and Pavel Matousek. «Spatially offset Raman spectroscopy for biomedical applications». In: *Chem. Soc. Rev.* (2020), pp. -. DOI: 10.1039/D0CS00855A. URL: http://dx.doi.org/10.1039/D0CS00855A (cit. on p. 13).

[27] Nikki Kuhar, Sanchita Sil, Taru Verma, and Siva Umapathy. «Challenges in application of Raman spectroscopy to biology and materials». In: *RSC Adv.* 8 (46 2018), pp. 25888–25908. DOI: 10.1039/C8RA04491K. URL: http://dx.doi.org/10.1039/C8RA04491K (cit. on p. 13).

[28] Pavel Matousek, Claudia Conti, Chiara Colombo, and Marco Realini. «Monte Carlo simulations of subsurface analysis of painted layers in micro-scale spatially offset Raman spectroscopy». In: *Applied Spectroscopy* 69.9 (2015), pp. 1091–1095. ISSN: 19433530. DOI: 10.1366/15-07894 (cit. on pp. 13, 18).

[29] C. Conti, A. Botteon, C. Colombo, D. Pinna, M. Realini, and P. Matousek. «Advances in Raman spectroscopy for the non-destructive subsurface analysis of artworks: Micro-SORS». In: *Journal of Cultural Heritage* 43 (2020), pp. 319–328. ISSN: 1296-2074. DOI: https://doi.org/10.1016/j.culher.2019.12.003. URL: http://www.sciencedirect.com/science/article/pii/S1296207419305734 (cit. on p. 13).

[30] Marco Realini, Alessandra Botteon, Claudia Conti, Chiara Colombo, and Pavel Matousek. «Development of portable defocusing micro-scale spatially offset Raman spectroscopy». In: *Analyst* 141 (10 2016), pp. 3012–3019. DOI: 10.1039/C6AN00413J. URL: http://dx.doi.org/10.1039/C6AN00413J (cit. on p. 13).

[31] M. Realini, C. Conti, Alessandra Botteon, Chiara Colombo, and Pavel Matousek. «Development of a full micro-scale spatially offset Raman spectroscopy prototype as a portable analytical tool». In: *The Analyst* 142 (Dec. 2016). DOI: 10.1039/c6an02470j (cit. on p. 13).

[32] C Eliasson, N Macleod, and Pavel Matousek. «Noninvasive Detection of Concealed Liquid Explosives Using Raman Spectroscopy». In: *Analytical chemistry* 79 (Dec. 2007), pp. 8185–9. DOI: 10.1021/ac071383n (cit. on p. 14).

[33] Pavel Matousek. «Spatially offset Raman spectroscopy for non-invasive analysis of turbid samples». In: *TrAC Trends in Analytical Chemistry* 103 (2018), pp. 209–214. ISSN: 0165-9936. DOI: https://doi.org/10.1016/j.trac.2018.04.002. URL: http://www.sciencedirect.com/science/article/pii/S0165993617304466 (cit. on p. 14).

[34] Charlotte Eliasson and Pavel Matousek. «Noninvasive Authentication of Pharmaceutical Products through Packaging Using Spatially Offset Raman Spectroscopy». In: *Analytical chemistry* 79 (Mar. 2007), pp. 1696–701. DOI: 10.1021/ac062223z (cit. on p. 14).

[35] William Olds, Shankaran Sundarajoo, Mark Selby, Biju Cletus, Peter Fredericks, and Emad Izake. «Noninvasive, Quantitative Analysis of Drug Mixtures in Containers Using Spatially Offset Raman Spectroscopy (SORS) and Multivariate Statistical Analysis». In: *Applied spectroscopy* 66 (May 2012), pp. 530–7. DOI: 10.1366/11-06554 (cit. on p. 14).

[36] Julia Griffen, Andrew Owen, Darren Andrews, and Pavel Matousek. «Recent Advances in Pharmaceutical Analysis Using Transmission Raman Spectroscopy». In: *Spectroscopy* 32 (Apr. 2017), pp. 37–43 (cit. on p. 14).

[37] Jianwei Qin, Kuanglin Chao, and Moon S Kim. «Postharvest Biology and Technology Nondestructive evaluation of internal maturity of tomatoes using spatially offset Raman spectroscopy». In: *Postharvest Biology and Technology* 71 (2012), pp. 21–31. ISSN: 0925-5214. DOI: 10.1016/j.postharvbio.2012.04.008. URL: http://dx.doi.org/10.1016/j.postharvbio.2012.04.008 (cit. on p. 14).

[38] David Ellis, Rebecca Eccles, Yun Xu, Julia Griffen, Howbeer Muhamadali, Pavel Matousek, Ian Goodall, and Royston Goodacre. «Through-container, extremely low concentration detection of multiple chemical markers of counterfeit alcohol using a handheld SORS device». In: *Scientific Reports* 7 (Dec. 2017). DOI: 10.1038/s41598-017-12263-0 (cit. on p. 14).

[39] Fabrizio Martelli, Tiziano Binzoni, Sanathana Konugolu Venkata Sekar, Andrea Farina, Stefano Cavalieri, and Antonio Pifferi. «Time-domain Raman analytical forward solvers». In: *Optics Express* 24.18 (2016), pp. 20382–20399. ISSN: 1094-4087. DOI: 10.1364/oe.24.020382 (cit. on pp. 17, 18, 30, 31, 33, 34, 37, 95).

[40] Fabrizio Martelli. Personal communication, Unpublished material. 2020 (cit. on pp. 17, 37).

[41] G. F. Roach. *Green's Functions: Introductory Theory with Applications*. London: Van Nostrand Reinhold Company, 1970 (cit. on p. 23).

[42] Michael S. Patterson, B. Chance, and B. C. Wilson. «Time resolved reflectance and transmittance for the noninvasive measurement of tissue optical properties». In: *Appl. Opt.* 28.12 (June 1989), pp. 2331–2336. DOI: 10.1364/AO.28.002331. URL: http://ao.osa.org/abstract.cfm?URI=ao-28-12-2331 (cit. on p. 29).

[43] Arridge SR, Cope M, and Delpy DT. «The theoretical basis for the determination of optical pathlengths in tissue: temporal and frequency analysis». In: *Phys Med Biol.* 37.7 (July 1992), pp. 1531–60. DOI: 10.1088/0031-9155/37/7/005 (cit. on p. 29).

[44] Freund I I. «Surface reflections and boundary conditions for diffusive photon transport». In: *Phys Rev A.* 45.12 (June 1992), pp. 8854–8858. DOI: 10.1103/physreva.45.8854 (cit. on p. 29).

[45] Richard C. Haskell, Lars O. Svaasand, Tsong-Tseh Tsay, Ti-Chen Feng, Matthew S. McAdams, and Bruce J. Tromberg. «Boundary conditions for the diffusion equation in radiative transfer». In: *J. Opt. Soc. Am. A* 11.10 (Oct. 1994), pp. 2727–2741. DOI: 10.1364/JOSAA.11.002727. URL: http://josaa.osa.org/abstract.cfm?URI=josaa-11-10-2727 (cit. on p. 29).

[46] Alfio Quarteroni, Riccardo Sacco, and Fausto Saleri. *Numerical Mathematics*. New York: Springer-Verlag, 2000 (cit. on p. 42).

[47] Michael Wahl. *Time-Correlated Single Photon Counting*. PicoQuant GmbH. Rudower Chaussee 29, 12489 Berlin, Germany, 2014. URL: https://www.picoquant.com/images/uploads/page/files/7253/technote_tcspc.pdf (cit. on pp. 80, 81).

[48] Y. Prokazov, E. Turbin, A. Weber, R. Hartig, and W. Zuschratter. «Position sensitive detector for fluorescence lifetime imaging». In: *Journal of Instrumentation* 9.12 (Dec. 2014), pp. C12015–C12015. DOI: 10.1088/1748-0221/9/12/c12015 (cit. on p. 80).

[49] Longtao Yi, Zhiguo Liu, Kai Wang, Man Chen, Shiqi Peng, Weigang Zhao, Jialin He, and Guangcui Zhao. «A new background subtraction method for energy dispersive X-ray fluorescence spectra using a cubic spline interpolation». In: *Nuclear Instruments and Methods in Physics Research Section A: Accelerators, Spectrometers, Detectors and Associated Equipment* 775 (2015), pp. 12–14. ISSN: 0168-9002. DOI: https://doi.org/10.1016/j.nima.2014.11.100. URL: http://www.sciencedirect.com/science/article/pii/S0168900214014144 (cit. on p. 91).

[50] Tatu Rojalin et al. «Fluorescence-suppressed time-resolved Raman spectroscopy of pharmaceuticals using complementary metal-oxide semiconductor (CMOS) single-photon avalanche diode (SPAD) detector». In: *Analytical and Bioanalytical Chemistry* 408.3 (2016), pp. 761–774. ISSN: 16182650. DOI: 10.1007/s00216-015-9156-6 (cit. on p. 94).